THE UNIVERSITY OF CHICAGO

DESIGN OF SEMICONDUCTOR BIOINTERFACES FOR MODULATION OF CELLULAR SIGNALLING AND NEURONAL NETWORKS

A DISSERTATION SUBMITTED TO

THE FACULTY OF THE DIVISION OF THE PHYSICAL SCIENCES

IN CANDIDACY FOR THE DEGREE OF

DOCTOR OF PHILOSOPHY

DEPARTMENT OF CHEMISTRY

BY

VISHNU NAIR

CHICAGO, ILLINOIS

MARCH 2020

Dedicated to my parents and brother

Preface

The field of bioelectronics has come a long way in terms of its capabilities and outreach. Beginning with simple metallic electrodes and nanoscale field-effect transistors for biosensing or cellular stimulation the materials choices and design for bioelectronic architectures has evolved tremendously. Amongst the factors that led to such progress include the strategic identification of materials that would enable formation well-coupled junction with the cellular environment. Materials with a reduced mismatch of mechanical properties and optical or electronic properties allowing transduction of an external stimulus to cell responsible stimuli have been crucial in the development. Though the development of fundamental biophysical perspective has progressed the applicability of these across scales of the cellular environment, from *invitro* cultures to *invivo* organs have been slow. These have been attributed to three shortcomings. 1. Lack of knowledge of cellular signaling pathways activated by bio-electronic stimulation, 2. Design of material architectures for forming tissue level interfacing with low cytotoxicity, long term stability, and mechanical compatibility, 3. A platform for simultaneous sensing and stimulation. Seamless integration is the ultimate goal in bioelectronics wherein we overcome the three main difficulties discussed above, to expand proof-of-concept ideas into biomedical devices. Among the three main shortcomings, we plan to address the first two in this work.

The consequences of bioelectronic stimulation have been observed to be in four different modes - Thermal, capacitive, mechanical and electrochemical -subject to the electronic structure of the nanomaterial, mechanical properties, and nature of the external stimulus.

On a cellular level, each of these modes can induce their specific transduction pathways, which could have consequences leading to adaption or apoptosis of cells to such a perturbation. Systems leading to adaptation would be due to genetic or proteomic changes in the cellular system the utility of which could be used in disease cure. Similarly controlling apoptosis and its underlying mechanism could be utilized for developing specific cancer therapies and wound healing. Besides the adaptation of cells to stimulation-induced cellular perturbations, it could also be exploited via biomimicking nanomaterials that possess structure and properties similar to biological materials. Furthermore, to generalize our study it is important to move beyond adaptive and apoptotic signaling to study modulation of signaling synchronization between specific cell types. Such studies are important specifically from a neuromedicine perspective and form the foundation to address diseases in memory, learning or neurodegenerative disease. Hence studying artificial neuronal networks with various modes of stimulation provide a preliminary foundation in this aspect.

Designing architectures that can simultaneously be mechanically and biologically compatible, along with optoelectronic activity for stimulation are tricky keeping materials choices fixed. Thus, to satisfy the existing demands -the design of hybrid biointerfaces with a mechanically soft component and an optoelectronically active component is a proposed strategy. To achieve the development of such hybrid biointerfaces the use of conventional material synthetic processes is insufficient as most synthesis techniques are dynamically stable for, they are optimized for specific synthetic pathways and mechanisms. Thus, we require multistep synthetic strategies or unconventional non-

equilibrium synthetic processes for the development of such hybrid materials. This thesis explores unconventional non-equilibrium synthetic methods like laser ablation synthesis, cavitation synthesis and self-assembly for the design of semiconductor-based hybrid interfaces with specialized properties to modulate various signaling processes in a variety of biological systems.

Acknowledgments

The truth and beauty in science has never failed to fascinate me. However, understanding this truth and beauty to become a scientist has itself been an amazing journey. Most paths that we take up as adults are one among the ones not taken by others as described by Robert Frost. I came across so many of those colleagues, coworkers, and friends apart from my own family along this road who gave me the energy, support and directions to race through to my goal.

First and foremost, I would like to thank my family for their unconditional support making me capable of being a scientist. Also, for being with me through my ups and downs despite being oceans away from me. For making this scientist in me possible I would like to thank my adviser Bozhi Tian for his support and guidance as a mentor. Bozhi led me into the world of bioelectronics and brought out a hidden biologist and a future clinician-scientist in me. I appreciate very much the freedom, exposure, and opportunity towards scientific exploration given to me as a student in his group. I would also like to thank Dr. Jean T. Greenberg for mentoring me on my research work in Plant biology. Working with Jean and her group has been a wonderful learning experience for me. I want to extend my sincere thanks to Dr. Suriyanarayanan Vaikuntanathan and Dr. Yamuna Krishnan, my committee members for their valuable feedback and support through my Ph.D. Also, to thank the Krishnan lab members who have been very welcoming for scientific discussions and collaborations.

My research wouldn’t have been possible without a huge list of my collaborators across Chicago. I would like to thank Dr. Jaeseok Yi especially for being a kind and understanding a human being apart from being an amazing research mentor to me. Dr. Menahem Rotenberg who taught me hands-on biological and animal work. Jessica M. Morgan for teaching me how to do plant biology. Other lab members Lingyuan Meng, Aleksander Prominski, Dr. Xiang Gao and Dr. Jiping Yue for their hands-on support for me. Dr. Yuanwen Jiang, Dr. Yin Fang, and Dr. Yin Fang for all late-night science discussions, ideas, and advice. Dr. Joe Austin, Dr. Tera Lavoie and Yimei Chen for teaching me electron microscopy and giving me an amazing lifetime skill. Optical microscopy core staff Dr. Vytas Bindokas and Dr. Christine Labno for making my hands excellent at imaging and analysis. MRSEC manager Dr. Qiti Guo for his training and support with instrumentation. External collaborators Dr. Fengyuan Shi from UIC, Dr. Dieter Isheim, Dr. Xinqi Chen, Dr. Reiner Bleher and Dr. Eric W. Roth from Northwestern University.

It’s always friends who have been there to check on me in my hard times in life that we all phase through eventually. My best friends Jessica M. Morgan, Arvind Ilamaran, Atreyi Bhattacharya and Lorenz Matz for being with me. Music has always been a part of me and as a singer and flutist its always given me positive energy to pursue science. I would like to thank Lorenz Matz my interim pianist and Chicago Men's A Capella for getting me back to music and making me a happier and energetic person during my Ph.D. life.

Table of Contents

List of figures

1. Introduction†

1.1. Motivation

The field of medicine has made great strides in improving the quality of life for human beings across the globe. This gradual expansion and maturation of medicine have resulted from the contributions of scientists over the centuries who have attempted to understand living systems across different scales. Investigations, from the molecular and cellular levels to organs and whole animal level studies, have revealed how these systems function when in a state of equilibrium.[1] In the event of deviation from such a state—when these systems are incapable of adapting—the result is either disease, injury or disorder.[2] When such situations arise, the goal of medicine has been to restore humans to the optimal state of equilibrium using short-term or long-term solutions in the case of an acute or chronic condition, respectively.[3] However, to diagnose a specific medical condition, we need suitable techniques with which to probe a biological system and identify what specific type of non-equilibrium condition exists to clinically classify the disorder appropriately.[4] Medicine has successfully evolved such techniques to address virtually the entire range of disorders known to mankind. One essential component that has contributed immensely to the field of medical diagnostics are biosensors, tools that form an integral part of medicine as they are a very versatile platform for diagnosing a plethora of human disorders.[5]

Beyond the diagnosis of a condition or disorder, medicine aims to repair or restore the system to its original state. Medicine is greatly indebted to molecular biology for enabling

† *The introduction unit appears as Chapter 16 in Neural Interface Engineering, doi:10.1007/978-3-030-41854-0_16*

the use of small molecules—classified as drugs—for treating such disorders.[6] Though drugs come with their downsides, such as side effects, low efficacy, and low specificity, they have been the only successful method of treating nearly all human disorders.[7] The action of the drug upon the cells is typically mediated through these molecules, which selectively stimulate certain biological pathways, leading to a cascade of chemical reactions that often stabilize a cellular system (which, as a whole, cures the disorder).[8] Cellular stimulation and response to various stimuli have been part of numerous fundamental studies, such as the Hodgkin-Huxley experiment which enabled cell biologists to classify cells as excitable and non-excitable.[9-10] This further enabled electrophysiological research wherein studies utilizing an electrical stimulation generated a deeper understanding of the electrochemical properties of excitable cells.[11-12] These studies supported the development of external and implantable devices for the stimulation of excitable cells. The initial basic devices, such as the automated external defibrillator, vagus nerve stimulator, peripheral nerve stimulator, etc., are some of the most fundamental medical tools for dealing with acute and chronic disorders.[13-15] Hence, this trajectory of diagnosis and treatment leads to a synergistic relationship between sensing-associated diagnosis and stimulation-assisted treatment.[16]

The novel aim of bioelectronics is to precisely monitor a clinical condition, supply an appropriate dose of electrical or optoelectronic stimulation specific to that disorder, and thus cure the patient. However, depending on the acute or chronic nature of the condition behind the disorder, the time scale for monitoring and the associated feedback for stimulation-assisted treatment would vary. The device would need properties or features

that could enable implantation or removal, wireless communication and engineering design for seamless integration into a biological system.[17-18] In this thesis, we lay the foundation for the development of nanoscale devices with various modes of stimulation, and nanomaterial design strategies for the control of stimulation.

The scope of utilizing biointerfaces extends beyond the animal kingdom and is of tremendous interest in the plant kingdom. Plant kingdom forms an important part of the living world and their symbiosis with the animal kingdom is what enables life. Like animals, plants do enter diseased states on a very similar biochemical perspective.[19] Plant biologists refer to the perturbations here as stresses and classify them into biotic and abiotic.[20] Biotic stresses include pathogenic or animal attacks whereas abiotic stresses include variation in minerals, salinity, water and radiation damage. Material biointerfaces in this context form abiotic stresses to plants as they by their chemical composition are deemed minerals. Nanomaterials are often recognized by plants such that they evoke unique signaling pathways and lead to priming or immune enhancement in plants.[21] Nanomaterials may perform a mimicry to plants in being minerals enabling control in their signaling.

Having looked at the potential utility of material interfaces and junctions in forming a functional biointerface with selected entities of animal and plant kingdom in controlling specific signaling pathways. We look forward to designing and testing these aspects which enable such a control.

1.2. Model for cellular stimulation

Every cell that forms a part of tissues or organs has a unique role that it plays along with other cells of a similar type, all in an attempt to maintain homeostasis in the human body.[22] These cells are hence known as the fundamental unit of life and thus are our system of interest.[23] Cells are the model system used to investigate different types of stimulation and their aftereffects, intending to advance our knowledge of bioelectronics.

Cells are a set of complex non-linear systems that cycle in and out of equilibrium and are subject to environmental stresses [4]; they are sufficiently robust to handle a certain degree of stress. This cycling in and out of equilibrium is governed by fundamental molecular thermodynamics.[24] Thus, a precise understanding of cellular-level processes and signaling pathways tell us the nature of the stimulus that would be required to push a cell in and out of equilibrium.

Stimulation aims to apply a signal that is recognizable to cells, thus invoking a signaling pathway to push the system out of equilibrium. This would create a non-equilibrium cellular state, the decay of which relies on the stimuli strength and frequency.[24] Depending on these two factors, the cell can either adapt and modify itself or proceed towards apoptosis [25], reflecting a Darwinian like theory in action. Thus, one initial prerequisite of bioelectronic stimulation is the optimization of stimuli strength and frequency for adaptation—unless the goal is apoptosis.

To optimize the cellular stimulation, the design and implementation of the right stimuli transducer are critical. Given that these devices may require implantation and remote

control—depending on whether the disorder is acute or chronic—we would need miniaturized devices that are less invasive. Such devices should contain components that can transduce a stimulus to generate a cell-perturbing signal and would be graded with respect to the dosage and frequency of the stimulus. Thus, the transducing material would have a frequency response that would govern its interfacial coupling with cell and output signal magnitude (Fig.1.1). Nanomaterials are one set of candidates for this role as they have large active surface areas and can be electronically active with a frequency response.[26-27]

The interfacial coupling of a cell and a nanomaterial results in a junction or cleft [28] through which the transduced signal is scaled, phased and transferred to a cell (Fig.1.1). Such cell-material interfaces are chemically well-defined in terms of the surface functional groups that interact with the membrane proteins and the extracellular matrices (ECM) to form active junctions.[29] Such active junctions are electrically defined using a capacitive element and a resistance in parallel (Fig.1.1).[27] However, a signal that is transferred via this path has to go through two sets of circuits in series, from a constant phase element (CPE) element in the cleft [26] and the cell membrane [30], such that the effective interfacial impedance here governs the scaling and phasing of the signal that is transferred to the cell (Fig.1.1).[31]

1.3. Modes of stimulation

To achieve synergy between sensing and stimulation, we have concluded that miniaturized remote-controlled devices are a necessity. In conjunction with the

requirement of signal transduction by active materials in a device for stimulation and miniaturization, we identify stimuli-responsive nanomaterials as potential candidates.[32-34] Nanomaterials or nanoscale interfaces, by virtue of their solid-state structure, have electronic states which evolve in space and time according to the laws of quantum mechanics.[35] The development of powerful quantum chemistry computational methods has enabled us to understand how quantum confinement effects impact the electronic structure of nanomaterials and interfaces.[36] The electronic structure of a nanomaterial

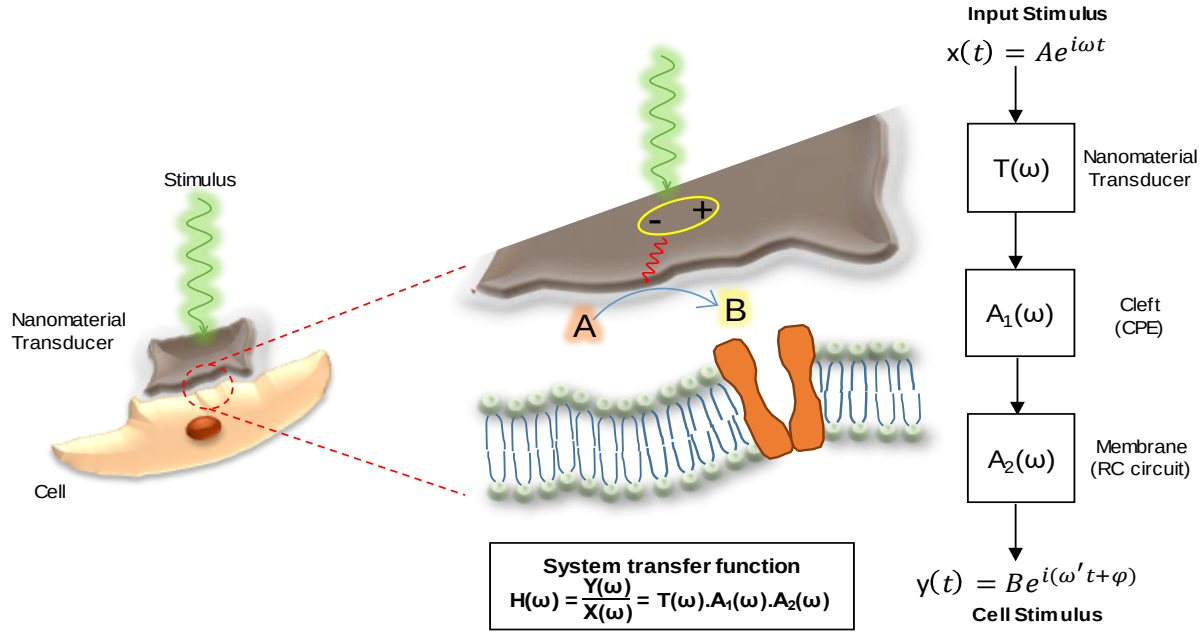

Fig. 1.1. Schematic representation of a cell-nanomaterial interface from a system science perspective. The schematic illustrates how the nanomaterial acts as a transducer with a frequency response T(w) to convert the stimulus into a cell-readable signal which is further modulated by the impedances A1(w) and A2(w) of the cleft and membrane, respectively. Thus, from a systems perspective, we can define the entire process of signal processing by the nanomaterial transducer and the impedances by a net transfer function H(w) given by the product of individual frequency responses in the frequency domain as the net transformation factor.

Fig.1.1. continued. Though the stimulus and cell-readable signal are in the time domain, a frequency domain analysis permits easier analysis as we can consider each component as a set of cascaded systems.

further governs its electronic, optical, magnetic and surface properties, all of which form an essential set of features that could be controlled by synthetic strategies.

Previous electrophysiology experiments have enabled the classification of cells into excitable versus non-excitable—though the goal of bioelectronic stimulation is to evolve a general strategy for stimulation as disorders are not specifically confined to excitable cells. Excitable cells have a binary response to an electrical, electrochemical or thermal stimulus, resulting in a membrane depolarization or hyperpolarization event.[10] In stark contrast, non-excitable cells have a continuum response thus allowing scope for a sub-threshold stimulation which leads to a diversified fate in the responding cells. Thus, nanomaterial synthesis for bioelectronics aims to design materials that can transduce fundamental forms of energy such as electromagnetic waves, heat, and sound, to create cell-recognizable stimuli like ionic currents, thermal gradients, and transient molecular species.[37,38] These stimuli, irrespective of their nature, depolarize or hyperpolarize the cell membrane, the consequences of which, though diverse, leading to an unstable non-equilibrium state in the cell.[37,38] We hereby classify the different modes of stimulation as thermal, electrochemical, and mechanical, depending on the form of the final cell receptive signal.

1.3.1 Thermal methods

Heat is a form of energy that can perturb the structure and function of molecules that make up biological components such as proteins, lipids, and nucleic acids.[39] Heat that is externally applied to a cell is generally capable of perturbing the lipid bilayer of a membrane and membrane proteins, causing changes in their structure and hence in the membrane capacitance and resistance.[37] The membrane capacitance controls the charge separation via an ionic gradient across the membrane that ultimately provides a measure of the membrane voltage. Thus, we can expect an apparent membrane voltage fluctuation to occur as a thermal stimulus is externally applied to a cell.[37] These membrane voltage fluctuations are read by excitable cells and non-excitable cells in different ways. An excitable cell would depolarize in response to heat only when it causes the membrane voltage to rise above a threshold. [37] On the other hand, a non-excitable cell continuously responds to a membrane potential increase by modulating the ionic concentration inside versus outside the cell to catch up with this perturbation.[10] Thus, such a continuous response of non-excitable cells gradually evokes organelle- and genetic-level responses to overcome this change more prominently than excitable cells, leading to sub-threshold stimulation.

To introduce such an external thermal stimulus, we should have candidate nanomaterials that can convert an optical stimulus to heat via defect or trap state-mediated carrier recombination or surface plasmon resonance.[40,41] Alternatively, a magnetothermal effect caused by the release of energy from a magnetization-demagnetization cycle in

nanoparticles can also produce such a result.[41] The dosage of a thermal stimulus varies according to the fundamental mechanism operating behind the transduction and its efficiency. In case of a semiconductor defect or trap state-mediated carrier recombination, we first need to estimate the defect density using photoluminescence or electrical transport techniques followed by an estimate of generation and recombination rates (Fig. 1.2.b). After estimating the rate of recombination, scaling it by the energy gap between the conduction band and trap states would yield a theoretical estimate of the heat generated (though practically there could be multiple dissipation pathways which are underestimated or ignored). In contrast, plasmonic heating deals with the oscillatory dissipation of energy by relatively free electrons at metallic surfaces.[41] According to the Drude-Lorentz model, surface atoms have an electron cloud that is weakly bound to the nuclei thus making them capable of oscillating in response to electromagnetic radiation. [41] Depending on the frequency of an electromagnetic wave we could model the electron cloud as an overdamped, underdamped or critically damped oscillator, ultimately dissipating energy in the form of heat (Fig. 1.2.c). On a similar note, a magnetic material placed in an oscillatory magnetic field dissipates the energy stored during a magnetization-demagnetization cycle (Fig. 1.2d.). [41] In general, thermal methods focus on the thermodynamic conversion of energy from one form to heat.

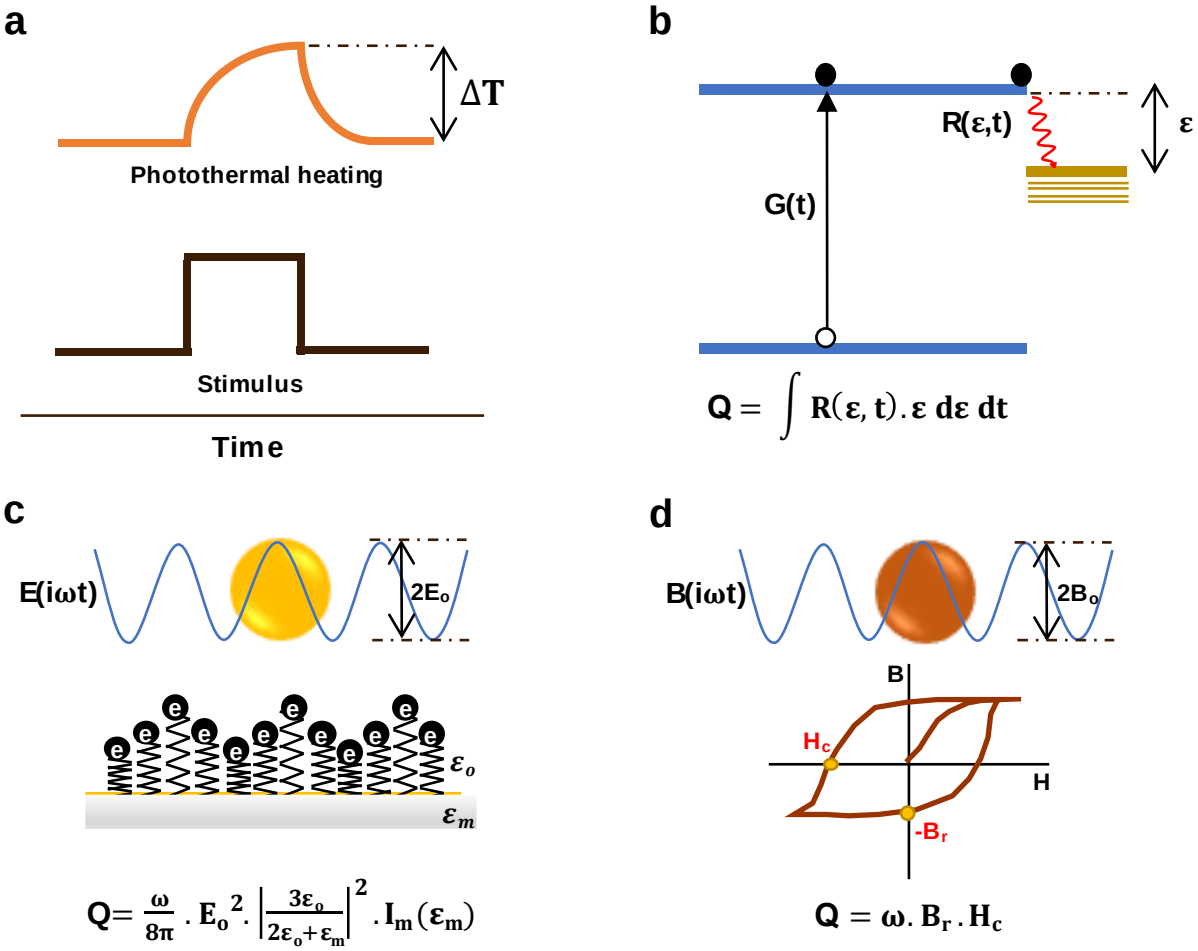

Fig. 1.2. Schematic illustration of different modes of thermal stimulus production using nanomaterials. a. A general schematic showing a standard photothermal response for a constant stimulus pulse. Thermal heating always increases with the application of a stimulus and saturates, only to exponentially decay as the stimulus is turned off. The peak of the heat profile measures ΔT from the thermal diffusion current which is proportional to heat generated Q. b. Illustration of heat generation from semiconductor defect recombination, where G(t) is the carrier generation rate due to photon absorption, R(ε,t) is the recombination rate from the conduction band into a defect state located energy ε below it and Q is the total estimate of heat generated from this process. c. Illustration of weakly-bound surface electrons and dissipating energy from an electrical field according to the Drude-Lorentz model, with Q being an estimate of heat generated. d. Equating the energy stored in a magnetic hysteresis cycle of a nanomaterial being dissipated as heat Q.

1.3.2 Electrochemical methods

Free energy (in all systems) is used to take a system towards an equilibrium state, thus maximizing the entropy and minimizing the free energy. In one such attempt, energy from an electromagnetic field may lead to the production of local charge separation in a material.[40] These localized charge separations are non-equilibrium states that have an associated excess of electrostatic potential energy. [40] This charge separation and the consequential electrostatic potential energy depends on the band structure of the material. Such available free energy in the form of electrostatic potential is precisely what drives electrochemistry at the interfaces.[43] An electrochemical reaction thus happens when a local charge separation (or exciton) has significant transient stability in the highest occupied molecular orbital (HOMO) and lowest unoccupied molecular orbital (LUMO) or the valence (VB) or conduction band (CB) of that material.[43] Such a stability enables separated charges to be transferred across an interface to a molecular species or material with overlapping density of states (Fig. 1.3.a,b).[43] An electrochemical process can polarize the immediate surroundings of an electrode due to charge accumulation on its surface. This polarization can cause membrane depolarization via capacitive coupling between the membrane and the electrode (Fig. 1.3.c).[43] However, if there is an overlap between the density of states of a species in solution and the electrode's HOMO or LUMO as illustrated in Fig. 1.3.a or b, then the species could undergo oxidation or reduction.[43] The consequences of such a redox reaction or faradaic injection (Fig. 1.3.d) are that a species of a specific charge accumulates in the cleft, causing depolarization or hyperpolarization via charge induction. Following this, the concentration of ions inside and

outside the cell are modified, leading to a new membrane potential governed by the Goldman–Hodgkin–Katz (GHK) equation (Fig. 1.3.e).[30] Besides perturbing a concentration gradient, such electrochemical reactions can produce cell-recognizable active molecules through a catalytic process. Cell-recognizable species mainly include reactive oxygen species, reactive nitrogen species, and oxidized or reduced metal ions or clusters.[38] Such cell-recognizable molecular species trigger a cascade in the cellular system leading to a membrane potential change, organelle stimulation, or genetic expression.[38] A similar effect could also be generated by cavitation effects. Ultrasound-induced cavitation can produce cavitating bubbles that could generate gigapascal and thousands of Kelvin of temperature to generate radical species like peroxides that can stimulate cells in a very similar fashion.[44] However, careful control of ultrasound intensity is important to ensure control of the cavitation thus giving electrochemical methods a significant edge over cavitation processes.

1.3.3 Mechanical methods

Compared to either thermal or electrochemical methods, mechanical stimulation operates in a fundamentally different way. This variation arises from the fact that cells have a piece of entirely different machinery with which to sense and respond to mechanical forces. Cells can convert such mechanical cues into intracellular electrochemical signals which lead to a signaling cascade.[45] This conversion of mechanical forces into electrochemical cues happens at mechanosensors which are classified into three classes.

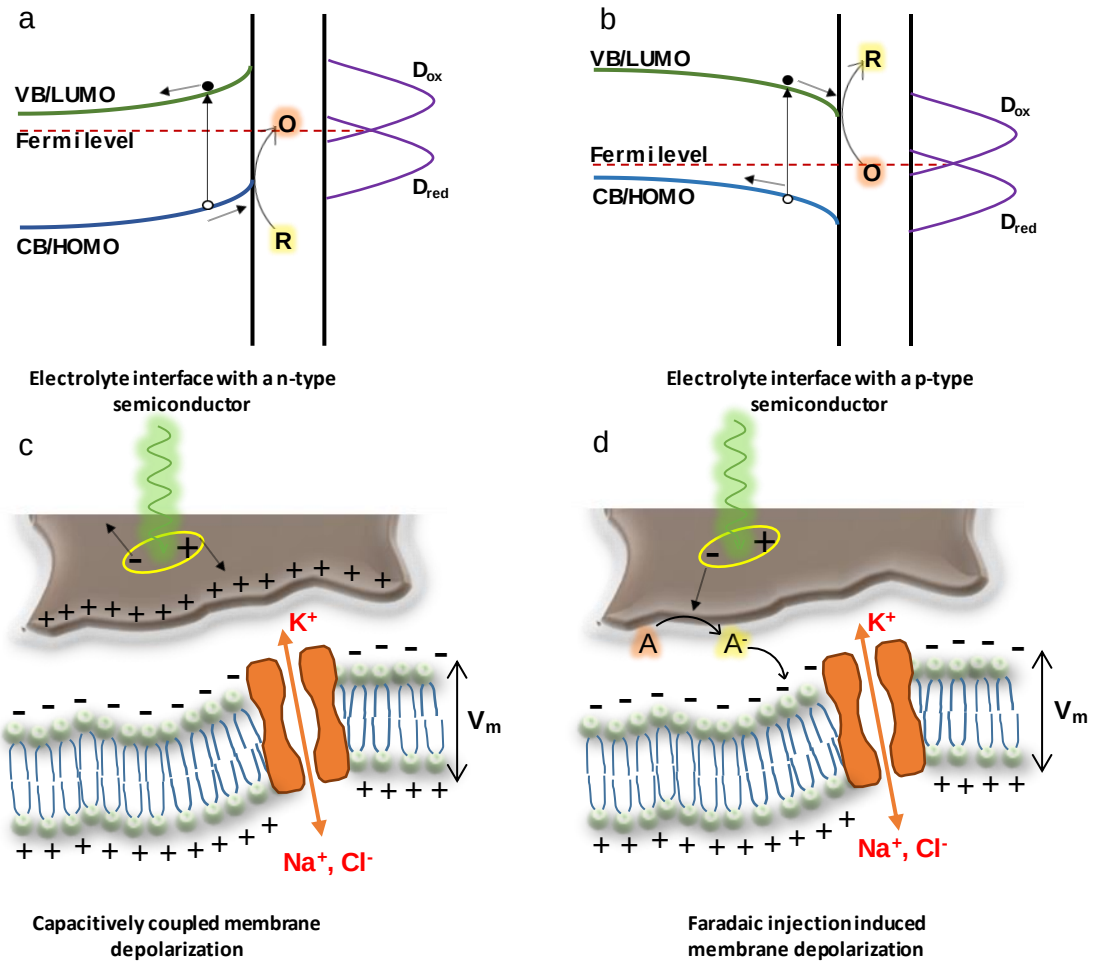

e Goldman-Hodgkin-Katz (GHK) equation

$$V_m = \frac{kT}{F} \ln \left\{ \frac{(P_K[K^+]_o + P_{Na}[Na^+]_o + P_{Cl}[Cl^-]_i)}{(P_K[K^+]_i + P_{Na}[Na^+]_i + P_{Cl}[Cl^-]_o)} \right\}$$

Fig. 1.3. a. Photon absorption and photooxidation process occurring at an n-type semiconductor-electrolyte interface, generating an anodic current. b. Photon absorption and photoreduction process occurring at a p-type semiconductor-electrolyte interface, generating a cathodic current. c. Capacitive depolarization of the cell membrane due to charge accumulation at the nanomaterial-cleft interface, causing charge-induced depolarization of the cell membrane. d. Faradaic reaction-induced redox species which either introduced an accumulation of charged species causing membrane depolarization or a molecular active species which caused receptor binding mediated depolarization. e. The GHK equation describing the variation in membrane voltage with differing concentrations of ions.

Mechanosensing by the plasma membrane is mediated caveolin or cilia or microvilli which leads to the inward wrinkling of the plasma membrane.[45] Further, these are primarily determined by the topographical features of the biointerface which forms a junction with the cell. In such situations, the plasma membrane bending and stabilization following topographical features decided the mechanotransduction.[46] Membrane stabilization on various nanoscale topographical features evoke cellular signaling mechanisms which lead to cytoskeletal structuration and nanoinvaginations processes for endocytotic regulation.[46] Alternatively, mechanosensing can happen through an intracellular or extracellular mechanism as well. In these cases, they are mediated through actin cytoskeleton, glycocalyx, cadherin rich cell-cell junction or mechanosensitive ion channels.[45] Among these, the mechanosensitive ion channels are the fastest and thus of extensive interest though many of these mechanisms could be coupled with respect to each other.

Cells are coupled to the ECM via integrin proteins that extend from the cytosol into the external environment.[47] Integrin proteins connect the cytoskeletal filaments to the ECM through the focal adhesions and the phospholipid bilayer (Fig. 1.4.b). Thus, any force that the cell receives is via the ECM and goes into the focal adhesions or directly onto the lipid bilayer (Fig. 1.4.a,b).[46] Extracellular forces such as fluid flow shearing, tensile and traction forces along with intracellular contractile forces are the primary agents that bring about and mechanical stimulation. Such forces are transduced by mechanosensitive ion

channels present on the cell membrane. These mechanosensitive ion channels physically open or close in response to a force traveling through the lipid bilayer or cytoskeletal filaments. Such channels were open or close to producing membrane voltage fluctuations which could lead to depolarization or hyperpolarization of the cell membrane. Thus, magnetic, optical, or piezo-responsive nanomaterials which can exert force on the lipid bilayer or the ECM to transduce a cytoskeletal force are additional modes of cellular stimulation. [46]

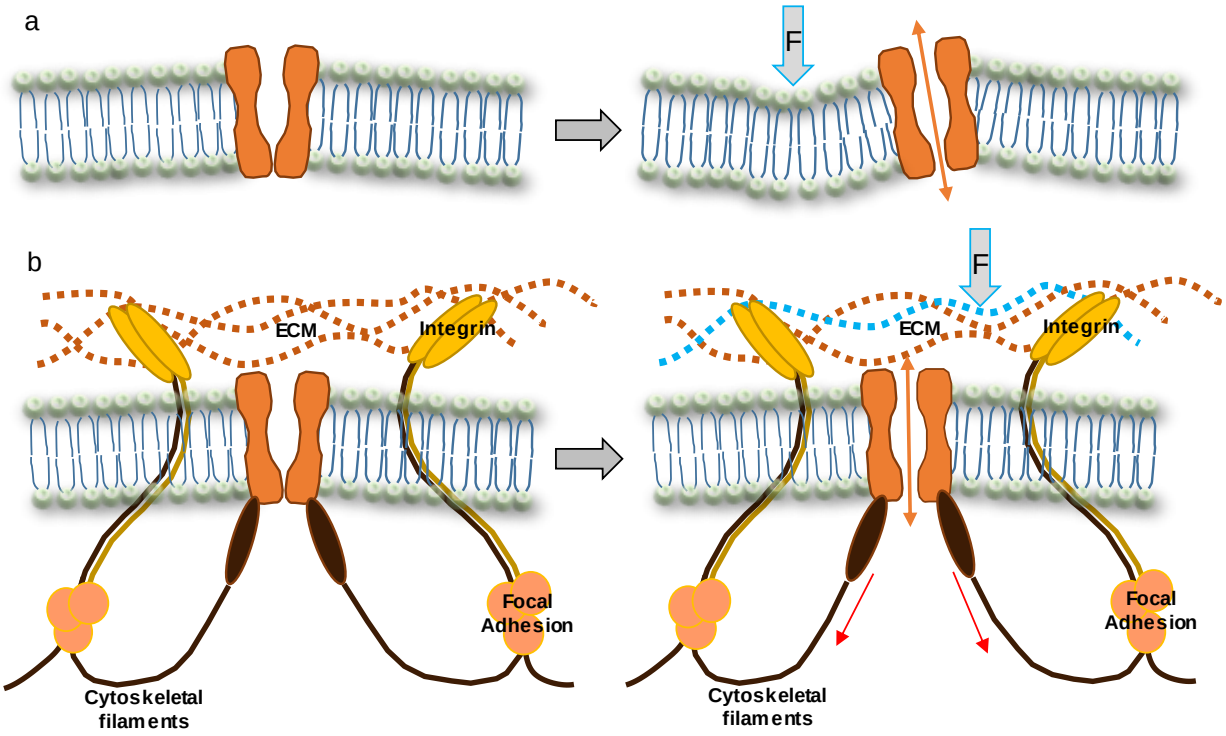

Fig. 1.4. a. A direct force of the lipid layer causing mechanosensitive ion channels to activate, open and produce depolarization. b. Force in ECM transduced via integrin and cytoskeletal filaments, causing a mechanosensitive channel to open.

1.4. Cellular network stimulation and synchronization

The response to a cellular stimulation could be read out on an individual cell or an ensemble. An ensemble here would consist of cells that are connected through electrically active cell-cell junctions or though neurites as in neurons. Thus, the response in such a connected system of cells towards a stimulation on one part of it could be understood through synchronization between electrical activity between these cells. These networks could be divided into nodes and one way to record electrical activity would use array devices that make contact with cells that are part of the network.[48] However, an alternative, cheaper and traditional way would be looking at calcium signals which can give similar information.[49,50]

Studying brain rhythms and associated synchronization has become an important part of neuroscience.[49-51] The oscillatory activity of neurons which underlie the formation of brain rhythms always exists with non-oscillatory noise.[49-51] However, these rhythms appear to exist only at certain frequencies and are a result of large coordinated activity in neuronal networks.[51] Though these are higher dimensional dynamical systems their analysis could be simplified by modeling them as low dimensional chaotic oscillators that are coupled.[51] Further, these oscillators are self-sustained - as they are an autonomous continuous-time dynamic system.[51] Such self-sustained oscillators are described in non-linear dynamics using a phase which acts as a variable for parametrizing motion along a cycle.[51]

Synchronization is defined as phase and frequency locking between different oscillators in a system. [49-51] In our case these oscillators are neurons that are chaotic and self-

sustaining. One of the measures of synchrony popularly used in neuroscience is phase synchronization. [49-51] Phase synchronization is advantageous as it is time-resolved and only sensitive to phases and not the amplitude. [49-51] If we have two continuous-time signal x(t) and y(t) then we would need to determine their instantaneous phases. $\varphi_X(t)$ and $\varphi_Y(t)$ respectively. This is one by taking the Hilbert transform of the continuous-time signal given by $\tilde{x}$(t) = $\frac{1}{\pi}\int_{-\infty}^{\infty}\frac{x(t')}{t-t'}\,dt'$. The Hilbert phase can be obtained by $\tan^{-1}\frac{\tilde{x}(t)}{x(t)}$. Once the Hilbert phase is obtained the mean synchronization index can be calculated between every neuron pair for N time steps as $|\frac{1}{N}\sum_{j=1}^{N} e^{i(\varphi_X(t_j)-\varphi_Y(t_j))}|$. The values of mean synchronization index vary between 0 and 1, one being the most synchronized and zero the least.

1.5. Biointerface design strategies

Having explored the different modes of stimulation we can determine a requisite property that each of these nanomaterials should possess for a stimulus to be transduced as a cell-recognizable signal. Beyond the functional capability of generating a cell-recognizable signal, we may need to explore other properties that are required for a well-coupled bio-interface. For example, the nanomaterial under consideration should be biocompatible, sufficiently mechanically flexible (like ECM or cytoskeleton), and have the appropriate surface chemistry for cellular recognition.[48] To further extend the capabilities of this nanomaterial for simultaneous sensing and stimulation with a feedback interlock, it is necessary to use appropriate nanofabrication technologies to design three-dimensional devices capable of interfacing with tissues.[52] If achieved, this would be the

ultimate goal of seamless integration. Hence our focus is on obtaining a three-dimensional framework of appropriate size—as well as the correct mechanical and electronic properties—capable of carrying out spatiotemporal mapping and stimulation. Existing synthetic nanomaterials have wide-ranging optoelectronic and mechanical properties, thus the task here is to make the appropriate selection from the range of available options. For ideal sensing capabilities, we need to select a material with an electronic structure that has a maximum signal to noise ratio (SNR) subject to screening limited response at physiological conditions. Similarly, for stimulation capabilities, a good understanding of the electronic structure and the subsequent efficiency of signal transduction is important to determine the appropriate dosage. Both stimulation and sensing depend on the electronic structural properties which reside in their dimensionality, chemical composition, and surface chemistry, for dosage and sensitivity, respectively.[53] Thus, the selection process for the choice of nanomaterials could be decentralized based on these fundamental properties. This would ultimately enable us to have electronic components capable of performing simultaneous stimulation and sensing.

Once it's possible to draw up a shortlist of nanomaterials based on their electronic properties, and included information on the appropriate dimension, chemical compositio, and surface chemistry. Next, a sub-search within this set has to be performed for mechanical compatibility and biocompatibility. The latter is usually assessed by carrying out a combination of device stability and cytotoxicity testing. This involves checking degradation and its by-products formed from nanomaterials under physiological conditions in human blood plasma or serum, or in vivo testing.[48,53] An appropriate

quantification and identification of the degradation by-products and immune response like scarring and cell death enable researchers to predict the cytotoxicity. Device degradation by enzymes and pH is an equally important property to be determined through in vivo testing to assess device delamination, corrosion, and fractures. On the other hand, mechanical compatibility of a nanomaterial is theoretically predicted by a deviation of the persistence length of 1D architectures or nanoscale elasticity modulus in case of 2D or 3D structures, to cellular ECM or cytoskeleton. Nanoscale mechanical property measurement using atomic force microscopy or microrheology allows us to obtain information on mechanical compatibility. Furthermore, the materials for flexible device fabrication and signal readout could be chosen from existing nanofabrication techniques to select materials with properties that facilitate seamless integration. The procedure described here is a sequential selection process that allows us to select materials from an existing library, a process that could be efficiently outsourced to machine learning (Fig. 1.5.a).

In addition to a smart selection process to find the right set of materials from an existing pool one could envision design strategies maximized to obtain hybrid materials with the requisite properties. At this juncture, we need to classify materials into hard and soft and attempt to think of hard-soft hybrid materials as a solution to seamless integration. The design of a hard-soft hybrid could be done by embedding a functionally active material into a soft matrix, serving as a mechanically compatible framework for the device. Such a fabrication could be achieved by either using additives in the starting material of the synthesis, by the application of an in situ synthetic processes, or by a post-synthetic

modification process (Fig. 1.5.b). As a result, we have a three-way flexible synthetic strategy by which we can design new hard-soft hybrid materials for seamless integration.

1.6. Themes for investigation

Working towards the goal of designing biointerfaces for modulation of specific biological process we are limited by: 1. Lack of knowledge of cellular signaling pathways activated by bioelectronic stimulation, 2. Design of three-dimensional architectures for forming tissue level interfacing with low cytoxicity, long term stability, and mechanical compatibility, 3. A platform for simultaneous sensing and stimulation.[54] We devise our

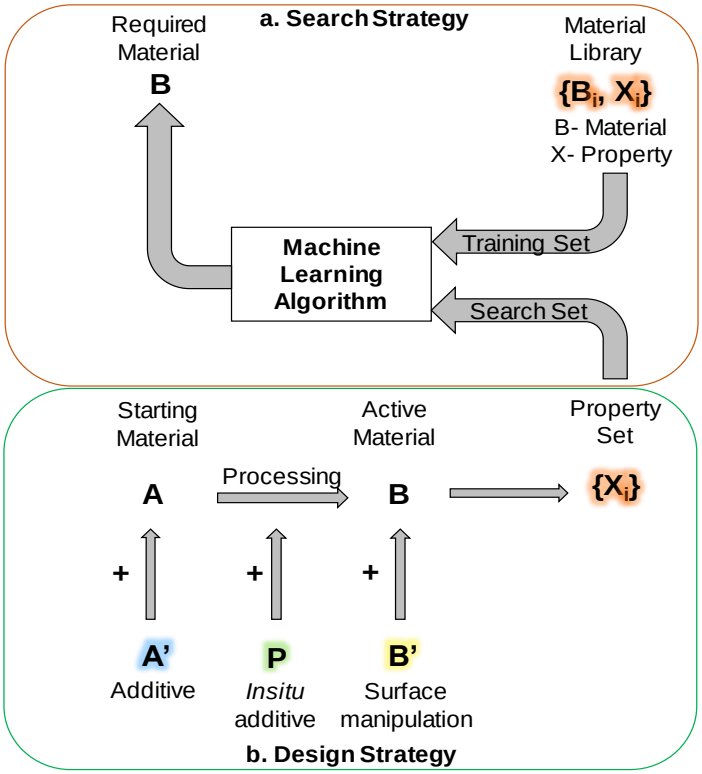

Fig. 1.5. a. Discussion of the selection strategy via machine learning searching for seamless integration. b. Discussion of a material design strategy via a three-way control to obtain material for seamless integration.

research directions towards overcoming the first two shortcomings. Herein we focus our studies on cellular signaling and synchronization with various types of stimulation and intensity along with the development of hard-soft interfaces using unconventional non-equilibrium synthetic methods like laser ablation synthesis, cavitation synthesis, and self-assembly. Such hard-soft interfaces are expected to form better junctions with cells with biocompatibility and lesser mechanical mismatch. In order to achieve these, we work in three different directions:

Laser ablation synthesis of PDMS-SiC hard-soft hybrid biointerface

In line with these future goals of seamless integration, we build on existing chemistry to demonstrate in our work a laser ablation-based technique for *in-situ* conversion of poly dimethyl siloxane (PDMS) to SiC. This technique enables us to obtain nitrogen-doped cubic SiC patterns embedded in a soft PDMS matrix, thus creating a soft-hard hybrid with a hard electronically functional and soft mechanically compatible component. Moreover, depending on the optics and laser writing parameters one could obtain well defined two- and three-dimensional devices or circuits as required. The SiC formed in this synthetic methodology by the ablation technique used comes with a graphite layer beneath, which acts as an electrode for easy interfacing and integration into circuits. These printed electrodes also exhibit pseudocapacitive charging thus demonstrating their capability in forming well-coupled junctions with cellular systems for direct electrical stimulation or as free-standing devices. Furthermore, the nitrogen-doped cubic SiC obtained can perform

in a free-standing mode, photoelectrochemical oxidation of water to hydrogen peroxide in low non-apoptotic doses. These observed features together thus form a big step forward in the field of bio-electronics towards future seamless integration.

Laser ablation synthetic techniques have often been under-utilized for materials design due to the lack of better guiding principles. Hence, we propose a two-way modification strategy to our existing synthetic method of laser ablation mediated conversion of PDMS to SiC. This two-way strategy involves using additives in the starting raw material or a surface functionalization of the final active material to obtain a different set of optoelectronic properties to ultimately influence their final cellular level stimulus in response to light absorption. To demonstrate this strategy, we use bulk molybdenum disulfide (MoS_2) as a starting material additive and manganese dioxide (MnO_2) as a surface functionalization. As a consequence of MoS_2 as an additive in PDMS, we obtain crystal phase scrambling and excessive nitrogen doping in SiC whereas the surface MnO_2 coating on cubic SiC only enhances the photoanodic reaction. Thus, along with tunability in the synthesis, this two-way modification strategy reveals to us that additives control the crystal structure and doping whereas surface modification controls electrochemistry. Either of these strategies thus become tuning gears for bioelectronics to expand their capabilities for various biological systems. Thus, besides making significant progress towards seamless integration we demonstrate the tunability of the synthetic technique and lay forward a material design principle in the field of laser ablation synthesis.

Extracellular matrix mimicking poly-(3 hexyl thiophene) (P3HT) nanofiber bio-interfaces

Extracellular matrices (ECM) are large macromolecular networks that provide cells with structural and biochemical support. Cells interface with these network-like structures through integrin proteins that enable force transduction from the ECM to focal adhesions. Hence the focal adhesion assembly and cell migration are influenced by the stiffness of the matrix. Thus, designing a soft network matrix that can mimic extracellular matrices and also possess optoelectronic activity is a potential platform for optical modulation of cellular activity. Organic semiconductors which are soft and can be fabricated into low dimensional nanostructures with varying optoelectronic properties are thus an ideal candidate for such investigations.

Based on the electrical property of cell membranes, cells are classified into excitable and non-excitable. Excitable cells have a binary response towards a stimulus that perturb their membrane voltage, whereas non-excitable cells have a continuum response. Thus, non-excitable cells form an ideal system to explore the much less studied sub-threshold stimulation to understand specific signaling cascades. Such stimulated signaling and its strength depend on the stimuli strength and its ability in overcoming biological noise thus enabling one to strengthen specific signaling pathways.

In our work, we demonstrate the capability of an organic semiconducting nanofiber network to control signaling pathways with apoptosis as a model problem. Using an optical stimulus, we perform time-domain studies of mitochondrial calcium and caspase signaling to understand the non-equilibrium dynamics of apoptotic cells. These studies

suggest to us how an optical stimuli strength can control the apoptosis mechanism between type 1 and type 2. Furthermore, we look at cytoskeletal filament and focal adhesion organization on the matrix to understand the potential of ECM mimicry. Ultimately, this work lays a foundation for sub-threshold stimulation in addressing diseases and studies in systems biology.

Coaxial silicon nanowire hybrid structures and mineralizing biointerfaces

We utilize a self-assembling technique in designing a hard-soft hybrid by self-assembling P3HT on a silicon nanowire surface to obtain a coaxial hard soft-hybrid. Besides, the utility of growing a softer phase on silicon using self-assembly, mechanochemistry could enable us to generate hard-soft interfaces by growing harder graphene on comparatively softer silicon. Such hybrid hard-soft interfaces are candidates for testing mechanosensing in cells and for future material development in tissue regeneration, differentiation and wound healing.

The potential utility of silicon nanowire surfaces in silicic acid generation and *invitro* mineralization into silicates could be utilized for defense priming in plants. This mineralization and silicic acid formation could be further illustrated by coupling cavitation forces. Apart from such cavitation coupled catalysis using free-standing nanowires the silicon nanowire -graphene hybrid generated by mechanochemical synthesis be utilized for photocatalyzed oxygen reduction to hydrogen peroxide. Hydrogen peroxide and reactive oxygen species are well known in plants as signaling molecules during abiotic stresses. Hence the production of hydrogen peroxide by internalized silicon nanowire -

graphene hybrid could also be utilized for defense priming in plants. Thus, cavitation coupled catalysis and synthesis of soft-hard hybrids are of significant interest for modulation of plant signaling pathways.

References

1. Sung, J. H.; Esch, M. B.; Prot, J.-M.; Long, C. J.; Smith, A.; Hickman, J. J.; Shuler, M. L. Microfabricated Mammalian Organ Systems and Their Integration into Models of Whole Animals and Humans. Lab Chip 2013, 13 (7), 1201.

2. Hernández-Lemus, E. Nonequilibrium Thermodynamics of Cell Signaling. Journal of Thermodynamics 2012, 2012, 1–10.

3. Murrow, E. J., Oglesby, F. M. Acute and chronic illness: similarities, differences and challenges. Orthop Nurs. 1996, 15,47-51.

4. Wang, L.; Haug, P. J.; Del Fiol, G. Using Classification Models for the Generation of Disease-Specific Medications from Biomedical Literature and Clinical Data Repository. Journal of Biomedical Informatics 2017, 69, 259–266. https://doi.org/10.1016/j.jbi.2017.04.014.

5. Bhalla, N.; Jolly, P.; Formisano, N.; Estrela, P. Introduction to Biosensors. Essays in Biochemistry 2016, 60 (1), 1–8.

6. Hassan Baig, M.; Ahmad, K.; Roy, S.; Mohammad Ashraf, J.; Adil, M.; Haris Siddiqui, M.; Khan, S.; Amjad Kamal, M.; Provazník, I.; Choi, I. Computer Aided Drug Design: Success and Limitations. CPD 2016, 22 (5), 572–581.

7. Niu, Y.; Zhang, W. Quantitative Prediction of Drug Side Effects Based on Drug-Related Features. Interdiscip Sci Comput Life Sci 2017, 9 (3), 434–444.

8. Ritter, J. M.; Ferro, A.; Lewis, L. D.; Mant, T. G. K. Textbook of Clinical Pharmacology and Therapeutics.; Hodder Education, 2008.

9. Hodgkin, A. L.; Huxley, A. F. Currents Carried by Sodium and Potassium Ions through the Membrane of the Giant Axon of Loligo. The Journal of Physiology 1952, 116 (4), 449–472.

10. Cervera, J.; Alcaraz, A.; Mafe, S. Membrane Potential Bistability in Nonexcitable Cells as Described by Inward and Outward Voltage-Gated Ion Channels. J. Phys. Chem. B 2014, 118 (43), 12444–12450. https://doi.org/10.1021/jp508304h. 11. Linaro D, Couto J, Giugliano M (2015) Real-time Electrophysiology: Using Closed-loop Protocols to Probe Neuronal Dynamics and Beyond. J Vis Exp. doi: 10.3791/52320.

12. O'Shea, C.; Holmes, A. P.; Winter, J.; Correia, J.; Ou, X.; Dong, R.; He, S.; Kirchhof, P.; Fabritz, L.; Rajpoot, K.; et al. Cardiac Optogenetics and Optical Mapping – Overcoming Spectral Congestion in All-Optical Cardiac Electrophysiology. Front. Physiol. 2019, 10, 182.

13. Ellison, K.; Sharma, P. S.; Trohman, R. Advances in Cardiac Pacing and Defibrillation. Expert Review of Cardiovascular Therapy 2017, 15 (6), 429–440.

14. González, H. F. J.; Yengo-Kahn, A.; Englot, D. J. Vagus Nerve Stimulation for the Treatment of Epilepsy. Neurosurgery Clinics of North America 2019, 30 (2), 219–230.

15. Chakravarthy, K.; Nava, A.; Christo, P. J.; Williams, K. Review of Recent Advances in Peripheral Nerve Stimulation (PNS). Curr Pain Headache Rep 2016, 20 (11), 60.

16. Fu, T.-M.; Hong, G.; Zhou, T.; Schuhmann, T. G.; Viveros, R. D.; Lieber, C. M. Stable Long-Term Chronic Brain Mapping at the Single-Neuron Level. Nat Methods 2016, 13 (10), 875–882.

17. Implantable Bioelectronics: Devices, Materials, and Applications, 1. ed.; Katz, E., Ed.; Wiley-VCH: Weinheim, 2014.

18. Zhang, H.; Gutruf, P.; Meacham, K.; Montana, M. C.; Zhao, X.; Chiarelli, A. M.; Vázquez-Guardado, A.; Norris, A.; Lu, L.; Guo, Q.; et al. Wireless, Battery-Free Optoelectronic Systems as Subdermal Implants for Local Tissue Oximetry. Sci. Adv. 2019, 5 (3), eaaw0873.

19. Bonas, U. Plant Disease Resistance Triggered by Pathogen-Derived Molecules: Refined Models of Specific Recognition. Current Opinion in Microbiology 2002, 5 (1), 44–50.

20. Pandey, P.; Irulappan, V.; Bagavathiannan, M. V.; Senthil-Kumar, M. Impact of Combined Abiotic and Biotic Stresses on Plant Growth and Avenues for Crop Improvement by Exploiting Physio-Morphological Traits. Front. Plant Sci. 2017, 8.

21. Sanzari, I.; Leone, A.; Ambrosone, A. Nanotechnology in Plant Science: To Make a Long Story Short. Front. Bioeng. Biotechnol. 2019, 7, 120.

22. Davies, K. J. A. Adaptive Homeostasis. Molecular Aspects of Medicine 2016, 49, 1–7.

23. Plopper, G. Principles of Cell Biology, Second edition.; Jones & Bartlett Learning: Burlington, MA, 2016.

24. Olivier, B. G.; Swat, M. J.; Moné, M. J. Modeling and Simulation Tools: From Systems Biology to Systems Medicine. In Systems Medicine; Schmitz, U., Wolkenhauer, O., Eds.; Springer New York: New York, NY, 2016; Vol. 1386, pp 441–463.

25. Strasser, A.; O'Connor, L.; Dixit, V. M. Apoptosis Signaling. Annu. Rev. Biochem. 2000, 69 (1), 217–245.

26. Lasia, A. Electrochemical Impedance Spectroscopy and Its Applications; Springer: New York, 2014.

27. Nair, V.; Ananthoju, B.; Mohapatra, J.; Aslam, M. Photon Induced Non-Linear Quantized Double Layer Charging in Quaternary Semiconducting Quantum Dots. Journal of Colloid and Interface Science 2018, 514, 452–458. doi:10.1016/j.jcis.2017.12.034.

28. Santoro, F.; Zhao, W.; Joubert, L.-M.; Duan, L.; Schnitker, J.; van de Burgt, Y.; Lou, H.-Y.; Liu, B.; Salleo, A.; Cui, L.; et al. Revealing the Cell–Material Interface with Nanometer Resolution by Focused Ion Beam/Scanning Electron Microscopy. ACS Nano 2017, 11 (8), 8320–8328.

29. Cutler, S. Engineering Cell Adhesive Surfaces That Direct Integrin A5β1 Binding Using a Recombinant Fragment of Fibronectin. Biomaterials 2003, 24 (10), 1759–1770.

30. Principles of Neural Science, 4th ed.; Kandel, E. R., Schwartz, J. H., Jessell, T. M., Eds.; McGraw-Hill, Health Professions Division: New York, 2000.

31. Sedra, A. S.; Smith, K. C. Microelectronic Circuits, 6th ed.; The Oxford series in electrical and computer engineering; Oxford University Press: New York, 2010.

32. Jiang, Y.; Carvalho-de-Souza, J. L.; Wong, R. C. S.; Luo, Z.; Isheim, D.; Zuo, X.; Nicholls, A. W.; Jung, I. W.; Yue, J.; Liu, D.-J.; et al. Heterogeneous Silicon Mesostructures for Lipid-Supported Bioelectric Interfaces. Nature Mater 2016, 15 (9), 1023–1030.

33. Parameswaran, R.; Carvalho-de-Souza, J. L.; Jiang, Y.; Burke, M. J.; Zimmerman, J. F.; Koehler, K.; Phillips, A. W.; Yi, J.; Adams, E. J.; Bezanilla, F.; et al. Photoelectrochemical Modulation of Neuronal Activity with Free-Standing Coaxial Silicon Nanowires. Nature Nanotech 2018, 13 (3), 260–266.

34. Tortiglione, C.; Antognazza, M. R.; Tino, A.; Bossio, C.; Marchesano, V.; Bauduin, A.; Zangoli, M.; Morata, S. V.; Lanzani, G. Semiconducting Polymers Are Light Nanotransducers in Eyeless Animals. Sci. Adv. 2017, 3 (1), e1601699.

35. Kuno, M. Introductory Nanoscience; Garland Science: London ; New York, 2012.

36. Burdett, J. K. Electronic Structure and Properties of Solids. J. Phys. Chem. 1996, 100 (31), 13263–13274.

37. Carvalho-de-Souza, J. L.; Pinto, B. I.; Pepperberg, D. R.; Bezanilla, F. Optocapacitive Generation of Action Potentials by Microsecond Laser Pulses of Nanojoule Energy. Biophysical Journal 2018, 114 (2), 283–288.

38. Rosado, J.; Redondo, P.; Salido, G.; Pariente, J. Calcium Signalling and Reactive Oxygen Species in Non-Excitable Cells. MRMC 2006, 6 (4), 409–415.

39. Huang, R.; Lau, B. L. T. Biomolecule–Nanoparticle Interactions: Elucidation of the Thermodynamics by Isothermal Titration Calorimetry. Biochimica et Biophysica Acta (BBA) - General Subjects 2016, 1860 (5), 945–956.

40. Streetman, B. G.; Banerjee, S. Solid State Electronic Devices, Seventh edition.; Pearson: Boston, 2015.

41. Govorov, A. O.; Richardson, H. H. Generating Heat with Metal Nanoparticles. Nano Today 2007, 2 (1), 30–38. https://doi.org/10.1016/S1748-0132(07)70017-8.

42. Skumiel, A.; Kaczmarek-Klinowska, M.; Timko, M.; Molcan, M.; Rajnak, M. Evaluation of Power Heat Losses in Multidomain Iron Particles Under the Influence of AC Magnetic Field in RF Range. Int J Thermophys 2013, 34 (4), 655–666.

43. Krishnan Rajeshwar. Fundamentals of Semiconductor Electrochemistry and Photoelectrochemistry. In Encyclopedia of Electrochemistry; Bard, A. J., Ed.; Wiley-VCH Verlag GmbH & Co. KGaA: Weinheim, Germany, 2007; p bard060001.

44.Hernández-García, D.; Castro-Obregón, S.; Gómez-López, S.; Valencia, C.; Covarrubias, L. Cell Death Activation during Cavitation of Embryoid Bodies Is Mediated by Hydrogen Peroxide. Experimental Cell Research 2008, 314 (10), 2090–2099.

45. Bavi, N.; Nikolaev, Y. A.; Bavi, O.; Ridone, P.; Martinac, A. D.; Nakayama, Y.; Cox, C. D.; Martinac, B. Principles of Mechanosensing at the Membrane Interface. In The Biophysics of Cell Membranes; Epand, R. M., Ruysschaert, J.-M., Eds.; Springer Singapore: Singapore, 2017; Vol. 19, pp 85–119.

46. Pennacchio, F. A.; Caliendo, F.; Iaccarino, G.; Langella, A.; Siciliano, V.; Santoro, F. Three-Dimensionally Patterned Scaffolds Modulate the Biointerface at the Nanoscale. Nano Lett. 2019, 19 (8), 5118–5123

47. Kumar, A.; Ouyang, M.; Van den Dries, K.; McGhee, E. J.; Tanaka, K.; Anderson, M. D.; Groisman, A.; Goult, B. T.; Anderson, K. I.; Schwartz, M. A. Talin Tension Sensor Reveals Novel Features of Focal Adhesion Force Transmission and Mechanosensitivity. J Cell Biol 2016, 213 (3), 371–383.

48. Chen, R.; Canales, A.; Anikeeva, P. Neural Recording and Modulation Technologies. Nat Rev Mater 2017, 2 (2), 16093.

49. Artimovich, E.; Jackson, R. K.; Kilander, M. B. C.; Lin, Y.-C.; Nestor, M. W. PeakCaller: An Automated Graphical Interface for the Quantification of Intracellular Calcium Obtained by High-Content Screening. BMC Neurosci 2017, 18 (1), 72.

50. Patel, T. P.; Man, K.; Firestein, B. L.; Meaney, D. F. Automated Quantification of Neuronal Networks and Single-Cell Calcium Dynamics Using Calcium Imaging. Journal of Neuroscience Methods 2015, 243, 26–38.

51. Guevara Erra, R.; Perez Velazquez, J. L.; Rosenblum, M. Neural Synchronization from the Perspective of Non-Linear Dynamics. Front. Comput. Neurosci. 2017, 11, 98.

52. Dai, X.; Hong, G.; Gao, T.; Lieber, C. M. Mesh Nanoelectronics: Seamless Integration of Electronics with Tissues. Acc. Chem. Res. 2018, 51 (2), 309–318.

53. Jiang, Y.; Tian, B. Inorganic Semiconductor Biointerfaces. Nat Rev Mater 2018, 3 (12), 473–490.

54. Birmingham, K.; Gradinaru, V.; Anikeeva, P.; Grill, W. M.; Pikov, V.; McLaughlin, B.; Pasricha, P.; Weber, D.; Ludwig, K.; Famm, K. Bioelectronic Medicines: A Research Roadmap. Nat Rev Drug Discov 2014, 13 (6), 399–400.

2. Laser printing of nitrogen-doped silicon carbide structures for multimodal biointerfaces.

2.1. Introduction

Synthetic laser ablation techniques have been utilized for nanomaterial design due to their ease of fabrication, low cost, and their unique capacity to generate exotic phases that are stable only under non-equilibrium conditions.[1-4] There are, however, a lack of available design principles to fully exploit this method for creating materials with specific properties. Specificity in material properties arising out of rational synthetic manipulations enables one to correlate these properties with their potential utility. We are interested, therefore, in exploring their utility in the context of biological modulation.

In line with these goals, material synthesis and fabrication aim to create well-coupled junctions with cellular systems so that their stimulation may be achieved.[5,6] Besides, there is a rising demand for non-apoptotic therapeutic effects arising from such material stimulation.[5] To achieve this, we looked for a material property associated with the modulation of biological systems, an area in which silicon has held prominence until now. One drawback of silicon, however, is its degradation under physiological conditions, expensive and intricate fabrication methods and its lack of pseudocapacitive coupling.[7,8] Furthermore, silicon circuits or devices cannot be printed and require nanofabrication techniques for development. Moreover, in comparison to the semiconductor industry, bioelectronics or modulation prioritizes functionality over precision fabrication. Hence,

there is a demand for a paradigm shift in bioelectronic fabrication to techniques with more functionality, such as laser- and 3D printing.

Silicon carbide (SiC) has been a material of significant importance in the semiconductor industry, apart from being a well-known abrasive. Despite the exploration of silicon carbide for both mainstream electronics and its mechanical strength, its utility in biological modulation from an electrochemical or electronic perspective is largely unexplored. Proportional to its existing utility, SiC synthesis methods range from conventional high-temperature inorganic methods like the Acheson process to those from organic precursors such as polysiloxanes.[9-13] SiC is also known to form a plethora of polytypes, though hexagonal 6H and 4H are the most widely-grown and frequently used in electronics. Though the hexagonal polytypes have been well utilized, the cubic 3C polytype is much preferred due to its high mobility, thermal conductivity and saturation drift velocity.[14] However, 3C-SiC being metastable, it cannot be grown in large quantities or with a high level of quality, as its growth requires a non-equilibrium condition.[14-16] Hence, laser ablation holds promise for the synthesis of such a non-equilibrium phase, given an appropriate choice of precursor material.

In this work, we demonstrate two- and three-dimensional laser printing of 3C-SiC using PDMS as a precursor. We introduce a layer-by-layer three-dimensional fabrication method using laser writing for printing 3C-SiC. This technique enables the incorporation of nitrogen as a dopant, making the electrode capable of exhibiting pseudocapacitive charging. We further propose a dual modification strategy to this synthetic method for

tuning material properties (Fig.2.1). This strategy involves using additives in the initial raw material—or a surface functionalization of the final active material—to obtain a different set of optoelectronic properties to ultimately influence the cellular level stimulus in response to light absorption. To demonstrate this strategy, we used bulk molybdenum disulfide (MoS_2) as a starting material additive and manganese dioxide (MnO_2) for the surface functionalization. MoS_2 being a hydrophobic lubricant-like material [17,18], it can blend well with the PDMS precursor base. Moreover, it can increase the local temperature by exothermically oxidizing to a volatile MoO_3 without incorporating itself into the material.[19] This makes MoS_2 a candidate for testing the phase formation during laser printing by manipulating the temperature. MnO_2, on the other hand, is a good photocatalyst that enables us to modify the surface catalytic activity. As a consequence of using MoS_2 as an additive in PDMS, we obtained crystal phase mixing and excessive nitrogen doping in SiC, whereas the surface MnO_2 coating on cubic SiC only enhanced the electrochemical reaction. This demonstrates that additives control the crystal formation, structure, and doping, whereas surface modification tunes the electrochemistry. Either of these strategies shows potential as a tuning gear for expanding material synthesis for various biological systems in the context of laser ablation synthesis.

2.2. Structural characteristics of SiC

To understand the crystal phases of SiC formed from PDMS and the PDMS-MoS_2 composite, the isolated crystals were subjected to X-ray scattering and electron diffraction

techniques. Wide-angle X-ray scattering (WAXS) of SiC obtained from PDMS revealed a single phase which indexed to the 3C polytype of SiC (3C-SiC) (Fig. A.1.1a) whereas the one obtained from a PDMS-MoS_2 composite revealed a mixed phase (M-SiC) of both the 3C and 15R polytypes (Fig. A.1.1b). However, specific spots on the sample produced a pattern corresponding to pure 15R polytype, suggesting that phase mixing and separation is evident from MoS_2 addition (Fig. A.1.1c). Similar information was obtained from high-angle annular dark-field image in scanning transmission electron microscopy (HAADF-

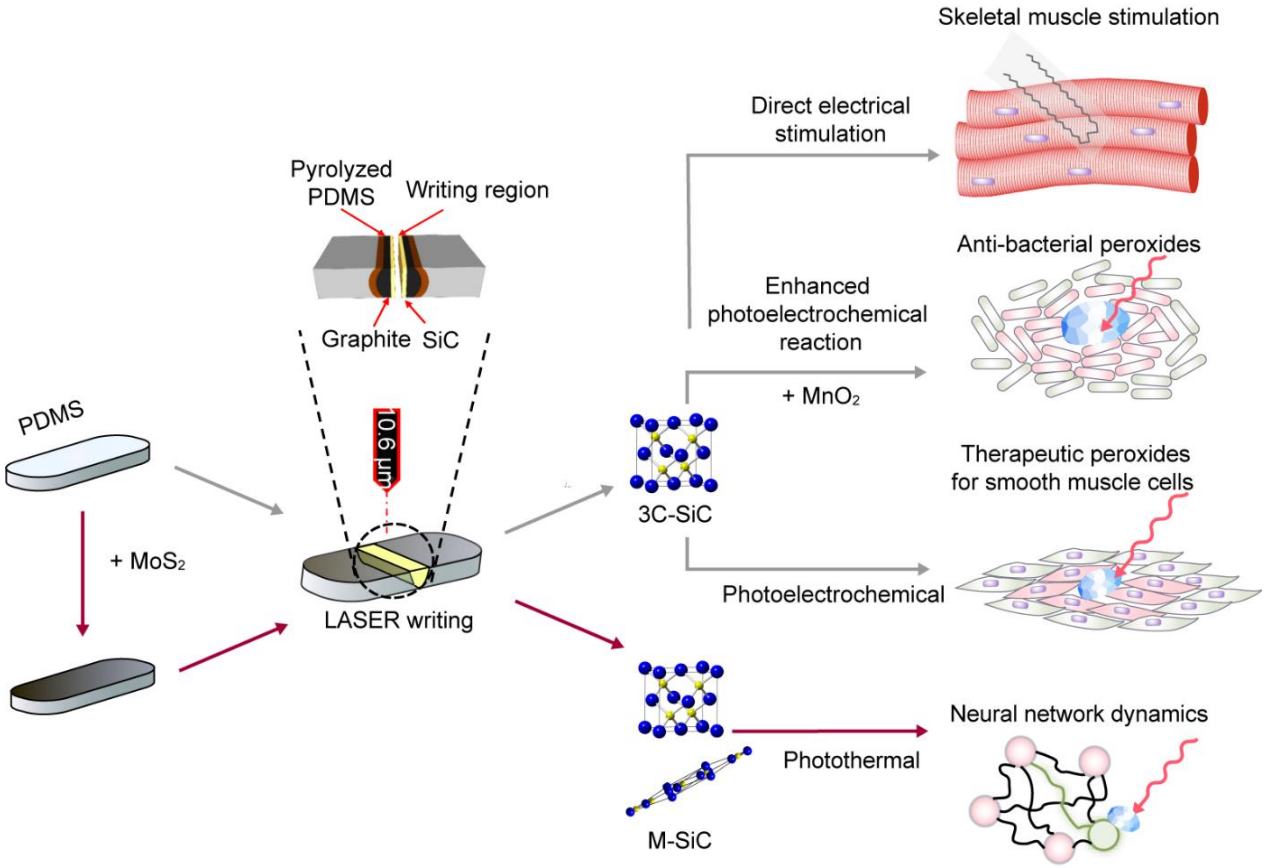

Fig. 2.1. A schematic illustration showing the emergence of the multi-functionality in a bio-interface from an underlying modification in synthetic methodology. A straightforward synthesis by laser ablation gives nitrogen-doped 3C-SiC which can exhibit pseudocapacitive coupling for wired electrical stimulation of skeletal muscles. However, as a free-standing species, the 3C-SiC electrode can perform

Fig. 2.1. continued. photoelectrochemical production of hydrogen peroxide for modulation of smooth muscle cells. The addition of a surface coating of MnO_2 by electroless deposition enhances the photoelectrochemical reaction causing the production of hydrogen peroxide to shift to a lethal dosage useful as an anti-bacterial. In contrast, the use of a starting material additive like MoS_2 tunes the crystal structure and doping thereby generating a photothermal property useful for spatio-temporal neural network modulation. This demonstrates how an additive can tune crystal structure and doping versus the surface functionalization controlling the electrochemistry. Thus, by using a starting material additive and surface functionalization as basic tuning gears we can expand the utility of this laser synthetic methodology to obtain modified materials with unique properties to suit the stimulation requirements of specific biological systems and pathways.

STEM) (Fig. 2.2.c,f) and from indexed selected area electron diffraction (SAED) (Fig. 2.2.b,e) performed on microtomed crystal sections (Fig. 2.2.a,d). Electron Backscatter

Diffraction (EBSD) point analysis done on various ensembles of crystal grown at an ablation site in PDMS resulted in a purely cubic phase across the surface, indicating the phase purity of the sample in this case (Fig. A.1.2). This phase purity—and the existence of 3C or the cubic phase in direct ablation—is consistent with previous studies wherein cubic phases are known to nucleate and grow only under non-equilibrium conditions.[15,16] Using our method, we have noted a non-equilibrium case as the laser ablation method applies a very high amount of energy in a short time span. Furthermore, a statistical analysis of multipoint EBSD phase analysis on various batches of SiC from PDMS-MoS_2 composite resulted in approximately ~ 66% 3C polytype, 30% 15R polytype, and 4% 4H polytype (Fig. A.1.2). This phase mixing and separation could be attributed to the highly exothermic oxidation experienced by MoS_2 to form a highly volatile MoO_3 during the laser ablation process.[19] Such a strongly exothermic reaction would create temperature

instabilities causing some re-crystallization of the initially formed phases to provide rhombohedral and hexagonal phases.[15,16]

To further analyze the composition of the crystals, atom probe tomography was performed on 3C-SiC and M-SiC. This composition analysis revealed the presence of nitrogen doping in both structures (Fig. 2.2.g) along with an absence of molybdenum in M-SiC. Further reconstruction and profiling of nitrogen along the depth of an atom probe tip produced a constant average nitrogen doping of ~ 200 ppm in 3C-SiC (Fig. 2.2.g). However, M-SiC showed a ten-fold increase in the doping concentration along with a gradation along with the depth of the atom probe tip (Fig. 2.2.g). Given that, the atom probe tip is fabricated (Fig. A.1.3) such that its pointed edge is from the surface and its base from the interior to the ablation point. The temperature increases with MoS_2 superposes on an existing temperature gradient leading to enhanced energetics for increased nitrogen doping from the atmosphere following this gradient, compared to the case without MoS_2 (Fig. A.1.4). The superposition of an exothermic reaction onto an existing temperature gradient assists in changing the doping concentration. This is supported by the fact that molybdenum is a nitrogen-fixing catalyst and that following its catalytic action it is removed as a highly volatile MoO_3 [20], causing limited interference with the material structure and properties. Furthermore, the temperature gradient from laser ablation was also observed to affect the chemical conversion of PDMS to SiC as regions far from the point of ablation formed a graphite layer beneath the SiC (Fig. A.1.4). Thus, from a device design standpoint, such temperature gradients are beneficial.

2.3. Two- and three-dimensional printing

We sought not only to understand the structural properties of the material, but to explore the utility of this technique in two- and three-dimensional printing. As a pre-patterning test, we explored the role of laser power and the number of points per inch in controlling the average crystallite sizes (Fig. A.1.5). The test suggested cut-off parameters for synthesis and a significant control on crystallite sizes with laser power and number of points per inch. With this information, we are able to use the laser writing technique for printing fine patterns or circuits, as demonstrated in Fig. 2.3.b. Any painting or pattern (Fig. 2.3.a) could be vectorized and printed using technique. Furthermore, using Raman mapping of nitrogen defect luminescence, we were able to further verify the patterns as being composed of 3C-SiC (Fig. 2.3.c).[21,22] For three-dimensional printing we demonstrated a layer-by-layer printing technique (Fig. 2.3.d-g) similar to UV-based 3D printing. However,

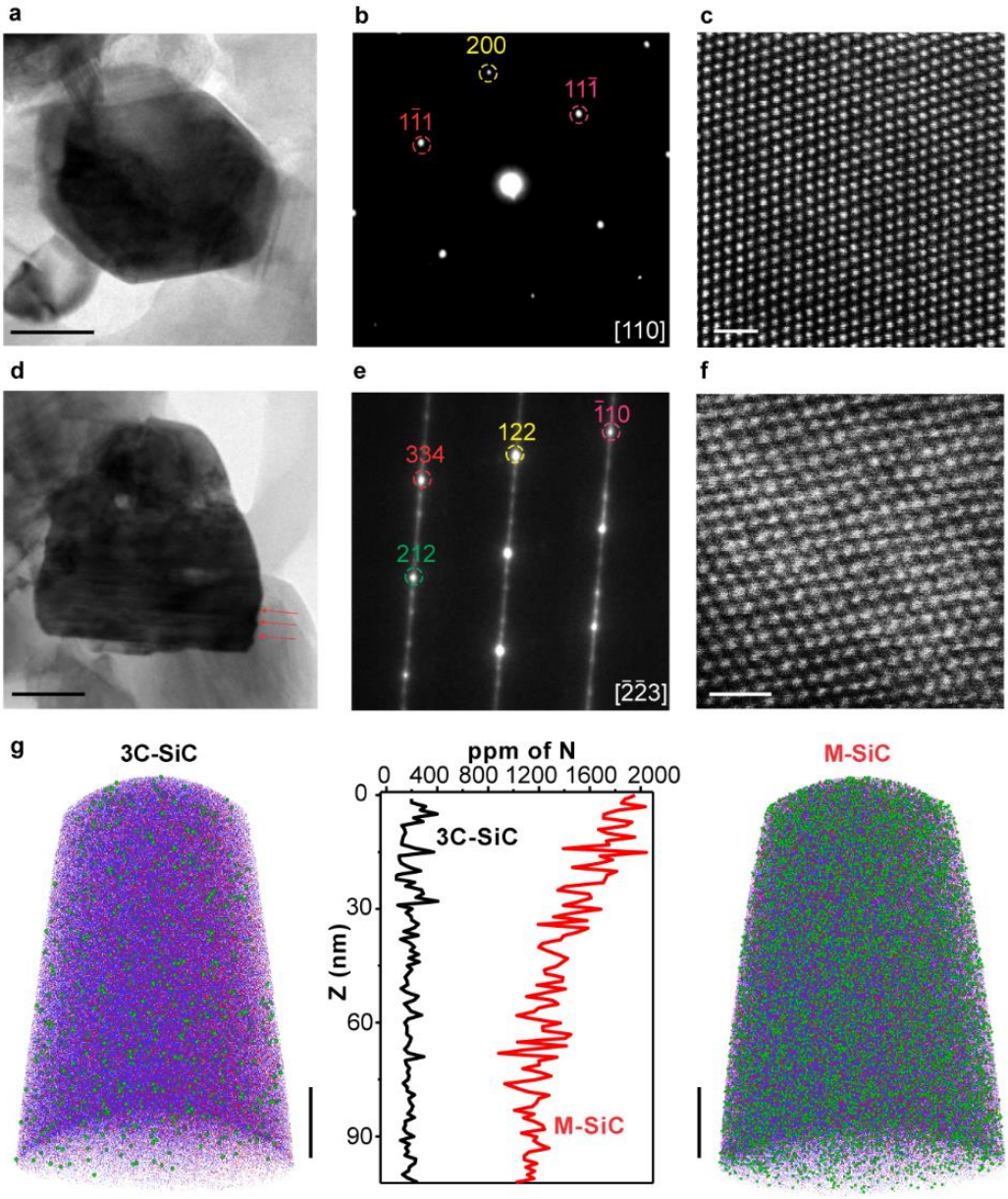

Fig. 2.2. The crystal structure of the SiC was analyzed using microtomed sections of crystals and by performing electron diffraction and STEM on the samples. For the direct synthesis where 3C-SiC was purely formed, it is verified by performing electron diffraction on a section (a) to obtain a pattern (b) and STEM lattice image (c) which indexes to the 110 zone. Similar analysis on M-SiC revealed primarily 3C phase (Supplementary Figure 1), however, the existence of 15R as a separate secondary phase was observed similarly in an analysis from (d) to (f) revealing a [-2-23] zone with twinning (Selected twin planes marked by red arrows in d). Atom

Fig. 2.2. continued. probe tomography reconstruction (g) of 3C-SiC and M-SiC (Red- Si, Blue-C, Green- N) were performed to discover the presence of nitrogen doping. The dopant nitrogen was profiled along the z-direction of atom probe needles for either species revealing a 10-fold increase in doping along with a decreasing gradation in M-SiC. This decreasing gradation overlaps with the temperature gradient created by the ablation laser and grades away from the laser ablation spot into the PDMS bulk (Supplementary Figure 9). (Scale bars: a-100 nm, c-1 nm, d- 50 nm, f- 1nm, g-20 nm)

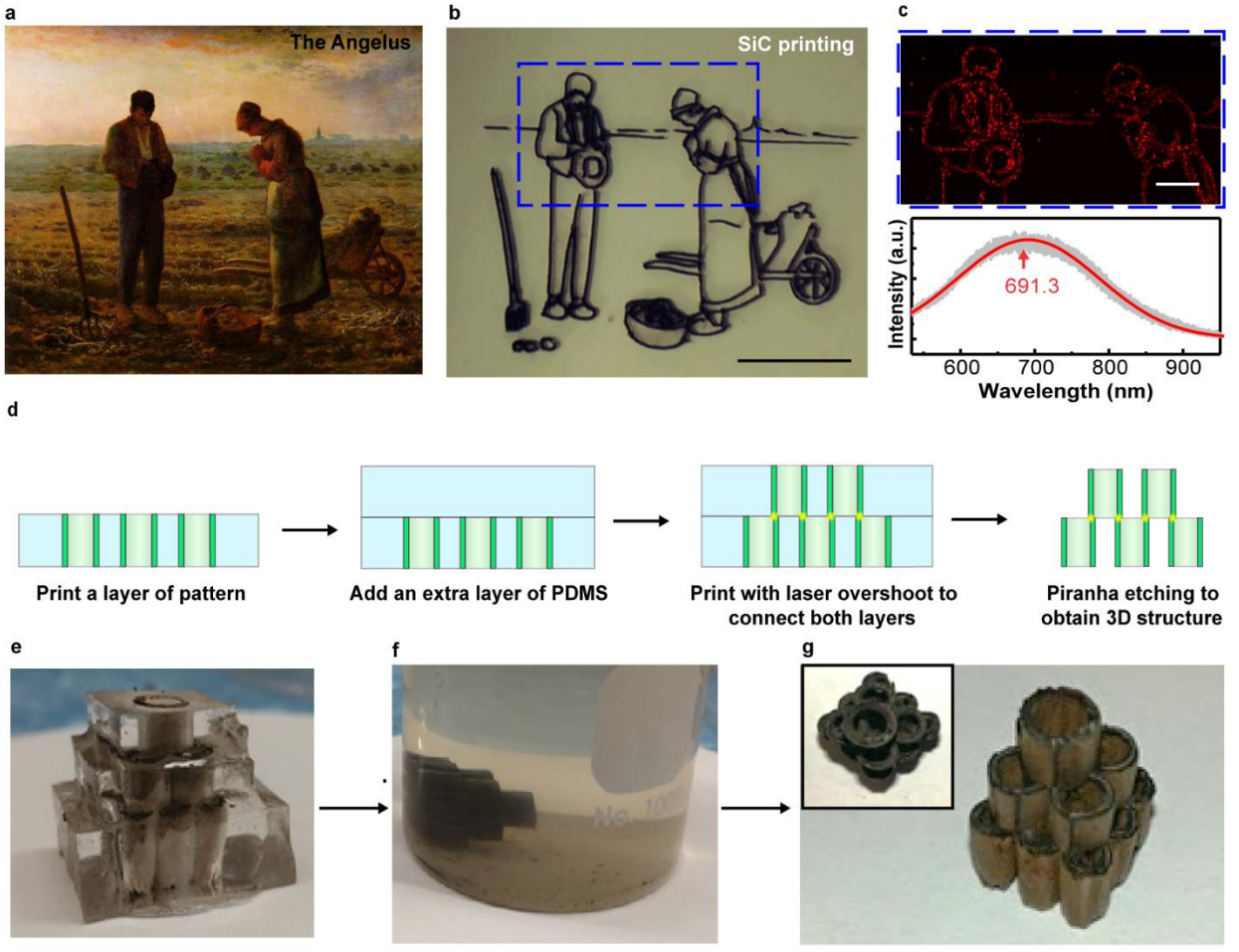

Fig. 2.3. The patterning utility of the laser printing technique is demonstrated by printing a SiC pattern. Thus, a chosen painting (a) is vectorized and laser printed on PDMS to obtain a 3C-SiC pattern (b). The presence of SiC formed during such a laser printing process is verified by Raman photoluminescence mapping (c) by integrating the intensity between 600 and 800 nm. Illustration of utility in three-dimensional printing is done using a layer by layer printing technique as depicted in (d). The layer by layer technique involves printing a layer followed by printing

Fig. 2.3. continued. another layer on top such that there is a laser overshoot from the layer above to below. The laser overshoot could be spatially controlled such that they weld together the SiC in each layer at specific locations. The weld (Indicated by yellow in d) is strong enough that they are stable in harsh acidic environment used to etch the leftover PDMS as seen in (f). Ultimately after etching such a layer by layer stack (e), we can obtain a free-standing interlinked 3D architecture made of 3C-SiC (g). (Scale bars: b – 1 cm, c – 2 mm)

this technique is cleaner and easier as we do not use photopolymerizing agents and the technique can be performed in solid state.[23] Furthermore, we simply modulated the power of the laser to overshoot and weld various layers of 3C-SiC embedded in PDMS to obtain an integrated architecture.

2.4. Circuits with pseudocapacitive coupling for electrical stimulation

To explore the electrochemical properties of the 3C-SiC interface, cyclic voltammograms (CV) were carried out in 1X phosphate-buffered saline (PBS). The cyclic voltammograms collected at various scan rates demonstrated a distinct difference with respect to the standards used (Fig. 2.4.b,c). The skewed square-like shape of CV and the decreasing trend of differential capacitance from 6.28 mF/cm^2 to 4.67 mF/cm^2 and 3.50 mF/cm^2 with an increasing scan rate from 50 mV/s to 100 and 200 mV/s, is indicative of a pseudocapacitive charging in 3C-SiC (Fig. 2.4.a).[24] Moreover, the order of a mF/cm^2 in differential capacitance is three orders of magnitude greater than double-layer capacitance reported on conventional conductive electrodes.[7,25] This means that the Faradaic component of the charge storage available in 3C-SiC is due both to its nitrogen-doped electronic structure and surface properties, making it a superior electrode for forming well-coupled capacitive junctions with cells. Furthermore, the in-situ formation of

a graphite layer underneath the 3C-SiC is what portrays these circuits as ready-to-use electrodes because they act as interfacing electrodes with excellent conductivity (Fig. A.1.4, A.1.5). The utility of such electrodes is demonstrated by direct in vivo electrical stimulation of skeletal muscle (Fig. 2.4.d). Electrical pulses were delivered through a printed 3C-SiC device placed on the skeletal muscle of the rat limb. Action potential recordings on the same tissue revealed in-phase signals to stimulation (Fig. 2.4.e) suggesting a successful stimulation of the skeletal muscle.

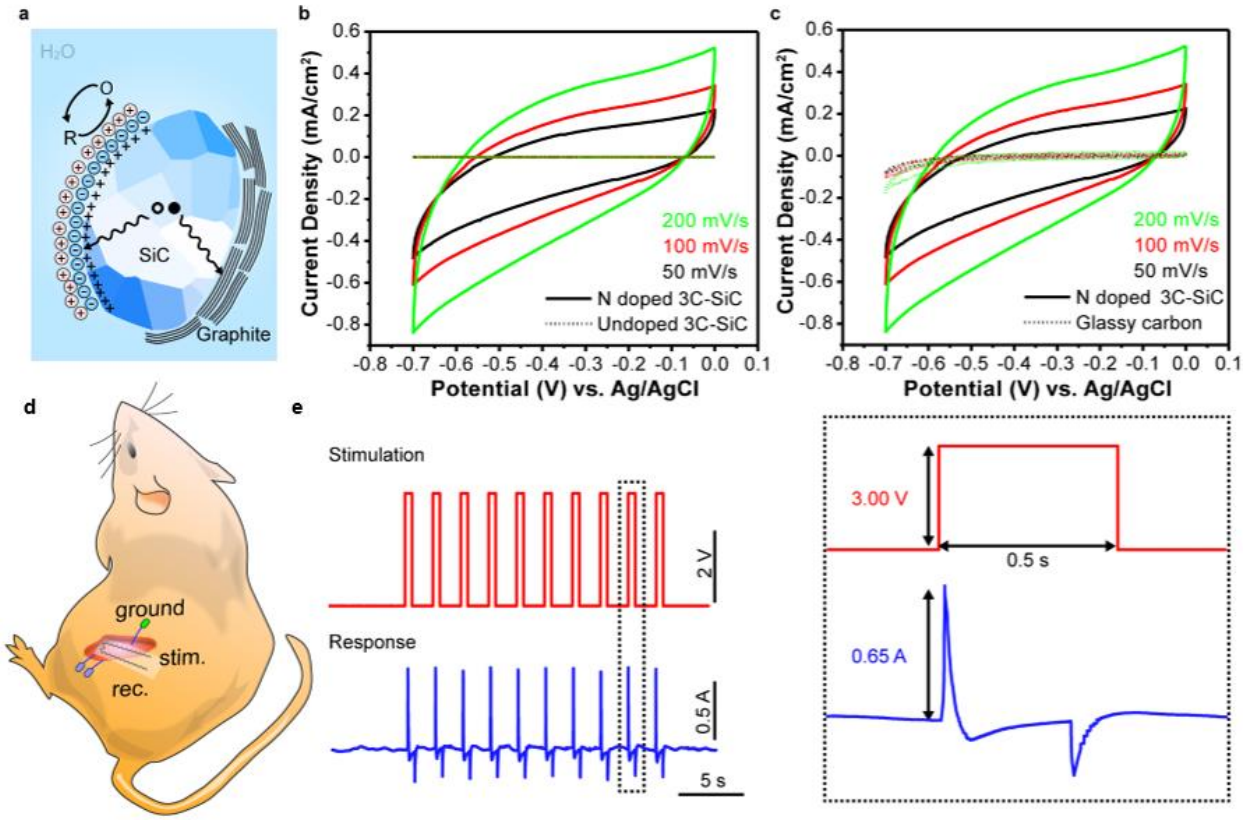

Fig. 2.4. a. Schematic illustration of SiC-graphite interfaces wherein crystals have ribbon-like graphite emerging from them on a nanoscale as observed from STEM imaging (Supplementary Figure 11) and their capability in exhibiting pseudocapacitance. The utility of 3C-SiC as a pseudocapacitively coupled

Fig. 2.4. continued. biointerface is demonstrated by the cyclic voltammograms (b, c). A comparison of cyclic voltammograms with undoped 3C-SiC and standard glassy carbon suggest that the faradaic component giving rise to pseudocapacitance arises purely from nitrogen doping and in SiC. Further, the capability of such printed pseudocapacitive electrodes in direct wired stimulation is illustrated by passing a stimulation current pulse to elicit in-phase action potentials in rat skeletal muscle (d, e).

2.5. Photoelectrochemical characteristics of 3C-SiC

Typically, the surface and its composition would influence the electrochemical properties, which are critical for forming well-coupled biointerfaces along with their functionality. To account for these properties, we characterized the valence band position of all synthetic products using ultraviolet photoelectron spectroscopy (UPS). The valence band edge estimated using UPS (Fig. A.1.6) is given with respect to the standard hydrogen electrode as 1.86 eV for 3C-SiC, 2.48 eV for 3C-SiC-MnO_2 and 1.19 eV for M-SiC (Fig. 2.5.a).[26] Single-channel photocurrent measurements were used to determine the nature of functionality that the interfaces would exhibit with optical excitation. The 3C-SiC electrodes exhibited a photoanodic oxidative reaction, confirmed by the negative direction of the faradaic current and its invariance with the holding level (Fig. 2.5.c).[6] Furthermore, this photoanodic oxidation reaction is enhanced ~ 10-fold by the electroless deposition of MnO2 on the 3C-SiC surface (Fig. A.1.7). Given the n-type nature of the 3C-SiC and their upward band bending at the electrolyte interface (Fig.2.5.b), the photocurrent measurements for 3C-SiC and 3C-SiC-MnO_2 showing photoanodic oxidation is consistent.[27] Hence, a qualitative comparison of UPS determined valence band edge with standard redox potentials for the two- and four-electron oxidation of water reveals an

overlap of 3C-SiC valence band edge with water oxidation to hydrogen peroxide (Fig. 2.5.a).[26,28] This suggests water oxidation to hydrogen peroxide as a potential reaction that we are measuring in our single-channel photocurrent measurements. Furthermore, to verify the functionality of 3C-SiC and the hypothesis of hydrogen peroxide production, we undertook fluorescence kinetics studies. These studies confirmed the production of hydrogen peroxide by 3C-SiC, and the kinetics showed its saturation with time (Fig. 2.5.d, A1.8). However, for 3C-SiC-MnO_2, the hydrogen peroxide production is more than 3C-SiC, suggesting a catalytic role for MnO_2. This idea is supported by a more positive valence band edge of 3C-SiC-MnO_2, thermodynamically favoring more oxidation of water to hydrogen peroxide. Furthermore, the difference in the quantity of hydrogen peroxide produced also discriminates their role in biology—3C-SiC provides a therapeutic dose, though 3C-SiC-MnO_2 provides a lethal dose, hence its utility in anti-bacterial applications (Fig. A.1.9).

2.6. Biomimicry of 3C-SiC as an endothelial cell

From a cardiovascular perspective, hydrogen peroxide or reactive oxygen species (ROS) plays a unique role in the control of smooth muscle cells.[29-31] Endothelial cells that form the lining of arteries and veins sense pressure and use nitric oxide to signal smooth cells to regulate their contraction-relaxation cycles. [49] However, studies have revealed that the direct addition of hydrogen peroxide could also elicit a similar response mediated via regulation of inositol triphosphate receptors (IP3R) (Fig. 2.5.e). [32,33] Thus, we carried out investigations on an ensemble of smooth muscle cells and studied the calcium signals of

individual cells as a consequence of 3C-SiC stimulation. Calcium signals of individual cells in the region of stimulation were analyzed, such that their response could be separated into stationary and oscillatory. Here, we have classified “stationary” cells as those which fire action potentials with very long periods (~1 contraction cycle per 2-3 minutes) and “oscillatory” cells as those which fire faster (~3-4 contraction cycles per minute).[34] As a consequence of stimulation—or exogenous hydrogen peroxide availability to cells—we see an immediate calcium spike for stationary cells (Fig. 2.5.f-i) whereas for oscillatory cells the response depends on where the stimulation happens with respect to the last calcium peak or contraction state. The oscillatory cells respond to hydrogen peroxide in three ways, depending on whether the stimulation happens in its relaxed state (Fig. 2.5.f-ii), immediately after contraction (Fig. 2.5.f-iii) or just after reaching a relaxed state (Fig. 2.5.f-iv). These responses are a phase shift (delay in next firing) in oscillation, or a transient frequency increase, or an increase in frequency followed by damping to higher calcium level, respectively (Fig. 2.5.f). These perturbations in oscillatory responses are consistent with experimental and theoretical studies of smooth muscle behavior that occur with an increase of inositol triphosphate (IP3).[31]

Fluorescence kinetics (Fig. 2.5.d) has demonstrated the production of hydrogen peroxide, which is known to directly increase IP3 by binding to G-protein coupled receptors (GPCR).[34] GPCR activation leads to an increase in cytosolic IP3 which regulates IP3R which opens in a cyclic fashion modulated by cytosolic calcium levels.[34] Such a biphasic regulation of IP3R by cytosolic calcium leads to oscillation in cytosolic calcium and transmembrane chloride current.[34] The opening of this transmembrane chloride channel

causes depolarization via the uptake of exogenous calcium and the release of calcium from internal storages like the endoplasmic or sarcoplasmic reticulum.[32-34] Thus, putting together our cellular calcium perturbation observations with these existing facts, we can confirm the IP3-based signaling mechanism involved. Further, the capability of hydrogen peroxide produced by 3C-SiC in modulating smooth muscle contraction cycles illustrates its biomimicry as an endothelial cell.

Besides, observation of a stimulated sheet of cells reveals an overall increase in calcium levels (Fig. 2.5.g,h). This increase, observed as IP3R activation, leads to exogenous calcium uptake and an internal store release of calcium leading to depolarization of cells. Such an overall calcium level increase on an ensemble level manifests on the cellular level in different ways as observed in Fig. 2.5.f. Further exploration of correlations of calcium signals on an ensemble of stimulated smooth muscle cells by analyzing mean synchronization between them reveals an increase in synchronization post-stimulation. This also illustrates the increased synchronization in a contraction of an ensemble of smooth muscles consistent with increased calcium levels, illustrating the functionality on an ensemble level (Fig. A.1.10).

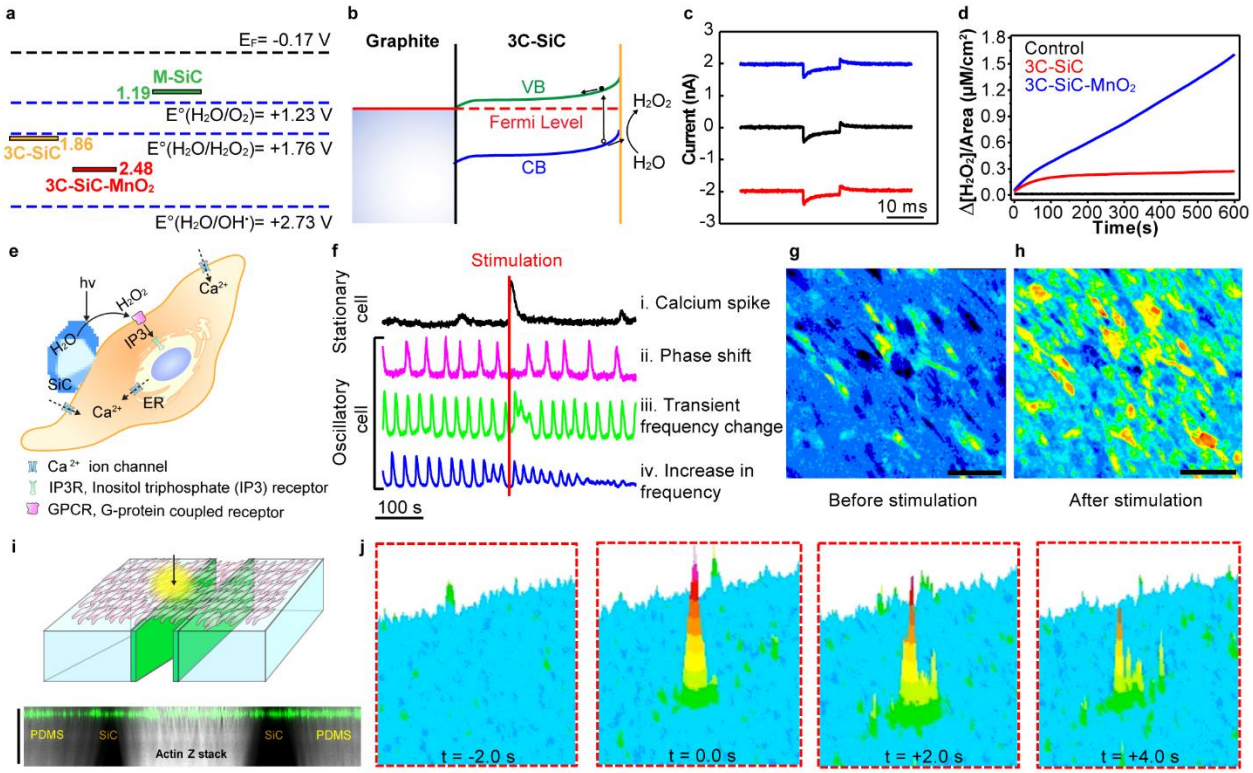

Fig. 2.5. HOMO levels of 3C-SiC, 3C-SiC-MnO_2 and M-SiC measured using UPS to a standard hydrogen electrode (a) revealing the incapability of M-SiC in performing an electrochemical oxidation reaction, versus 3C-SiC and 3C-SiC-MnO_2. The n-doping in 3C- SiC and M-SiC and their interfacing with graphite (an electron sink) suggests the possibility of pure oxidation reactions as a consequence of photostimulation (b). Photocurrent measurements on 3C-SiC at various holding levels for a 10 ms pulse revealing a photoanodic oxidation reaction (c). Further, the measurement here is invariant to holding level confirming a faradaic process. Fluorescence kinetics measurements were done on 3C-SiC and 3C-SiC-MnO_2 confirm the water oxidation to hydrogen peroxide and show the relative concentration of hydrogen peroxide produced by oxidation of water (d) per cm^2 of the material irradiated with light. A schematic illustration of the consequence of exogenous hydrogen peroxide on smooth muscle cells (e). Exogenous peroxides cause increased activation of IP3R causing a release of calcium from internal stores like ER/SR and uptake of exogenous calcium. The difference in calcium signaling on a cellular level, as a consequence of peroxide release on a sheet of cells, depend on the stimulation timing with respect to a contraction cycle that confirms the role of peroxide and IP3R activation in individual cells (f). The ensemble measurements were carried out on a sheet of smooth muscle cells (Supplementary Figure 18). The differential calcium ($\Delta F/F$) signals observed before (g) and after (h) stimulation reveals an overall increase in calcium levels

Fig. 2.5. continued. (Represented as heat maps) along with an increased synchronization in the contraction of a sheet of smooth muscles (Supplementary Figure 18). A device-level implementation of the same (i) and a point stimulation on the device (Supplementary Figure 24) reveals a calcium wave propagating (Represented as heat maps) from the stimulation point (j). (Scale bars: g- 100 µm, h- 100 µm, i - 100 µm)

Furthermore, we demonstrated the device-level scaling of this phenomena by growing smooth muscle cells on a device to form a uniform layer (Fig. 2.5.i), and then further stimulating them to produce localized calcium waves (Fig. 2.5.j). This suggests a device-based therapeutic utility in delivering hydrogen peroxide.[29-32]

2.7. Spatiotemporal synchronization of neuronal networks:

M-SiC consisting of mixed-phase and excess nitrogen doping demonstrated a weak photothermal effect. Further, the photothermal effect is characterized by portraying a growing photocurrent with an applied stimulation (Fig. 2.6.a, A1.7). To justify this observation, the surface composition of all synthesized materials was compared using X-ray photoelectron spectroscopy (XPS). The surface composition revealed the presence of 21% surface oxide and 1% nitride defects in 3C-SiC, which increased to 30.4% and 3.75%, respectively, in M-SiC (Fig. A.1.11, A.1.12). The increased presence of oxide and nitride surface defects in M-SiC could potentially justify their weak photothermal capability—apart from the excessive doping (~2000 ppm nitrogen) they have in bulk. Besides, M-SiC has a valence band edge much higher than all possible water oxidation reactions (Fig. 2.5.a) which explain its capability in portraying the photothermal effect due to its inability in performing any photoelectrochemical reaction. This may be attributed to

a change in electronic structure at the surface due to excessive doping, defects and higher surface phonon density as verified in low-loss electron energy loss spectroscopy (EELS) (Fig. A.1.13).

In addition to exploring the utility of the 3C-SiC and photoelectrical effect from nanomaterials, we look forward to a system with which to test the photothermal effect of M-SiC. Being sensory, dorsal root ganglia neurons (DRG) are known to respond to heat as a stimulus.[6,35] Moreover, the fact that photoelectrochemical stimulation has poor spatial confinement due to diffusion of stable molecular species provides thermal effects with a significant edge (Fig. 2.6.b) when it comes to spatio-temporal control. Thus, the effect of such a thermal stimulus in modifying network-level properties with spatiotemporal regulation is important to neuromedicine.[35,36] Herein, we culture DRG networks (Fig. 2.6.c, f) with M-SiC crystals dispersed in culture to form stable and biocompatible biointerfaces with networks. The biointerface formation explored through a scanning electron microscope (SEM) revealed the capability of M-SiC crystals to form entangled junctions with axons (Fig. 2.6.d) in addition to dendrites wrapping around them (Fig. 2.6.e). Furthermore, we explored the synchronization changes introduced by a single stimulation on a single node of a DRG network (Fig. 2.6.f). Such stimulation caused increased local synchronizations around that node and an overall increase in the average synchronization index on the entire network. These are clearly visible in the synchronization plots before and after stimulation with the rearrangement and expansion of clusters around the stimulated neuron (Neuron ID: 12, indicated by an arrow in Fig. 2.6.g).

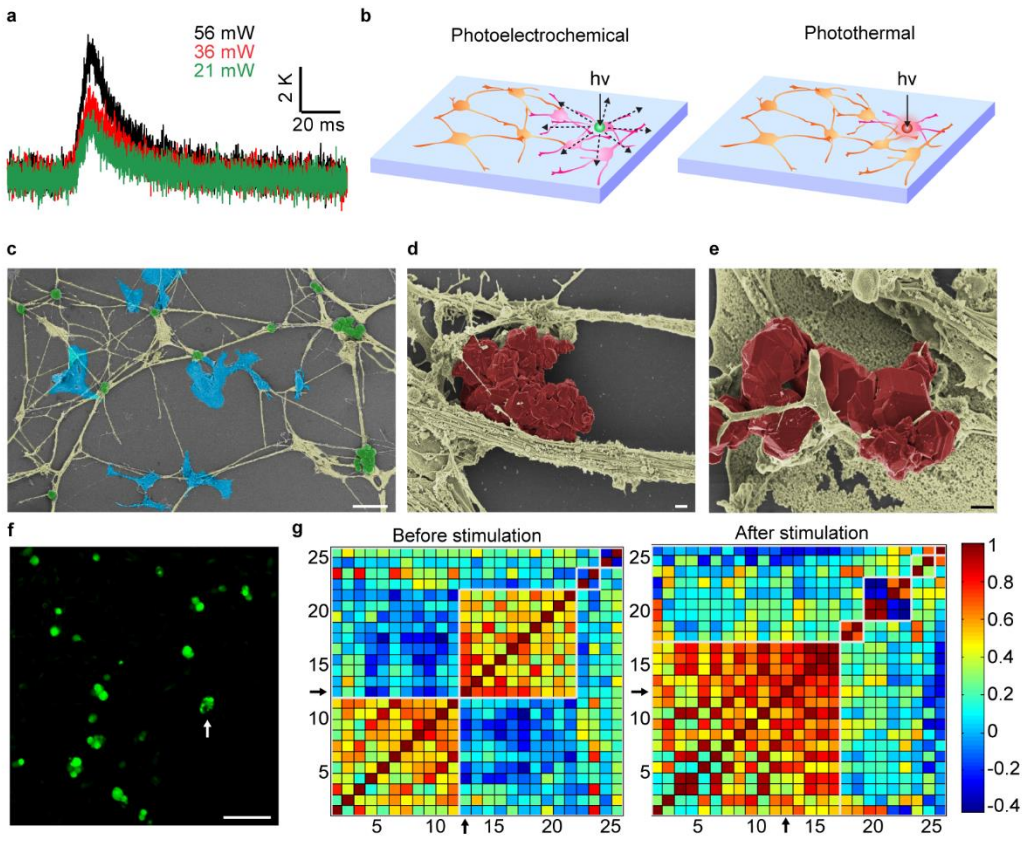

Fig. 2.6. The photothermal capability of a mixed-phase and excessively doped M-SiC is observed through single-channel recordings (a) for a stimulation pulse of 10 ms and various powers of a 532 nm stimulation laser. The advantage of such a photothermal measurement over photoelectrochemical (b) is that electrochemically generated species can eventually diffuse across and stimulate other neurons in a network resulting in poor spatio-temporal control whereas thermal gradients decay fast. Interfaces formed by an artificial cultured dorsal root ganglial network were explored using SEM imaging and false coloring. A typical neuronal network (c) has neurons (blue) interlinked by axons and dendrites (yellow) with few glial cells (green). M-SiC particles interspersed with the growth medium have been observed to be entangled with axons (d) and dendrites (e) as observed in SEM imaging. Calcium imaging was performed on a conventional neuronal network (f) with a single node stimulation (5.3 mW, 1 ms) to see how localized synchronization surrounding the stimulated node rises (g) with respect to the unstimulated case. Such spatially controlled increases in local synchronization results in an increase in the mean synchronization of the entire neural network from 0.197 to 0.338. This illustrates the capability of M-SiC to form interfaces with neural networks and to modulate synchronizations locally

Fig.2.6. continued. compared to drugs that modify neural networks globally. X-axis and Y-axis in (g) are neuron indices along with the heat map for synchronization values. (Scale bars: g- 100 µm, h- 100 µm, i - 100 µm)

Furthermore, the mean synchronization index increased from 0.197 to 0.338 after stimulation. This observed change or difference suggests how one could spatiotemporally control neural network synchronization by photothermal stimulation compared to conventional drugs which stimulate networks globally. Hence, in the future this demonstration could be used for precision medicine in regaining synchronization in networks of nerve injury, regional neuromodulation or even degenerative diseases like Alzheimer's, etc. [35,36]

2.8. Conclusion

This work has demonstrated two and three -dimensional laser printing of 3C-SiC along with the multimodal synthetic capability of laser ablation synthesis. This strategy and technique illustrate the idea of developing nitrogen-doped silicon carbide circuits as pseudo-capacitively coupled biointerfaces and freestanding electrodes for hydrogen peroxide production. We also obtained a significant understanding of the spatiotemporal modulation of correlated neural networks. These demonstrations reveal the future utility of such silicon carbide frameworks for organ or organoid-on-chip type research and applications. Furthermore, this work opens up opportunities in laser-assisted three-dimensional printing for the development of pharmaceutically relevant systems. The discovery of an anti-bacterial effect using a 3C-SiC-MnO2 hybrid in the presence of white light illumination paves the way for its future utility in solar bacterial disinfection. In a

broader sense, the work introduces potential design principles in material synthesis for developing biointerfaces with specific capabilities to address targeted biological problems

2.9. Experimental Methods

Synthesis of PDMS and PDMS-MoS_2 composite:

PDMS was prepared using commercially available Sylgard 184 kit. The polymer and curing agent were mixed in 10:1 ratio by weight and degassed in vacuum. Following the degassing process, they are cured in a vacuum oven at 80 °C for at least 8 hours. For PDMS-MoS_2 composite preparation the polymer, curing agent and bulk MoS_2 powder (Sigma Aldrich) (10:1:0.5 ratio by weight) were mixed into homogenous mixture by a magnetic stirrer. This was followed by vacuum degassing and curing at 80°C for 8 hours. Samples were always re-prepared in case of defects arising due to improper degassing.

Laser ablation of PDMS to SiC:

PDMS layers were mounted on an aluminum comb (With a supporting layer of glass or polystyrene petridish) and laser written with a CO_2 laser of 10.6 μm wavelength, upto a power of 50 W (VLS 460 manufactured by Universal Laser Systems) with a 100 μm spot size. The pattern for writing was generated as a vector image in Corel draw and printed using VLS 460 software. The writing was done in vector cutting mode with parameters for crystal structure and property analysis being 100% power (50 W), 1000 points for inch and 0.254 mm/s speed. However, for pattern printing the power is lowered to 5% (5 W) and 0.254 mm/s speed. (Warning: Using no supporting layer or thin samples of PDMS

would cause laser to hit the aluminum comb below and melt and even contaminate your samples)

Processing SiC for characterization and analysis:

Samples prepared with 100% power were generally used for crystal structure and property analysis and for direct integration with cells via dispersion of these crystals in growth media. However, before these processes are carried out the purification process of these crystals are done. The SiC along with the graphite layer formed is cut out from the PDMS matrix using a razor blade. This is followed by washing the sample in toluene (Fisher scientific) for 5 minutes to remove any organic components present in the material. Following this the sample is kept immersed in isopropyl alcohol (Fisher scientific) and then in De-ionized (DI) water for 5 minutes each. After this sequential washing process they are dipped in 1:1 HF:HNO_3 (Sigma Aldrich) to remove any silica and surface organics for 5 minutes. Once this is completed the samples are washed in DI water, nitrogen blow dry and oxygen plasma cleaned at 200 W for 3 minutes (PE-100 Benchtop Plasma System). After the final step the SiC synthesized from pure PDMS would appear yellow and the one with MoS_2 would appear light green.

Electroless deposition of manganese dioxide:

Electroless deposition on purified clean SiC surface was carried out by a solution of 0.25 M $KMnO_4$ (Sigma Aldrich) in 0.5 M H_2SO_4 (Sigma Aldrich). The samples were washed in water and ethanol (1:1) mixture and then kept dipped in the above mixture for 10 minutes. The samples are then washed in water and nitrogen blown dry.

X-ray scattering studies:

Off -axis wide angle x-ray scattering (WAXS) was carried out on SAXS LAB Ganesha with a Cu K-alpha radiation source and 50 μm spot size. The SiC crystals from the top layer are scratched off using a clean sharp tip TEM grid handling tweezer and the resulting crystal powder loaded onto a captone tape. The captone tape is mounted on a holder from which X-rays are scattered through the crystals onto a detector.

Electron microscopy and sample preparation:

Sample prep for TEM, STEM and EELS: According the procedure above, the crystals are scratched using a tweezer and the resulting powder loaded into a resin mold. The mold is then filled with epoxy resin and degassed in vacuum and baked at 60 °C overnight for embedment. The crystals are then microtomed (Leica UC6) into 100 nm sections and loaded on 200 mesh copper grids. The grids were stored in a vacuum desiccator. Transmission electron microscopy and selected area electron diffraction (SAED) patterns were collected on a JEOL 3010F operating at an accelerating voltage of 300 kV with a LaB6 filament. Scanning Transmission Electron Microscopy (STEM) and Electron energy loss spectroscopy (EELS): STEM and EELS were done on a JEOL ARM 200CF (Cs corrected) with a field emission gun at an accelerating voltage of 200 kV. STEM and EELS measurements were done on each area after a 200 kV, 30 min beam shower at the spot to remove any adsorbed hydrocarbon contaminants. EELS was collected using a Gatan dual EELS detector at magic angle. Scanning Electron Microscopy, EDS and Electron backscattered diffraction (EBSD) were all done on TESCAN LYRA3 system equipped

with Dual Oxford Instruments X-Max-80 silicon drift x-detectors for EDS and Oxford Instruments NordlysMax2 EBSD detector. The EBSD patterns were processed and indexed using Oxford AZTEC software.

Indexing of SAED and FFT patterns:

3C-SiC and 15R-SiC structures were generated in Crystal Maker 2.0 using existing reported structures [37] and the indexing of patterns were carried out using Crystal Diffract 2.0.

X-ray photoelectron spectroscopy (XPS) and Ultraviolet photoelectron spectroscopy (UPS):

XPS and UPS were performed on Thermo Scientific ESCALAB 250Xi equipped with an electron flood gun and argon ion sputter gun. The XPS measurements were done using an Al K-alpha X ray source of 1.487 keV energy and the spot size of 500 μm in diameter. The UPS measurements were done using a He I source of UV radiation of 21.2 eV energy and the spot size of 3 mm in diameter.

Atom probe tomography (APT) and sample preparation:

SiC crystals were sputter coated with 50 nm nickel to prevent charging during focused ion beam (FIB) milling process. The crystals were then milled into a small lamella on FEI Helios. These lamellas were transferred to silicon microposts using a micromanipulator and milled down to needles for atom probe tomography. These needles were then mounted into a LEAP 400X Si (Cameca) and charged to a potential between 1 to 6 kV.

Following this the surface atoms were evaporated using 355 nm laser pulses of 30 pJ at a frequency of 250 kHz in a chamber maintained at 30 K and 2 x 10-11 torr. The three-dimensional structures were reconstructed and analyzed using Cameca's integrated visualization and analysis software (IVAS) 3.4 code.

Photocurrent measurements:

Photocurrent measurements were performed by single channel voltage clamped recordings on a patch-clamp amplifier (Axopatch 200B) set up. The material of interest was immersed in 1X PBS (Fisher Scientific) in a petridish and focused on using a microscope (Olympus BX61WI) with a water immersion lens (20X/0.5 NA). Light pulses are delivered through the microscope from two different sources: (a) 375 nm LED source (Thorlabs M375L4, ~ 500 µm spot size) and (b) 532 nm laser (Laser glow, diode -pumped solids state laser, ~5 µm spot size). Light pulses were delivered to these light sources using a digitizer (Molecular devices, Digidata 1550). For measuring the photocurrent measurements glass pipettes of ~ 1 MΩ were pulled (Sutter Instrument, P-97) and their tip lowered and focused onto the same optical plane (Gap of ~2 µm) as the material surface before the stimulation pulse is applied. The voltage clamped currents were recorded in parallel with the stimulation pulse at various holding current levels. This data was analyzed and the nature of the photocurrents determined using a previously developed method (6). For analysis of photothermal currents the same pipette used for recording was calibrated for its resistance as a function of temperature. For this measurement the pipette was dipped in pre-heated PBS at approximately 50-60°C and

allowed to cool down naturally as the resistance were recorded alongside temperature, using a thermocouple.

Photoluminescence measurements:

Raman measurement of photoluminescence from SiC was performed for laser written patterns and crystals to understand the presence of defect related emissions present in the system. The PL measurements were done using a 473 nm excitation laser with detection in a back-scattered geometry with a 50X/0.5 NA objective and 600 grooves/mm grating, under ambient conditions. Point spectra were collected for crystals and mapping was done on patterns which were laser printed. The instrument used for measurements were on a Horiba LabRAM HR Evo Confocal Raman.

Fluorescence kinetics:

Fluorescence kinetics experiment was carried out with SiC crystals to understand the photo redox species produced in solution. To understand the production of hydrogen peroxide Amplex Red peroxide/peroxidase kit was used according to the manufacturer's instructions. In order that the same excitation is used for the dye emission and the photoanodic process we attach or suspend our crystals facing the excitation source and on the edge of the cuvette as illustrated in the photograph below such that all the fluorescent signal is transferred to the detector at 90 degree without any obstruction. The beam of the spectrometer is a rectangular one with ~ 0.21 cm^2 area.

Electrochemical measurements and I-V characteristics:

A purified piece of graphite- SiC layer was isolated and attached to a wire using conductive silver paste on the graphite side. The wire, contact and the graphite side along with edges were sealed using nail polish or epoxy and dried overnight such that only the SiC crystals are exposed to the electrolyte. The projected area of the SiC crystals exposed were ~0.09 cm^2, standard glassy carbon (CHI104) electrode was ~0.07 cm^2 and that of undoped 3C-SiC wafer (MTI corporation- SiC-3CP-a-4-13-05050525-2.2) was 0.25 cm^2. Cyclic voltammograms (CV) were carried out at 200, 100 and 50 mV/s scan rates from -0.7 V to 0.0 V in 1X PBS on a Bio-Logic SP-200 potentiostat. The current was scaled with respect to the area of electrode and the area in a cycle of CV estimated by integration in Origin Pro 8.0. Further the differential capacitance of the electrode was calculated using the equation $\partial C/\partial A = (1/f\Delta V) \int J \, dV$. Where J is the current density, V the potential, f is the scan rate, ΔV the potential window of scan. The I-V characteristics is measured by a Keithley source meter 2636A.

Muscle stimulation experiment:

Device fabrication: A PDMS film was prepared with a thickness of 100 μm on slide glass by spin coating followed by curing at 100 °C for 30 min. The PDMS film is mechanically peeled off and transfer on to acrylic. For conversion of PDMS to SiC, laser scan with a predefined pattern at 100% power (50 W), 1000 points for inch and 0.254 mm/s speed. Remove residual PDMS film by mechanical peel-off or chemical etching. The residual part could be removed with piranha treatment for 2 hours, and then the native oxide

etched with HF treatment for 10 min. To remove amorphous debris, the sample can be treated with O2 plasma (200 W, 10 min) and HF and HNO3 mixed solution (1:1, 2 hours). Silver paste or solder can be used to make a connection with wires, and PDMS solution added onto the connection points and cured at 115 °C.

Animal experiment: An adult rat is anesthetized using ketamine (60 mg/kg)/xylazine (5 mg/kg) cocktail. A cut is made on the rear dorsal skin and the device and probes inserted onto a skeletal muscle. Using a pulse generator an input square pulse of 3 V (Measured with respect to 0V ground) is applied into the rat's muscle between the SiC device and an electrode. The recording of stimulation current as a consequence of the direct electrical stimulation is done between an electrode and ground attached to the same muscle. The recording signal electrode was connected to a digitizer (Molecular devices, Digidata 1550) for read out.

Human aortic smooth muscle culture:

Primary human aortic smooth muscle cells were purchased from ATCC (ATCC PCS-100-012) and cultured in Medium 231 (Life Technologies) 500 mL of which is supplemented with 25 mL growth supplement (SMGS) (Life Technologies) and 50 µg/mL of sodium L-ascorbate (Sigma Aldrich) for extracellular matrix secretion. The cells were seeded at a density of 1.25 x 10^4 /mL and used within the first three passages. The glass and PDMS surfaces were coated with collagen before seeding. The PDMS surfaces were oxygen plasma cleaned at 200 W for 10 minutes immediately before seeding collagen to make the surface hydrophilic.

Dorsal root ganglial (DRG) neuronal network culture and bio-interface studies:

Dorsal root ganglias were harvested from P0-P3 Sprague-Dawley rat pups into ice cold DMEM/F12 (Thermo Fisher 11320033). The ganglias were then digested in 2.5 mg/mL trypsin (Worthington TRL3) in EBSS with no Ca/Mg (Thermo Fisher 14155063) for exactly 20 minutes in a 37°C shaker incubator. The ganglias were then centrifuged at 1500 rpm for 2 min and separated from trypsin and resuspended in EBSS with 10% FBS. The ganglias are mechanically triturated using fire polished pasteur pipettes of decreasing sizes and centrifuged down at 1500 rpm for 2 min. After removing the supernatant, the cells were resuspended in complete media (DMEM/F12 with 1% pen-strep, 5 % FBS along with 20 μM 5-fluoro uracil (Sigma Aldrich) and 50 ng/mL of NGF 2.5S (Thermo Fisher). The glass bottom dishes for seeding are covered with 0.01% poly-L -lysine in molecular biology grade water for 20 min, washed with water and aspirated dry with vacuum. The cells are seeded on this dish according to required concentration. For bio-interface studies with M-SiC the crystals are scratched out from the graphite layers and washed in 100% ethanol and dried overnight under a UV lamp in a bio-hood. The crystals are then re-dispersed in the complete media by bath sonication. The media is changed for the DRG culture network to the one with M-SiC within 24 hrs of the initiation of the culture and stimulation experiments performed within the next 24 hrs after this.

Immunofluorescence staining:

The cell cultures were fixed with 4% paraformaldehyde in PBS for 10 minutes and then washed in PBS thrice. Following this they were permeabilized with 0.5% Triton X-100 for 10 minutes and washed in PBS thrice. After the cells are fixed and permeabilized they were incubated in a blocking solution of 3% BSA in PBS for 60 minutes following which 2 drops/mL of ActinGreen 488 ReadyProbes (Invitrogen) was added to the blocking solution. The solution was incubated for another 30 minutes with the actin stain before washing and imaging in PBS.

Calcium imaging:

Calcium imaging was done using Fluo4-AM (Invitrogen) which was made into a 50 μM stock solution in Pluronic F-127 which is in 20% DMSO (Invitrogen). Cell were incubated with 2 μM Fluo4-AM in media for 30 minutes and washed post-incubation with media. The cells were further incubated for 15 minutes in media before beginning imaging. The calcium imaging was carried out at a rate of 3.8 Hz with a resolution of 512 x 512 pixels per frame on a LEICA SP5 STED-CW confocal microscope in a 37°C incubator.

Confocal stimulation experiments:

Point stimulation experiments were carried out in the FRAP mode of a LEICA SP5 STED-CW confocal microscope with a 592 nm laser. The stimulation was done for 1 ms and at varying powers.

SEM imaging of Dorsal Root Ganglial (DRG) networks:

DRG networks culture were fixed in 2.5% glutaraldehyde in PBS (pH = 7.2) over night. Then washed in a series of increasing concentration of ethanol each for ten minutes, beginning 20% in water till 100%. The samples are then critical point dried (Leica EMCPD300). The samples are then sputter coated with 8 nm platinum and palladium, following which they are imaged on a Carl Zeiss Merlin SEM at 2 kV.

Neural network data analysis:

The neural network calcium data was analyzed using LASX (Leica application software). The region of interests (ROIs) were marked to identify the neuronal soma and the calcium traces extracted from it. The raw calcium traces were further processed to ΔF/F for each soma in the neural network. The ΔF/F data was then smoothed using a savitzky-golay filter and baseline corrected for bleaching effects using a convex -envelope method on Peak Caller software package.[38] The processed ΔF/F curves were further processed on Peak Caller for generating the synchronization matrices, mean synchronization index, calcium waveforms and raster plots. Peak Caller package was run on MATLAB R2018b engine.

Smooth muscle stimulation data analysis:

The smooth muscle calcium data was analyzed using LASX (Leica application software). The Region of interest (ROIs) were drawn around smooth muscles identified across regions near and away from stimulation. The raw calcium traces were used to study bio-physical understanding of peroxide induced perturbations on calcium oscillations. For device stimulation studies the calcium channels videos were converted into tiff stacks

using Fiji-ImageJ. The stacks were then converted into ΔF/F image and the surface plots generated on Fiji-ImageJ. Synchronization analysis was done similar to the neural network analysis.

Anti-bacterial experiments:

Escherichia coli (E.coli) MG1655 was obtained from the American Type Culture Collection (ATCC). E.coli was cultured to log phase in Luria-Bertani (LB) media and harvested by centrifugation at 3000 rpm. Following which it is washed twice with Phosphate Buffered Saline (PBS) and suspended in LB medium, PBS or deionized (DI) water to ~ 106 c.f.u. ml^{-1} separately. The 3C-SiC-MnO2 crystals were then added to this bacteria culture and mixed uniformly. Photocatalytic disinfection was performed using a white light-emitting diode of 5 mW power for 24 hrs. Bacteria concentrations were then measured after 24 h illumination using standard spread-plate techniques. Each sample was serially diluted and each dilution was plated in triplicate onto LB plate and incubated overnight at 37℃. The experiments for the disinfection were also conducted in duplicate with 3C-SiC-MnO_2 under dark conditions (Control 1) and without 3C-SiC-MnO_2 under LED light illumination (Control 2).

References

1. Morales, A. M.; Lieber, C. M. A Laser Ablation Method for the Synthesis of Crystalline Semiconductor Nanowires. Science 1998, 279 (5348), 208–211.

2. Ye, R.; Han, X.; Kosynkin, D. V.; Li, Y.; Zhang, C.; Jiang, B.; Martí, A. A.; Tour, J. M. Laser-Induced Conversion of Teflon into Fluorinated Nanodiamonds or Fluorinated Graphene. ACS Nano 2018, 12 (2), 1083–1088.

3. Luong, D. X.; Yang, K.; Yoon, J.; Singh, S. P.; Wang, T.; Arnusch, C. J.; Tour, J. M. Laser-Induced Graphene Composites as Multifunctional Surfaces. ACS Nano 2019, acsnano.8b09626. https://doi.org/10.1021/acsnano.8b09626.

4. Stanford, M. G.; Li, J. T.; Chyan, Y.; Wang, Z.; Wang, W.; Tour, J. M. Laser-Induced Graphene Triboelectric Nanogenerators. ACS Nano 2019, 13 (6), 7166–7174.

5. Dai, X.; Hong, G.; Gao, T.; Lieber, C. M. Mesh Nanoelectronics: Seamless Integration of Electronics with Tissues. Acc. Chem. Res. 2018, 51 (2), 309–318.

6. Jiang, Y.; Li, X.; Liu, B.; Yi, J.; Fang, Y.; Shi, F.; Gao, X.; Sudzilovsky, E.; Parameswaran, R.; Koehler, K.; et al. Rational Design of Silicon Structures for Optically Controlled Multiscale Biointerfaces. Nat Biomed Eng 2018, 2 (7), 508–521.

7. K. J. Yu, D. Kuzum, S. Hwang, B. H. Kim, H. Juul, N. H. Kim, S. M. Won, K. Chiang, M. Trumpis, A. G. Richardson, H. Cheng, H. Fang, M. Thompson, H. Bink, D. Talos, K. J. Seo, H. N. Lee, S. Kang, J. Kim, J. Y. Lee, Y. Huang, F. E. Jensen, M. A. Dichter, T. H. Lucas, J. Viventi, B. Litt, J. A. Rogers, Bioresorbable silicon electronics for transient spatiotemporal mapping of electrical activity from the cerebral cortex. Nat. Mater. 15, 782-791 (2016).

8. Yu, K. J.; Kuzum, D.; Hwang, S.-W.; Kim, B. H.; Juul, H.; Kim, N. H.; Won, S. M.; Chiang, K.; Trumpis, M.; Richardson, A. G.; et al. Bioresorbable Silicon Electronics for Transient Spatiotemporal Mapping of Electrical Activity from the Cerebral Cortex. Nature Mater 2016, 15 (7), 782–791.

9. Burns, G. T.; Taylor, R. B.; Xu, Y.; Zangvil, A.; Zank, G. A. High-Temperature Chemistry of the Conversion of Siloxanes to Silicon Carbide. Chem. Mater. 1992, 4 (6), 1313–1323.

10. Nakajima, Y.; Hayashi, S.; Katayama, A.; Nedyalkov, N.; Terakawa, M. Femtosecond Laser-Based Modification of PDMS to Electrically Conductive Silicon Carbide. Nanomaterials 2018, 8 (7), 558.

11. Amorós, P.; Beltrán, D.; Guillem, C.; Latorre, J. Synthesis and Characterization of SiC/MC/C Ceramics (M = Ti, Zr, Hf) Starting from Totally Non-Oxidic Precursors. Chem. Mater. 2002, 14 (4), 1585–1590.

12. Weimer, A. W. Carbide, Nitride and Boride Materials Synthesis and Processing; Chapman & Hall: London, 1997.

13. Zou, X.; Ji, L.; Lu, X.; Zhou, Z. Facile Electrosynthesis of Silicon Carbide Nanowires from Silica/Carbon Precursors in Molten Salt. Sci Rep 2017, 7 (1), 9978.

14. La Via, F.; Severino, A.; Anzalone, R.; Bongiorno, C.; Litrico, G.; Mauceri, M.; Schoeler, M.; Schuh, P.; Wellmann, P. From Thin Film to Bulk 3C-SiC Growth: Understanding the Mechanism of Defects Reduction. Materials Science in Semiconductor Processing 2018, 78, 57–68.

15. Knippenberg, W.F. Growth phenomena in silicon carbide. Philips Research Report. 1963, 18(3), 161–274.

16. Jepps, N. W.; Page, T. F. Polytypic Transformations in Silicon Carbide. Progress in Crystal Growth and Characterization 1983, 7 (1–4), 259–307.

17. V. Nair, A. Kumar, C. Subramaniam, Exceptional photoconductivity of poly(3-hexylthiophene) fibers through in situ encapsulation of molybdenum disulfide quantum dots. Nanoscale. 22, 10395-10402 (2018).

18. V. Nair, K. Kumar, C. Subramaniam, Mechanochemically controlling the van der Waals gap in molybdenum disulfide nanosheets. Phys. Rev. Materials. 3, 0158021-0158926 (2019).

19. C. K. Gupta, D. Sathiyamoorthy, Fluid bed technology in materials processing (CRC press, 1998).

20. L. Han, X. Liu, J. Chen, R. Lin, H. Liu, F. Lü, S. Bak, Z. Liang, S. Zhao, E. Stavitski, J. Luo, R. R. Adzic, H. L. Xin, Atomically dispersed molybdenum catalysts for efficient ambient nitrogen fixation. Angewandte Chemie International Edition. 58, 2321–2325 (2019).

21. H. W. Shim, K. C. Kim, Y. H. Seo, K. S. Nahm, E.-K. Suh, H. J. Lee, Y. G. Hwang, Anomalous photoluminescence from 3C-SiC grown on Si (111) by rapid thermal chemical vapor deposition. Applied Physics Letters. 70, 1757–1759 (1997).

22. W. J. Choyke, D. R. Hamilton, L. Patrick, Optical properties of cubic SiC: luminescence of nitrogen-exciton complexes, and interband absorption. Physical Review. 133, A1163 (1964).

23. R. D. Farahani, M. Dubé, D. Therriault, Three-Dimensional Printing of Multifunctional Nanocomposites: Manufacturing Techniques and Applications. Adv.Mater. 28, 5794-5821 (2016).

24. Y. Zou, A. S. Walton, I. A. Kinloch, R. A. W. Dryfe, Investigation of the Differential Capacitance of Highly Ordered Pyrolytic Graphite as a Model Material of Graphene. Langmuir. 32, 11448–11455 (2016).

25. Nair, V.; Kumar, A.; Subramaniam, C. Exceptional Photoconductivity of Poly(3-Hexylthiophene) Fibers through in Situ Encapsulation of Molybdenum Disulfide Quantum Dots. Nanoscale 2018, 10 (22), 10395–10402.

26. Chun, W.-J.; Ishikawa, A.; Fujisawa, H.; Takata, T.; Kondo, J. N.; Hara, M.; Kawai, M.; Matsumoto, Y.; Domen, K. Conduction and Valence Band Positions of Ta 2 O 5 , TaON, and Ta 3 N 5 by UPS and Electrochemical Methods. J. Phys. Chem. B 2003, 107 (8), 1798–1803.

27.Krishnan Rajeshwar. Fundamentals of Semiconductor Electrochemistry and Photoelectrochemistry. In Encyclopedia of Electrochemistry; Bard, A. J., Ed.; Wiley-VCH Verlag GmbH & Co. KGaA: Weinheim, Germany, 2007; p bard060001.

28. Siahrostami, S.; Li, G.-L.; Viswanathan, V.; Nørskov, J. K. One- or Two-Electron Water Oxidation, Hydroxyl Radical, or H 2 O 2 Evolution. J. Phys. Chem. Lett. 2017, 8 (6), 1157–1160.

29. Dimmeler, S.; Fleming, I.; Fisslthaler, B.; Hermann, C.; Busse, R.; Zeiher, A. M. Activation of Nitric Oxide Synthase in Endothelial Cells by Akt-Dependent Phosphorylation. Nature 1999, 399 (6736), 601–605.

30. González-Pacheco, F. R.; Caramelo, C.; Castilla, M. Á.; Deudero, J. J. P.; Arias, J.; Yagüe, S.; Jiménez, S.; Bragado, R.; Álvarez-Arroyo, M. V. Mechanism of Vascular Smooth Muscle Cells Activation by Hydrogen Peroxide: Role of Phospholipase C Gamma. Nephrology Dialysis Transplantation 2002, 17 (3), 392–398.

31. Yang, Z.; Zheng, T.; Zhang, A.; Altura, B. T.; Burton M. Altura. Mechanisms of Hydrogen Peroxide-Induced Contraction of Rat Aorta. European Journal of Pharmacology 1998, 344 (2–3), 169–181.

32. Santiago, E.; Climent, B.; Muñoz, M.; García-Sacristán, A.; Rivera, L.; Prieto, D. Hydrogen Peroxide Activates Store-Operated Ca 2+ Entry in Coronary Arteries: Redox Regulation of SOC Entry in Coronary VSM. British Journal of Pharmacology 2015, 172 (22), 5318–5332.

33. Sneyd, J.; Han, J. M.; Wang, L.; Chen, J.; Yang, X.; Tanimura, A.; Sanderson, M. J.; Kirk, V.; Yule, D. I. On the Dynamical Structure of Calcium Oscillations. Proc Natl Acad Sci USA 2017, 114 (7), 1456–1461. https://doi.org/10.1073/pnas.1614613114.

35. Gemes, G.; Rigaud, M.; Koopmeiners, A. S.; Poroli, M. J.; Zoga, V.; Hogan, Q. H. Calcium Signaling in Intact Dorsal Root Ganglia: New Observations and the Effect of Injury. Anesthesiology 2010, 113 (1), 134–146.

36. Aron, L.; Yankner, B. A. Neural Synchronization in Alzheimer's Disease. Nature 2016, 540 (7632), 207–208.

37. Ruska, J.; Gauckler, L. J.; Lorenz, J.; Rexer, H. U. The Quantitative Calculation of SiC Polytypes from Measurements of X-Ray Diffraction Peak Intensities. J Mater Sci 1979, 14 (8), 2013–2017.

38. Artimovich, E.; Jackson, R. K.; Kilander, M. B. C.; Lin, Y.-C.; Nestor, M. W. PeakCaller: An Automated Graphical Interface for the Quantification of Intracellular Calcium Obtained by High-Content Screening. BMC Neurosci 2017, 18 (1), 72.

3. Soft poly-(3-hexyl thiophene) nanofiber biointerfaces for optical and mechanical control of cellular signaling.

3.1. Introduction

Extracellular matrices (ECMs) are known to support a cellular environment with structural integrity and mechanical coupling with the external environment.[1] The structural integrity of cells is important in a tissue or organ as it determines their structure and associated function for the physiological maintenance of that living organism. Mechanical coupling, on the other hand, enables force and topographic transduction leading to signaling in cells.[1-3] Forces transferred to a cell are received by them through membrane proteins which are coupled to the extracellular matrix.[1-3] Thus, the effective force transfer through an extracellular matrix depends on its elastic modulus and the mechanical anisotropy present in it.

Soft extracellular matrix-like material and modulation of their elastic properties through artificial methods have been known to act as transducers for mechanotransduction.[4] However, in such modulation is limited to mechanical force being the stimuli. Hence developing an ECM which can act as a transducer for other forms of stimuli serves as an opportunity to control various signaling pathways in cells. Herein we self-assemble organic semiconductor nanofibers of 20 nm diameter with approximately 1 MPa modulus capable of exhibiting photothermal effects besides softness and topographic mechanotransduction.

The candidate organic semiconductor material here for self-assembly is poly-(3-hexyl) thiophene (P3HT) which π-stack into long fiber-like networks when its solubility is decreased by lowering temperature in a poor solvent.[5-7] These fibers are photothermally active and the temperature generated could be light intensity-modulated with very good Spatio-temporal control. In contrast with the fibers, pristine P3HT films perform photoelectrochemical reduction undergoing self-oxidation.[8] Thus, using such a matrix enables one to superpose mechanotransduction with photothermal or photoelectrochemical transients providing us with artificial functional ECMs.

The application of spatially confined heat impulses to cells has known to be important from a biophysical perspective.[9] This allows one to look at the behavior of a cell and their dynamics in a non-equilibrium state and how the signaling determines the final fate of the cell. Previous studies have determined that photothermal heating changes the capacitance of the lipid bilayer and leading to depolarization.[10] Depolarization often causes calcium fluxes into the cell and the extent of the depolarization can determine the signaling cascade that cells initiate.[10] Besides the amount of heat, the extent of depolarization and calcium fluxes are determined by the excitability of the cell type under consideration. Hence the responses to these should significantly vary between excitable and non-excitable systems.[11] Though photothermal stimulation of excitable systems has been explored extensively the ones with non-excitable remain unexplored.[12] This motivates one to look at non-excitable cellular systems that make up the majority of an organism's structure and function. Moreover, organellar response, their interactomes, and dynamics are largely unknown with a heat stimulus.

In this project, we look at fibroblasts as a model non-excitable system to explore mechanical and photothermal modulation effects on cellular and organelle interactomes. Fibroblasts have been observed to undergo apoptosis with doses of photothermal stimulation. The pathway of apoptosis is carefully studied using calcium signaling, mitochondria-lysosome interaction and the effect of P3HT fiber network topography on caveolin 1 signaling. To demonstrate the utility of this study we perform photothermal and mechanotransductive modulation of apoptotic signaling and test them on triple-negative breast cancer cells. To compare with P3HT fibers we perform similar studies using P3HT sheets capable of exhibiting the photoelectrochemical effect. We microfabricate circular islands of pristine P3HT and demonstrate the interaction of neuronal network with these P3HT patterns through neurites and their photoelectrochemical modulation.

3.2. P3HT nanofibers as an ECM mimicking soft material

Transmission electron microscopy performed on as synthesized P3HT nanofibers reveals fiber like morphology with diameter around ~ 20 nm (Fig.3.1. a). The same was observed using HAADF-STEM imaging as well which gives a better contrast of the morphology as the STEM imaging contrast is based on atomic number and the polymer is sulfur rich (Fig.3.1. b). Further to verify if the π-stacking has led to this structure we perfume cryo-EM to keep the self-assembled structure stable from an electron beam induced heating. In the cryo-EM imaging we observe clear polymeric lamellar stacking which are known to result from an underlying π-stacked structure.[5-7] The observed lamellar spacing of ~ 1.6 nm (Fig 3.1.c) also matches well with the value in literature for P3HT fibers.[7] This fibrillar

morphology of self-assembled P3HT fibers is similar to collagen, thus making P3HT fibers identical in structure to certain extracellular matrix proteins. Besides, the fibrillar morphology, P3HT when spin casted or drop-casted assembles into fiber like network as observed in AFM imaging (Fig.3.1.d). The AFM image further suggests the topography of matrices made of P3HT.

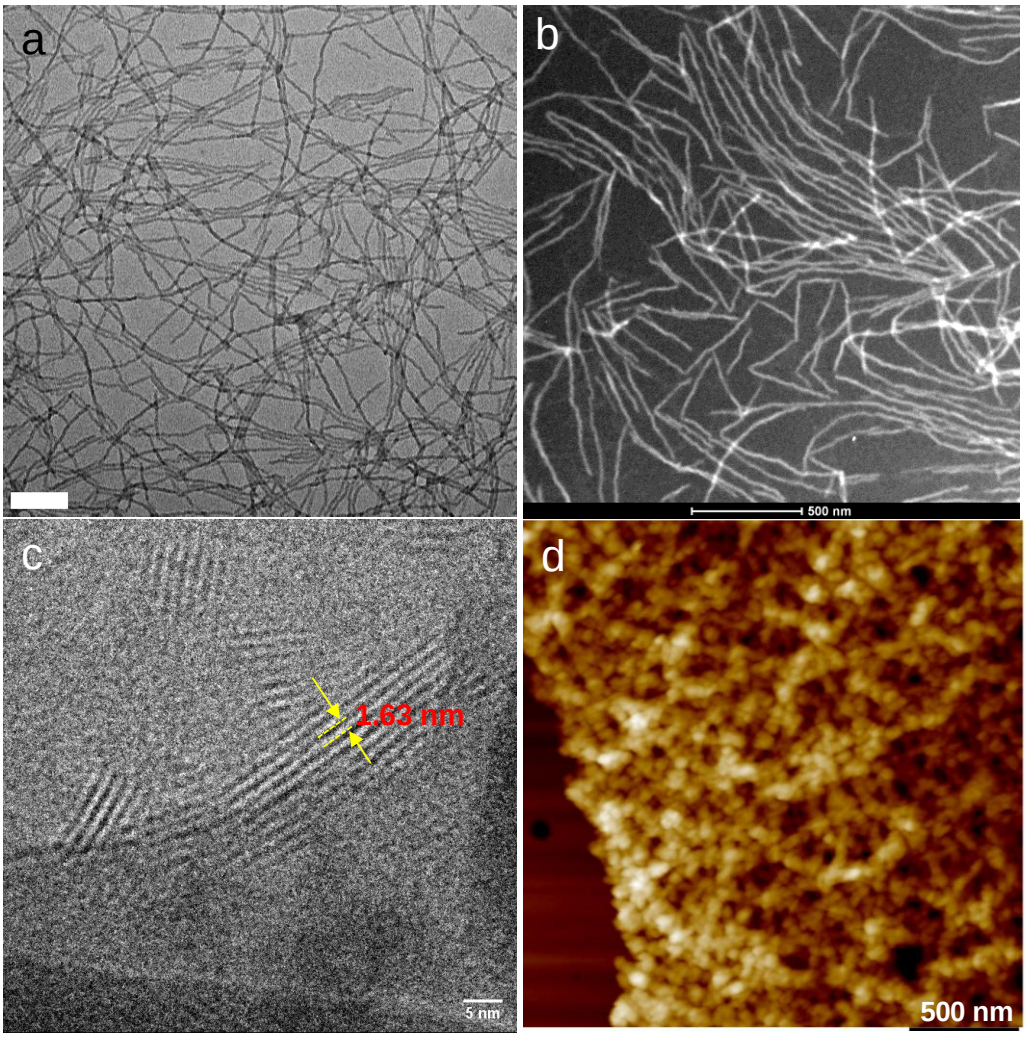

Fig.3.1. a. A TEM image of P3HT nanofibers as-synthesized (Scale bar 100 nm), b. HAADF-STEM image of P3HT nanofibers as-synthesized, c. Cryo-EM image of P3HT nanofiber revealing the interlamellar spacing to be 1.63 nm confirming a π-stacked

Fig. 3.1. continued. structure, d. AFM of spin-casted P3HT fiber matrix revealing the nanoscale topography of the surface on which cells are grown.

Besides morphological similarity mechanical properties should also be a match to understand if the material is capable of mimicking ECM.[13] Thus, we examine the cellular perception of the matrix in comparison with glass, using actin stress fibers and vinculin expression in fibroblasts. Actin stress fibers were reduced along the lamellar region of the cell in regions covered with P3HT though not on glass (Fig.3.2.a,b). This reduction is stress fibers selectively atop P3HT suggest that the cells perceive them as soft. This is because the lamella of a cell doesn't need to recruit a lot of stress fibers to support the cell on a soft substrate compared to hard.[14] This soft perception of P3HT by cells could be further confirmed by observing vinculin expression on focal adhesions. On P3HT the

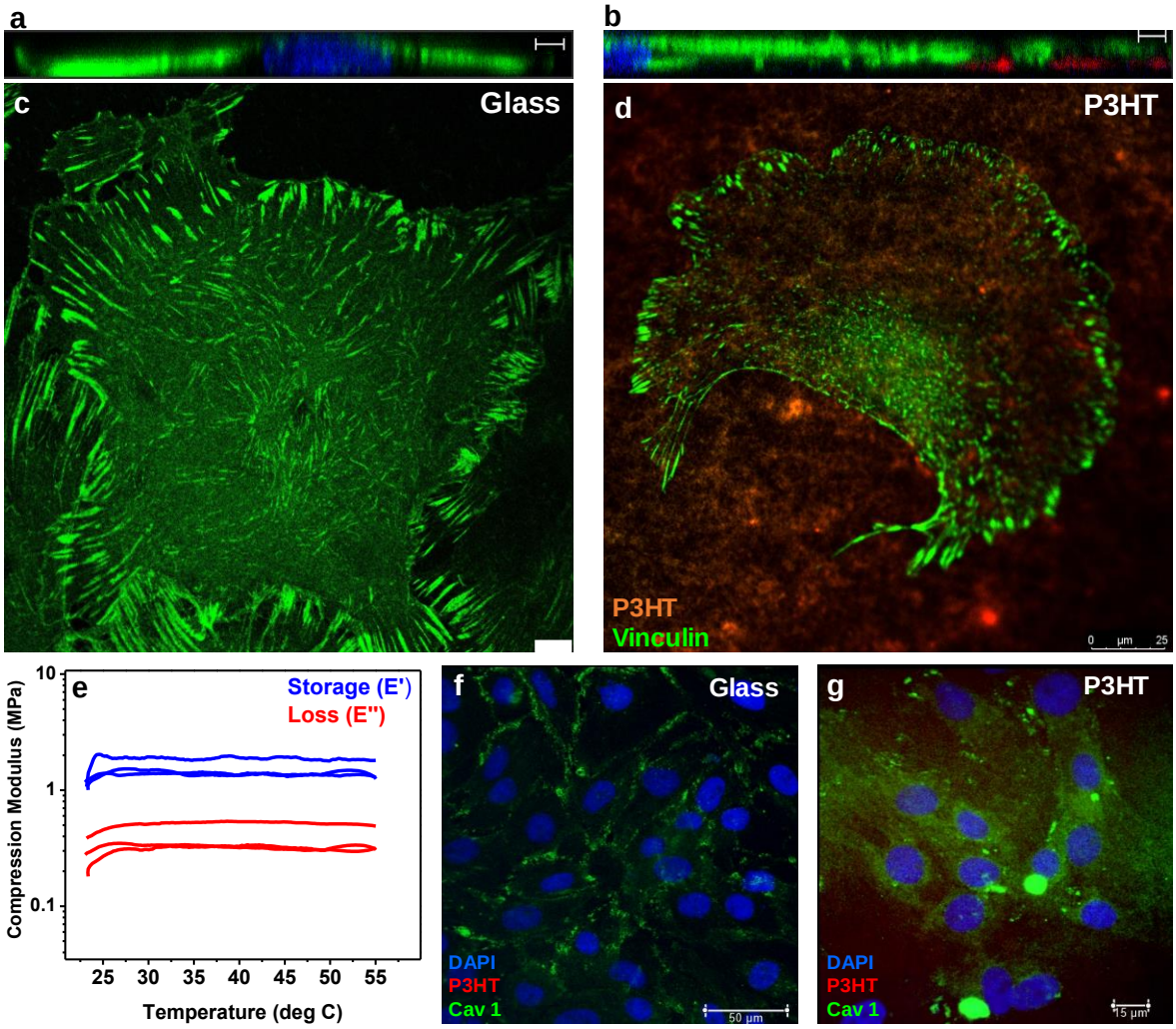

Fig.3.2. a. Z-stack of actin stress fibers in primary rat cardiac fibroblasts on glass substrate (Blue-DAPI, Green-Actin), b. Z-stack of actin stress fibers in primary rat cardiac fibroblasts on P3HT fiber matrix (Blue-DAPI, Green-Actin), c. Vinculin expression in primary rat cardiac fibroblasts on glass, d. Vinculin expression in primary at cardiac fibroblasts on P3HT fiber matrix. e. Compression modulus measurements done as a function of temperature on three different batches of P3HT fiber matrices. The temperature invariance of modulus suggests the stability of the matrix at a wide range of physiological temperatures. Caveolin-1 (Cav 1) expression in primary rat cardiac fibroblasts on (f) Glass substrate and (g) P3HT fiber matrix. (Scale bars: a- 3 µm, b- 3 µm, c-8 µm)

vinculin recruited focal adhesions are more spot like than needles shaped in the nuclear and non-lamellar region on a hard glass substrate (Fig.3.2.c,d). This difference is due to

the fact that vinculin recruitment was reduced on P3HT leading to the formation of shorter and immature adhesions as the substrate is perceived soft.[15,16] Compression modulus measurement done on three different batches of P3HT fiber suggest their modulus to be in the range of 1-2 MPa (Fig.3.2 e). This measured elastic modulus suggests that P3HT is much softer than collagen fibrils which have their modulus in the range of few GPa.[17] Besides this elastic modulus is comparable with that of fibronectin.[18] Furthermore, the temperature invariance of the elastic modulus of P3HT in a wide range of physiological temperatures suggests their thermal stability.

Apart from the rigidity and morphological similarity of P3HT which qualifies it as an ECM mimicking material the topographic feature of the fiber matrix is of importance (Fig.3.1.d). This topographic feature is known to cause caveolin-1 based mechanotransduction.[2] When a substrate has topographic features on it the cell membrane resting on it now has to bend according to these topographic features.[2] This accommodation of cell membrane bending involves invaginations leading to recruitment caveolin-1.[2,3] We observe an increased recruitment of caveolin-1 in non-lamellar on a P3HT matrix compared to glass (Fig.3.2.g) confirming the possibility of topographic mechanotransduction using P3HT. Thus, besides the ECM mimicry, the P3HT nanofiber matrix offers additional mechanotransductive cues as a tuning gear for cellular signaling.

3.3. P3HT nanofiber as an optoelectronically active ECM

Inline to use organic semiconductors to synthesize optoelectronically responsive ECM matrices for additional cues in cellular signaling. The optoelectronic properties of P3HT fiber matrices are explored and compared with pristine planar P3HT. Single-channel patch-clamp recordings with photostimulation were performed to realize the same. With the substrate kept external to pipette with a negative bias the P3HT fibers show a strong photothermal effect with heating that could be tuned by the power of the light stimulus. In contrast, pristine P3HT sheets show a photoelectrochemical reduction. P3HT sheets have been reported to produce reactive oxygen species through photoelectrochemical reduction and by self-oxidation to volatile materials.[8,19] This photo degradability is useful for making devices that naturally degrade without leaving behind toxic side-products leaving biocompatibility unaffected. Besides this is useful towards the future as devices fabricated out of P3HT degrade gradually without the requirement for removal.

To confirm the optoelectronic characteristics of these biointerfaces, inside pipette photocurrent measurements were performed with zero voltage bias. Single channels recording for P3HT fibers yielded no response whereas the pristine P3HT sheets yielded photoelectrochemical reduction profile. This difference is due to the fact the photothermal currents need an existing bias to superpose onto whereas photoelectrochemical currents are generated via a charge transfer process and have standalone currents.[20]

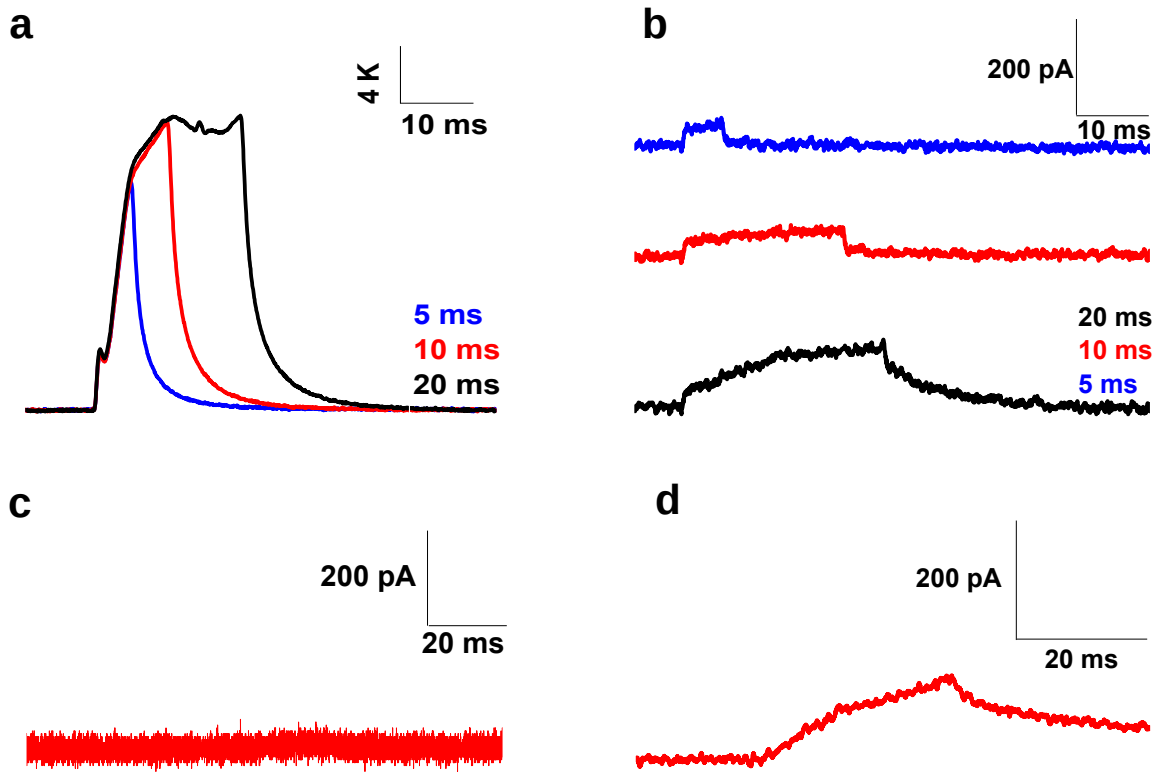

Fig.3.3. a. Photothermal characteristics and temperature profile of P3HT fiber matrices with stimulation of 29 mW using a 532 nm laser with different pulse width. Measurement was done with a bias of -0.5 V with substrate external to pipette. b. Photoelectrochemical reduction characteristics of pristine P3HT sheets withstimulation of 56 mW using a 532 nm laser. Measurement was done with a bias of -0.5 V with substrate external to pipette. c. In-pipette recordings done at 0 V bias for P3HT fibers with a stimulation pulse of 56 mW power, 20 ms pulse width using a 532 nm laser. d. In-pipette recordings done at 0 V bias for pristine P3HT sheets with a stimulation pulse of 56 mW power, 20 ms pulse width using a 532 nm laser.

Moreover, leaky currents are significantly reduced in an inside pipette measurement. The inside pipette measurements conclusively confirm the photothermal nature of fibers and photoelectrochemical nature of pristine sheets. This is further concurrent with argument and results observed in silicon wherein dimensionality reduction of the material enhanced

photothermal effect.[21] Thus, the dimensionality reduction in P3HT leads to photothermal characteristics in fiber form compared to sheets.

3.4. P3HT nanofiber matrices for photothermal modulation of apoptotic signaling

Primary rat cardiac fibroblasts (RCF) were photothermally stimulated to observe a rise in cytosolic calcium (Fig 3.4.a-c) followed by membrane blebbing and apoptosis (Fig.3.4.g). The rise in cytosolic calcium with photothermal stimulation suggests membrane depolarization by the well-known optocapacitance effect.[10] However, the fact that this leads to apoptosis suggests that calcium signaling turning on an apoptotic pathway. To understand this staining condition for the same calcium dye-Fluo4-AM were reoptimized for low cytosolic signals. Stimulation experiments performed under these optimized staining conditions revealed calcium loading into mitochondria and its subsequent swelling (Fig.3.4.d-f). The calcium uptake into mitochondria happens as a consequence of depolarization induced calcium flushing into the cell.[22] In order to overcome the excess calcium in cytosol the mitochondria are forced to uptake it.[22] However, the uptake of calcium into mitochondria is significantly large that it leads to an imbalance of osmotic pressure making the mitochondria swell as observed (Fig.3.4. f).[23,24] Further stimulation experiments also reveal caspase 3/7 signaling along with membrane blebbing and loss of focal adhesion confirming [25] apoptosis (Fig. 3.4. g-i). The signaling of caspase 3/7 is concurrent with the mitochondrial swelling as they rupture releasing cytochrome c leading to caspase 9 mediated type I apoptosis.[25] In order to confirm type I apoptosis, we look at caspase signaling timing as a function of power with caspase 8 and caspase 9 inhibitors.

With caspase 8 inhibitors the time dynamics as a function of power is invariant with respect to one with no inhibition suggested minimal contribution to caspase 8 pathway or type II or necrotic pathway (Fig.3.5.b). However, the signaling

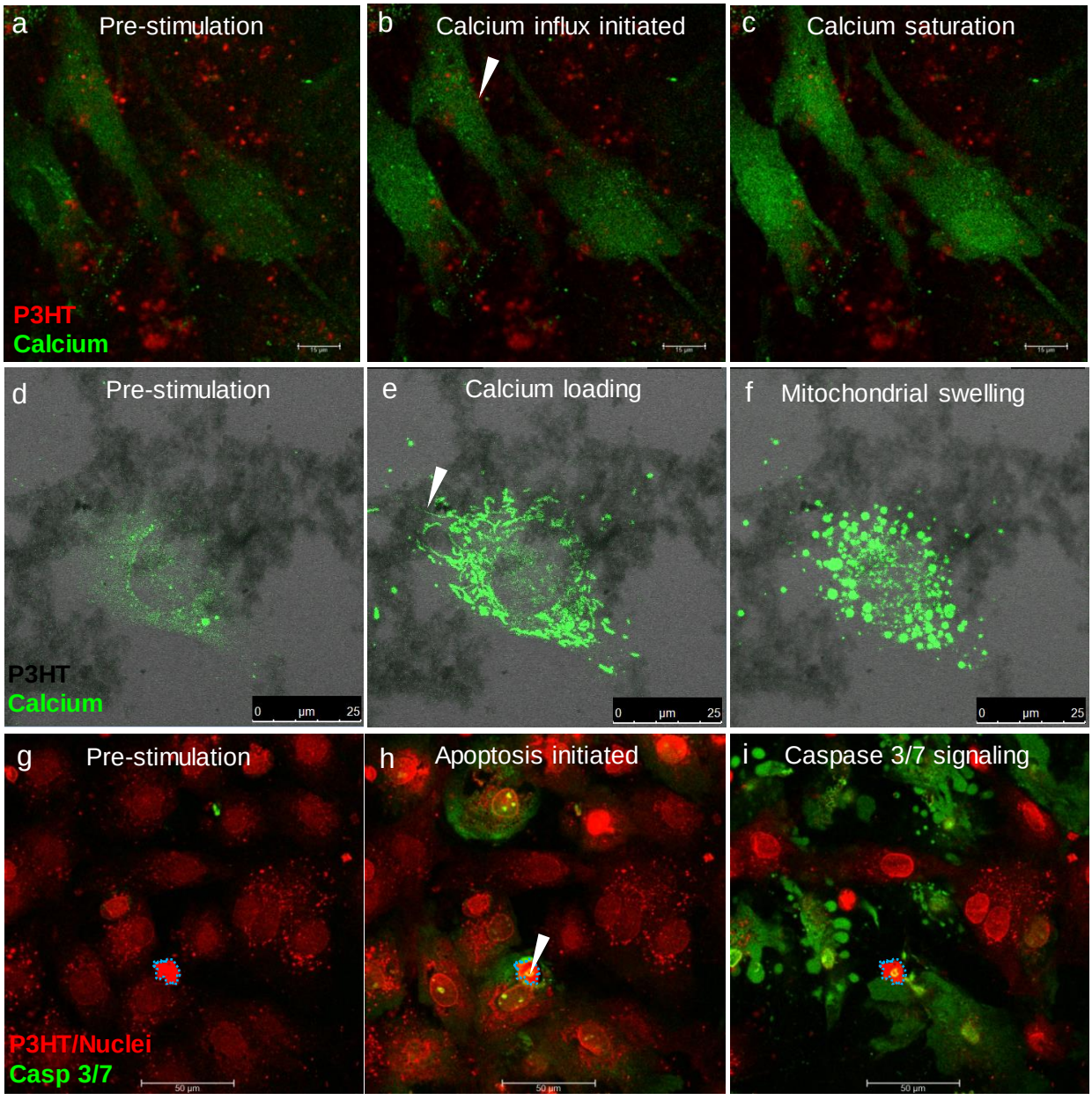

Fig. 3.4. a. Calcium levels in RCF cells before stimulation, b. Calcium levels in RCF cells immediately after stimulation showing an increase in calcium levels, c. Calcium levels saturating to a maximum possible value in RCF cells after

Fig. 3.4. continued. stimulation. d. Low level of cytosolic calcium staining in RCF cells before stimulation, e. Calcium loading into mitochondria after stimulation, f. Calcium loaded mitochondria swelling up due to excess calcium uptake. g. RCF cells stained for caspase3/7 before stimulation. P3HT fragment is covered in blue boundary here as both P3HT and cell nuclei stain fluoresce in red, they are differentiated using morphology and DIC image, h. Apoptotic signaling in caspase 3/7 is initiated after stimulation, i. Caspase 3/7 signaling is spreading across cells leading to membrane blebbing and ultimately death. The white arrow points to the stimulation point in all figures.

timing became faster and the curve shifts downward with caspase 9 inhibition (Fig.3.5.b).[26] Blocking caspase 9 pathway enables any possible apoptosis though signaling cross-talks to occur via caspase 8.[26] Caspase 8 pathways are known to be faster than caspase 9 pathway, thus inhibiting caspase 9 enables faster apoptosis.[26] This observation confirms type II pathway or mitochondria-mediated apoptosis as the dominant signaling pathway here.

Besides an understanding of the mechanism of apoptosis it's possible to realize the spatio-temporal control of apoptotic process using P3HT nanofiber matrices. Calcium and caspase 3/7 signaling onset times suggest a good control for initiation of apoptosis with stimulation power (which actually affects the temperature generated) (Fig.3.5.a). Moreover, it suggests that caspase 3/7 signaling happens much after calcium signaling concurrent with our mitochondria mediated type 2 apoptotic signaling. Besides the temporal control large area stimulation experiments suggest that apoptosis happens only to cells in regions around the stimulation point but restricted to cells on P3HT and not beyond, confirming the spatial control (Fig.3.5.c-d).

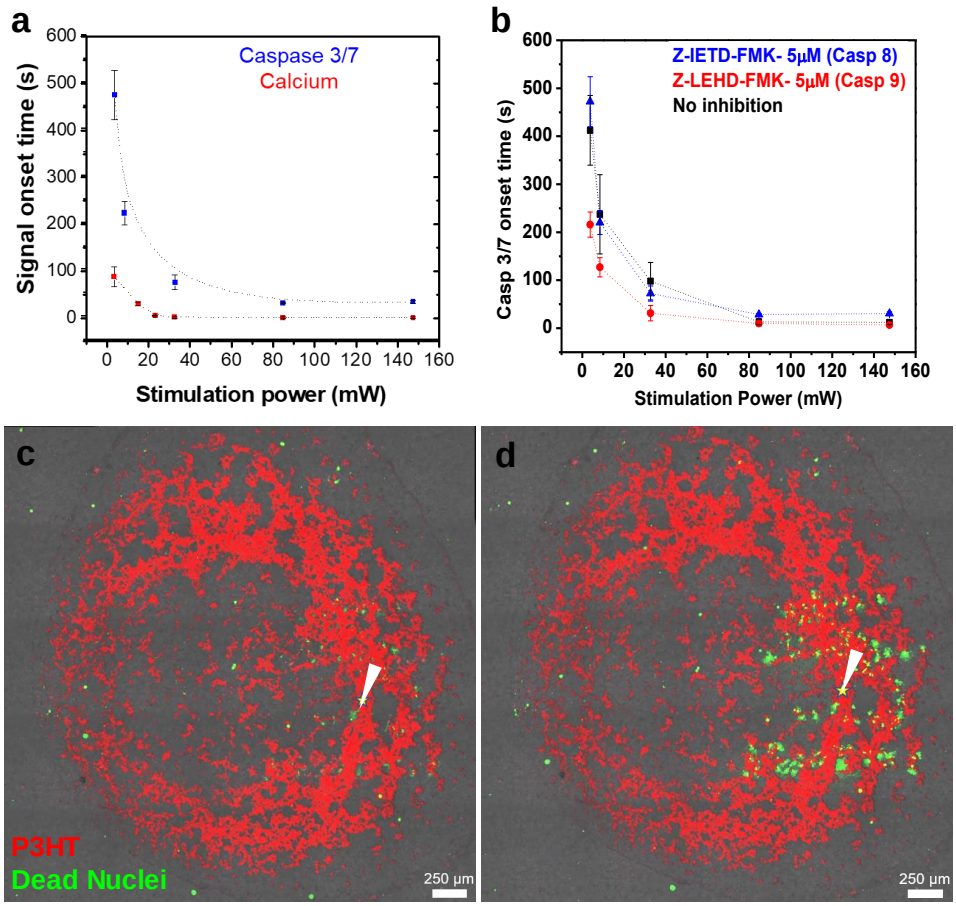

Fig.3.5. a. Caspase 3/7 and calcium signal onset times across cells in five independent stimulation experiments, b. Caspase 3/7 signaling onset time variation with caspase 8 and caspase 9 inhibitor across cells from three independent stimulation experiments, c. A large area stimulation experiment is just after stimulation, d. Large area stimulation experiment five minutes after stimulation. A white arrow indicates a stimulation point.

3.5. Role of mitochondria-lysosome interactome in apoptotic signaling

Besides the uptake of calcium by mitochondria from the cytosol, it could also receive calcium released from other organelles like lysosomes.[27-31] Mitochondria and lysosomes are known to make contact for degradative and non-degradative processes.[29] Degradative process involves mitophagy wherein a damaged mitochondrion is engulfed

by an autophagosome.[29] In comparison, non-degradative processes involve contact for transfer of metabolite and mitochondrial fission.[29] Mitochondrial fission involves RAB7-GTP hydrolysis and is observed normally in any mitochondria -lysosome network of the cell [29] and is a continuing dynamic process existing in living cells. We also observe the continuance of mitochondrial fission in cells even after stimulation until the mitochondria are stable (Fig.3.6 d-e). During the post-stimulation domain wherein in mitochondria are stable in their initial morphology we note an increase in lysosome to mitochondria contacts (Fig.3.6 b). Given our observation that calcium loading occurs into mitochondria when are they are in a stable condition, the increase in lysosome-mitochondria contacts suggests that the lysosome is transferring calcium into the mitochondria. This is a very possible pathway given that initial cytosolic calcium import into mitochondria via MCUs, activates ROS generating enzymes leading to increased ROS production in mitochondria.[27] With increased ROS the TRPM channels on lysosome get activated on contact with mitochondria releasing calcium into mitochondria.[27-31] Thus, the initial calcium import into mitochondria due to an increase in cytosolic calcium leads to more calcium being received from the lysosome eventually leading to calcium-induced mitochondrial swelling. Ultimately the lysosomes act as amplifiers of apoptotic signaling by enabling the import of more calcium into mitochondria. Further, the volume of lysosomes was found to increase after stimulation (Fig.3.6.c) suggesting the presence of physiological stress on them.30 Stresses which could lead to lysosomal swelling without rupture could be due to low pH or membrane alterations arising from ROS.[30] Either of which is valid in our problem as the ROS activity in mitochondria is activated with calcium

loading and affects lysosomes on contact.[27,30] Lysosomes don't possess any antioxidants to protect them from oxidative stresses.[30] Moreover, lysosomes are rich in iron enabling small quantities of ROS to be detrimental leading to membrane alterations and swelling.[30] Besides a loss of calcium from lysosome would push the pH to much higher values causing import of chloride and water into the lysosome leading to their swelling.[30-32] The mitochondria-lysosome interactome is thus observed to amplify calcium stress signaling for apoptosis.

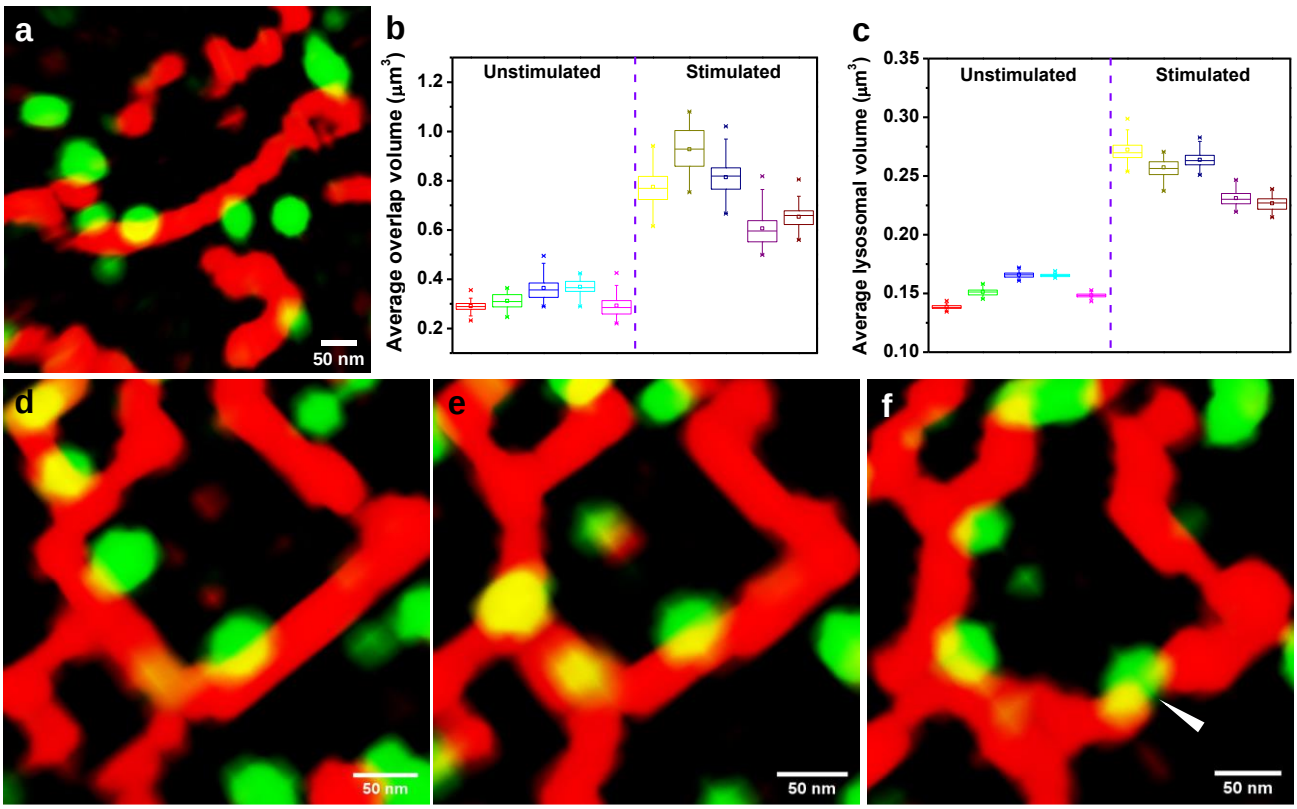

Fig.3.6. a. Representative image of lysosomes making contact with the mitochondrial network, b. Time distribution of average overlap of three-dimensional fit volumes between mitochondria and lysosomes in a cell per time frame. The box plots are time distribution of average overlap volume across a minute in five different unstimulated and stimulated cells. Averaging was done

Fig. 3.6. continued. across the number of contacts per time frame c. Time distribution of average three-dimensional fit volumes of lysosomes in a cell per time frame. The box plots are time distribution of average overlap volume across a minute in five different unstimulated and stimulated cells. Averaging was done across the number of lysosomes tracked per time frame. Lysosome marked with white arrow making contact with mitochondria tracked across a minute and 10 seconds. d- 0 sec, e- 42 secs, f-27 secs

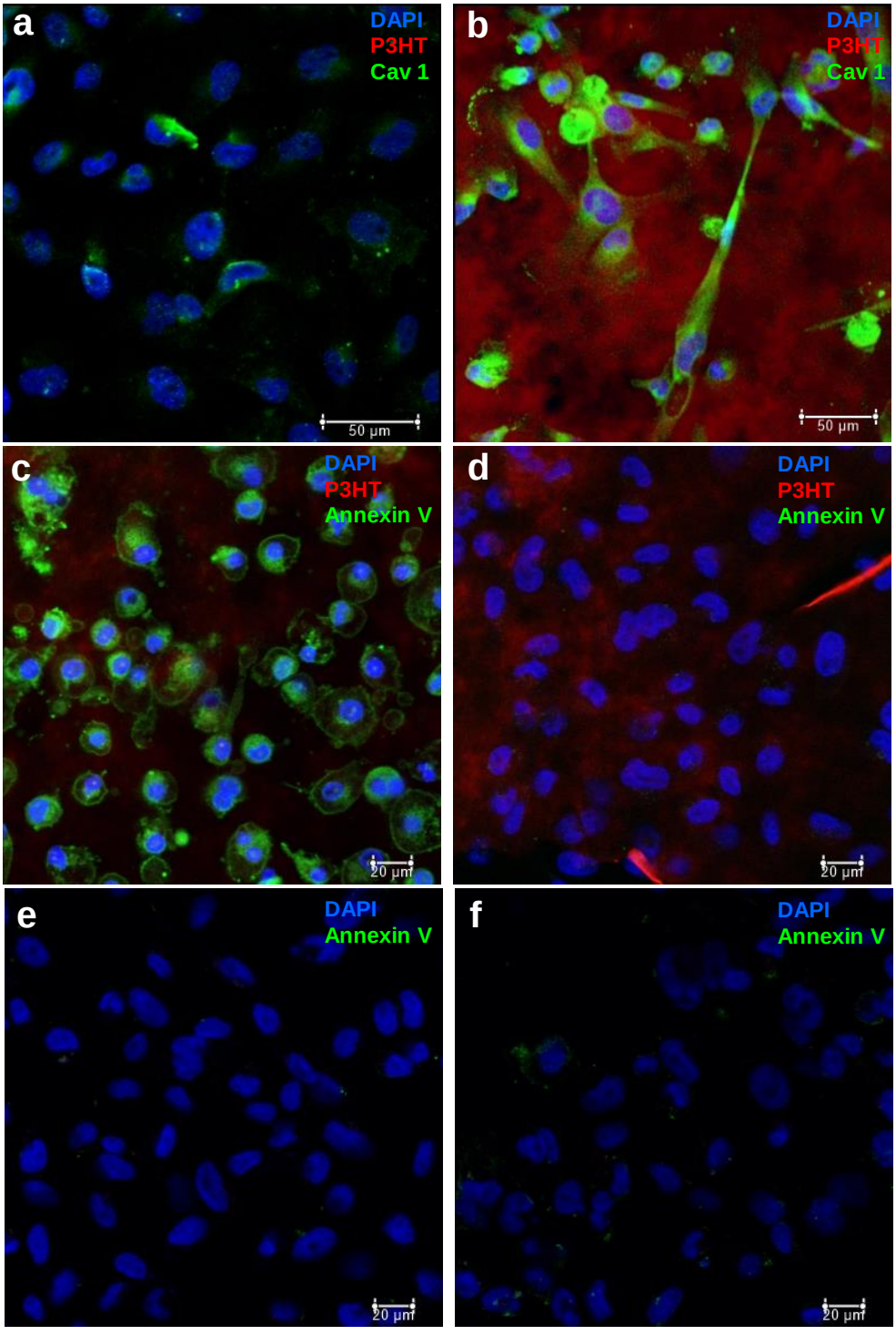

Fig.3.7. a. Caveolin 1 expression in MDA-MB-231 cells grown on the glass substrate, b. Caveolin 1 expression in MDA-MB-231 cells grown on P3HT fiber

Fig.3.7. continued. matrix, c. Annexin-V positive apoptotic MDA-MB-231 cells grown on the P3HT fiber matrix with 24-hour stimulation by 448 nm LED at 1.03 W, d. Annexin-V positive apoptotic MDA-MB-231 cells grown on the P3HT fiber matrix with no light stimulation. e. Annexin-V positive apoptotic MDA-MB-231 cells grown on glass with 24-hour stimulation by 448 nm LED at 1.03 W, d. Annexin-V positive apoptotic MDA-MB-231 cells grown on glass with no light stimulation.

3.6. P3HT nanofiber matrices for mechanotransductive apoptotic induction in triple-negative breast cancer cells

Understanding the capability of P3HT nanofiber matrices in inducing photothermal apoptosis and topographic mechanotransductive upregulation of caveolin 1 we look forward to how both these cues could be coupled in proposing a therapeutic strategy for treating cancers. Increased levels of caveolin 1 are known to possess anti-tumoral properties by causing cell-cycle arrest in specific forms of cancer.[33] Besides that, the photothermal mitochondrial calcium loading induced apoptosis being generic can be coupled synergically to form a potential cancer therapeutic strategy. Hence, we attempt this photothermal and mechanotransductive apoptosis strategy on MDA-MB-231 cells which is a triple-negative breast cancer cell line known to possess cell cycle arrest with overexpression of caveolin 1.[33]

Primarily we verify the increased expression of caveolin 1 in MDA-MB-231 cells using immunofluorescence (Fig.3.7.a-b). Further, we test the apoptotic induction in these cells by culturing them on P3HT and applying a low intensity LED simulation for 24 hours. It is observed that almost 100% of cells with P3HT and LED stimulation are apoptotic (Fig.3.7.c). The initiation of apoptosis is verified by staining for Annexin-V which are the

earliest markers of apoptosis. Control experiments with P3HT and no LED stimulation, glass and LED stimulation, glass and no LED stimulation show minimum to no apoptosis. This suggests the promising future utility of P3HT fiber matrices in cancer therapy for specific types of cancer.

3.7. Pristine P3HT sheets for photoelectrochemical modulation of neuronal networks

Having verified the capability of P3HT nanofiber as a biointerface and having tested potential utility of the same in cancer therapy, we touch upon the utility of pristine P3HT as a biointerface.

Pristine P3HT has been known to be involved in photoelectrochemical production of ROS leading to tubulogenesis in endothelial cells.[19] Thus our observation of photoelectrochemical reduction current in single-channel recordings suggests the reduction of dissolved oxygen to ROS in a physiological buffering medium. Such small scale production of ROS molecules are known to act as signaling agents.[19] We test the utility of such a system to control dorsal root ganglia neuronal network cultures.

To test the utility of pristine P3HT we pattern them into a device consisting of free-standing islands of P3HT on glass substrate atop which neurons are cultured. Scanning electron microscopy images of neurons cultured on P3HT patterns show the growth of neurites from axons to P3HT patterns are their wrapping around (Fig.3.8.a-b). This suggests a mechanical recognition of neurons of soft materials using neurite outgrowth.[34] Such neurite outgrowths to islands suggest the future utility of using such neurite interfacing

with P3HT islands for controlling links in a neuronal network. Such a strategy extends beyond the understanding of conventional synchronization modulation and is complex but is useful from a modulation perspective as we offer additional cues for interfacing. Besides this the islands could also interface will the cell soma which is the nodes of our network enabling their direct photoelectrochemical modulation (Fig. 3.8.f-g)

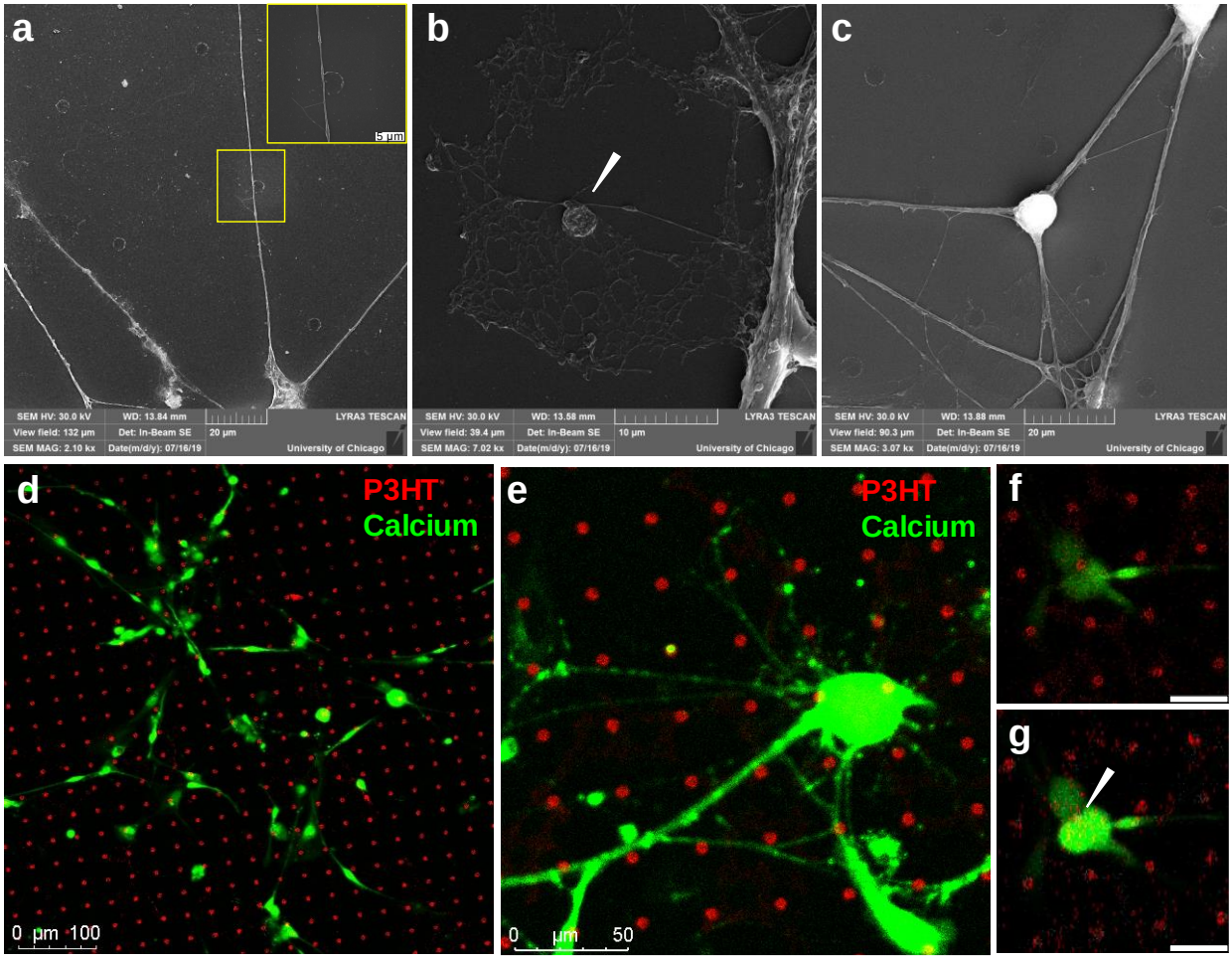

Fig.3.8. a. Scanning electron microscopy (SEM) image showing an axon interfacing with a P3HT island (yellow box) with a neurite outgrowth onto the island, b. Neurite outgrowth from an axon to surround a P3HT island nearby, c. Representative SEM image of a neural network on P3HT patterned glass substrate, d. Confocal fluorescence image of a neuronal network on a P3HT device, e. A

Fig. 3.8. continued. neuron showing outgrowth of neurite in all directions terminating on P3HT islands around it. f. A neuronal soma interfacing with a P3HT island before its photoelectrochemical stimulation, g. A neuronal soma interfacing with a P3HT island after its photoelectrochemical stimulation showing calcium influx and depolarization.

3.8. Conclusion

Through this project, a nanofiber mesh-like matrix that mimics the extracellular matrix in morphology and elasticity has been developed. This matrix also possesses the photothermal capability and topographical features for additional modes of mechanotransduction through caveolin 1 signaling. Using heat impulses study apoptotic signaling was studied and the mechanism confirmed. This was achieved by a systematic study of calcium signaling in mitochondria, caspase 3/7 signaling and their time dynamics along with the role of the mitochondria-lysosome interactome. Besides we demonstrate a synergic strategy of coupling of caveolin 1 mechanotransduction with photothermal stimulation for apoptotic induction in triple-negative breast cancer cells. As a control biointerface to P3HT nanofibers, we demonstrate the photoelectrochemical capability of pure pristine P3HT for neuronal modulation and how microfabricated devices interact with a neuronal network.

3.9. Experimental Methods

Synthesis of P3HT nanofibers and sheets:

0.2 mg of RR-P3HT (Sigma Aldrich) is mixed with 5 mL of cyclohexanone (Sigma Aldrich) and nitrogen gas bubbled through the solvent for an hour before raising the temperature

to 120 C under vacuum conditions. Once at 120 C for an hour slowly ramp down to room temperature with 20C every hour under vacuum and keep at room temperature overnight. All reactions to be done under dark or limited lighting.

For P3HT sheets 0.2 mg of RR-P3HT (Sigma Aldrich) is dissolved in 10 mL of chloroform (Sigma Aldrich) and spin casted at 1000 rpm for 1 min or drop cast enough to cover the surface and air dry.

Electron Microscopy

Transmission electron microscopy and High angle annular dark field -scanning transmission electron microscope (HAADF-STEM) were done on an FE Technai twin F30 scope with an accelerating voltage of 300 kV. Cryo electron microscopy was done FEI Talos with an accelerating voltage of 200 kV. Scanning electron microscopy was done on Tescan Lyra 2.

Biological specimens were prepared for SEM using the following protocol. Cells were fixed overnight at 4 C in 2.5% Glutaraldehyde in PBS. Followed by ethanol washes for ten minute each in increasing concentration of ethanol. The samples critical point dried in Leica EM CPD 300. Following critical point drying the samples were sputter coated with 5 nm gold before imaging in SEM.

Atomic force microscopy

Atomic force microscopy was performed under tapping mode with scan-asyst feature on Bruker dimension icon AFM.

Compression modulus measurement

Compression modulus measurement was done on TA Instruments RSA-G2 Dynamic Mechanical Analyzer using 5 mm diameter compression plates. The measurements were done under a constant compression force of 0.1 N with strain varying from 0.1% to 1%. Measurements were done across a temperature range of 25 C to 55 C in a temperature controlled chamber encasing the measurement sample and compression plates.

Photocurrent measurements

Photocurrent measurements were performed by single channel voltage clamped recordings on a patch-clamp amplifier (Axopatch 200B) set up. The material of interest was immersed in 1X PBS (Fisher Scientific) in a petridish and focused on using a microscope (Olympus BX61WI) with a water immersion lens (20X/0.5 NA). Light pulses are delivered through the microscope using a 532 nm laser (Laser glow, diode -pumped solids state laser, ~5 μm spot size). Light pulses were delivered to these light sources using a digitizer (Molecular devices, Digidata 1550). For measuring the photocurrent measurements glass pipettes (OD: 1.5 mm, ID: 1.10 mm, Length: 10 cm, Sutter instruments Cat No: BF150-110-10) of ~ 1 MΩ were pulled (Sutter Instrument, P-97) and their tip lowered and focused onto the same optical plane (Gap of ~2 μm) as the material surface before the stimulation pulse is applied. The voltage clamped currents were

recorded with a bias of -0.5V in parallel with the stimulation pulse at various holding current levels. This data was analyzed and the nature of the photocurrents determined using a previously developed method.[21] For analysis of photothermal currents the same pipette used for recording was calibrated for its resistance as a function of temperature. For this measurement the pipette was dipped in pre-heated PBS at approximately 50-60°C and allowed to cool down naturally as the resistance were recorded alongside temperature, using a thermocouple.

For inside pipette measurements the samples were taken into an unblown pipette and dried keeping the liquid drawn in at the center of the capillary tube. Once dried properly the pipettes were blown with a resistance in the range of 15-20 MΩ. This is to prevent any leaky currents from escaping the electrode. Measurements were performed by focusing the laser onto sample far away from the pipette but away from the Ag/AgCl electrode. The voltage clamped currents were recorded with a bias of 0 V in parallel with the stimulation pulse at various holding current levels.

Cell culture

Rat cardiac fibroblasts: P0-P5 neonatal rat hearts were isolated and placed into ice cold hanks balanced salt solution without calcium or magnesium (HBSS). Further these hearts were digested and fibroblasts obtained from them using Pierce cardiomyocyte culture kit (Thermo Fisher) by following manufacturers protocol. The cell suspension containing cardiomyocyte and fibroblasts were seeded in tissue culture plates for an hour to allow adherence of fibroblasts keeping the cardiomyocytes in the supernatant. The supernatant

is removed and replaced with rat cardiac fibroblast media consisting of DMEM with 5% FBS, 1% Pen-Step and 1% Glutamax (Life technologies).

Dorsal root ganglias were harvested from P0-P3 Sprague-Dawley rat pups into ice cold DMEM/F12 (Thermo Fisher 11320033). The ganglias were then digested in 2.5 mg/mL trypsin (Worthington TRL3) in EBSS with no Ca/Mg (Thermo Fisher 14155063) for exactly 20 minutes in a 37°C shaker incubator. The ganglias were then centrifuged at 1500 rpm for 2 min and separated from trypsin and resuspended in EBSS with 10% FBS. The ganglias are mechanically triturated using fire polished pasteur pipettes of decreasing sizes and centrifuged down at 1500 rpm for 2 min. After removing the supernatant the cells were resuspended in complete media (DMEM/F12 with 1% pen-strep, 5 % FBS along with 20 μM 5-fluoro uracil (Sigma Aldrich) and 50 ng/mL of NGF 2.5S (Thermo Fisher) . The glass bottom dishes for seeding are covered with 0.01% poly-L -lysine in molecular biology grade water for 20 min, washed with water and aspirated dry with vacuum. The cells are seeded on this dish according to required concentration.

MDA-MB-231 cells were obtained from the university of chicago cell screening facility and cultured in DMEM with 10% FBS and 1% Pen-Strep.

Cellular stimulation experiments

Point stimulation experiments were carried out in the FRAP mode of a LEICA SP5 STED-CW confocal microscope with a 592 nm laser. For cells, stimulation was done for 1 ms and at varying powers. For LED stimulation experiments to test apoptotic induction in cells, a 6 x 4 configuration of 447.5 nm LEDs each of power 1.03 W were placed onto a

heat sink board to suit a 24 well plate configuration. The were driven using a voltage of 2.5 V and pulsed at 1 Hz at full power for 24 hours.

Live imaging staining

Cytosolic calcium imaging was done using Fluo4-AM (Invitrogen) which was made into a 50 µM stock solution in Pluronic F-127 which is in 20% DMSO (Invitrogen). Cell were incubated with 2 µM Fluo4-AM in media for 30 minutes and washed post-incubation with media. The cells were further incubated for 15 minutes in media before beginning imaging. For mitochondrial calcium imaging using Fluo4-AM (Invitrogen) which was made into a 50 µM stock solution in DMSO (Invitrogen). Cell were incubated with 2 µM Fluo4-AM in media for 15 minutes and washed post-incubation with media and taken for imaging and stimulated. However, the staining time versus concentration may need to be optimized for different batches of cells or cell types. Caspase 3/7 staining for live imaging was done using CellEvent Caspase-3/7 Green ReadyProbes Reagent (Thermo Fisher). Staining was done by using 2 drops of the reagent per mL of media and incubated for 30-45 mind before imaging and stimulation. Mitochondria and Lysosome staining was done using MitoView 405 (Biotium) and LysoView 488 (Biotium) and staining performed as per manufacturers protocol for live imaging.

Immunofluorescence staining

The cell cultures were fixed with 4% paraformaldehyde in PBS for 10 minutes and then washed in PBS thrice. Following this they were permeabilized with 0.5% Triton X-100 for 10 minutes and washed in PBS thrice. After the cells are fixed and permeabilized they

were incubated in a blocking solution of 3% BSA in PBS for 60 minutes following which 2 drops/mL of ActinGreen 488 ReadyProbes (Invitrogen) was added to the blocking solution. The solution was incubated for another 30 minutes with the actin stain before washing and imaging in PBS. For vinculin staining, vinculin monoclonal antibody (7F9) conjugated with Alexa Fluor 488 (eBioscience) was stained at a concentration of 20 µg/mL overnight at 4C, after fixation and permeabilization. Caveolin 1 staining was done using Anti-Caveolin-1 conjugated with Alexa Fluor 488, Clone: 7C8 (Novus biologicals) at a concentration of 20 µg/mL overnight at 4C, after fixation and permeabilization. Annexin V-FITC conjugates were stained using Life Technologies ApoDETECT staining kit and as per manufacturers instruction. Nuclear staining was done using NucBlue Live ReadyProbes (Thermo Fisher) or NucRed Live 647 ReadyProbes (Thermofisher) as per manufacturers protocol.

Three -dimensional fluorescence microscopy data analysis

Three -dimensional sections of greater than a micron thickness was collected to analyze mitochondria -lysosome interaction in single cells. Imaging and stimulation was done on a LEICA SP8 with stimulation of 1 ms and 10 mW power using a 592 nm laser. Collected data were then analyzed using Arivis Vision4D software package. Data were passed through a particle enhancement filter and bleach corrected. Following which spheres were fit to reconstruct mitochondria and lysosomal structures. All reconstructed structures were tracked using Brownian centroid motion algorithm and along with overlapping volumes of mitochondria and lysosome detected using compartmentalization module of the software.

References

1. Hussey, G. S.; Dziki, J. L.; Badylak, S. F. Extracellular Matrix-Based Materials for Regenerative Medicine. Nature Reviews Materials 2018, 3 (7), 159–173.

2. Pennacchio, F. A.; Caliendo, F.; Iaccarino, G.; Langella, A.; Siciliano, V.; Santoro, F. Three-Dimensionally Patterned Scaffolds Modulate the Biointerface at the Nanoscale. Nano Lett. 2019, 19 (8), 5118–5123.

3. Bavi, N.; Nikolaev, Y. A.; Bavi, O.; Ridone, P.; Martinac, A. D.; Nakayama, Y.; Cox, C. D.; Martinac, B. Principles of Mechanosensing at the Membrane Interface. In The Biophysics of Cell Membranes; Epand, R. M., Ruysschaert, J.-M., Eds.; Springer Singapore: Singapore, 2017; Vol. 19, pp 85–119.

4. Akhmanova, M.; Osidak, E.; Domogatsky, S.; Rodin, S.; Domogatskaya, A. Physical, Spatial, and Molecular Aspects of Extracellular Matrix of In Vivo Niches and Artificial Scaffolds Relevant to Stem Cells Research. Stem Cells Int 2015, 2015.

5. Son, S. Y.; Kim, J.-H.; Song, E.; Choi, K.; Lee, J.; Cho, K.; Kim, T.-S.; Park, T. Exploiting π–π Stacking for Stretchable Semiconducting Polymers. Macromolecules 2018, 51 (7), 2572–2579.

6. Nair, V.; Kumar, A.; Subramaniam, C. Exceptional Photoconductivity of Poly(3-Hexylthiophene) Fibers through in Situ Encapsulation of Molybdenum Disulfide Quantum Dots. Nanoscale 2018, 10 (22), 10395–10402.

7. Kleinhenz, N.; Persson, N.; Xue, Z.; Chu, P. H.; Wang, G.; Yuan, Z.; McBride, M. A.; Choi, D.; Grover, M. A.; Reichmanis, E. Ordering of Poly(3-Hexylthiophene) in Solutions and Films: Effects of Fiber Length and Grain Boundaries on Anisotropy and Mobility. Chem. Mater. 2016, 28 (11), 3905–3913.

8. Hintz, H.; Egelhaaf, H.-J.; Lüer, L.; Hauch, J.; Peisert, H.; Chassé, T. Photodegradation of P3HT−A Systematic Study of Environmental Factors. Chem. Mater. 2011, 23 (2), 145–154.

9. Kucsko, G.; Maurer, P. C.; Yao, N. Y.; Kubo, M.; Noh, H. J.; Lo, P. K.; Park, H.; Lukin, M. D. Nanometre-Scale Thermometry in a Living Cell. Nature 2013, 500 (7460), 54–58.

10. Carvalho-de-Souza, J. L.; Pinto, B. I.; Pepperberg, D. R.; Bezanilla, F. Optocapacitive Generation of Action Potentials by Microsecond Laser Pulses of Nanojoule Energy. Biophysical Journal 2018, 114 (2), 283–288. https://doi.org/10.1016/j.bpj.2017.11.018.

11. Williams, J. A. Origin of Transmembrane Potentials in Non-Excitable Cells. Journal of Theoretical Biology 1970, 28 (2), 287–296.

12. Jiang, Y.; Carvalho-de-Souza, J. L.; Wong, R. C. S.; Luo, Z.; Isheim, D.; Zuo, X.; Nicholls, A. W.; Jung, I. W.; Yue, J.; Liu, D.-J.; et al. Heterogeneous Silicon Mesostructures for Lipid-Supported Bioelectric Interfaces. Nature Mater 2016, 15 (9), 1023–1030.

13. Chantre, C. O.; Campbell, P. H.; Golecki, H. M.; Buganza, A. T.; Capulli, A. K.; Deravi, L. F.; Dauth, S.; Sheehy, S. P.; Paten, J. A.; Gledhill, K.; et al. Production-Scale

Fibronectin Nanofibers Promote Wound Closure and Tissue Repair in a Dermal Mouse Model. Biomaterials 2018, 166, 96–108.

14. Tojkander, S.; Gateva, G.; Lappalainen, P. Actin Stress Fibers - Assembly, Dynamics and Biological Roles. Journal of Cell Science 2012, 125 (8), 1855–1864.

15. Zhou, D. W.; Lee, T. T.; Weng, S.; Fu, J.; García, A. J. Effects of Substrate Stiffness and Actomyosin Contractility on Coupling between Force Transmission and Vinculin–Paxillin Recruitment at Single Focal Adhesions. Mol Biol Cell 2017, 28 (14), 1901–1911.

16. Sun, Z.; Guo, S. S.; Fässler, R. Integrin-Mediated Mechanotransduction. J Cell Biol 2016, 215 (4), 445–456.

17. Wenger, M. P. E.; Bozec, L.; Horton, M. A.; Mesquida, P. Mechanical Properties of Collagen Fibrils. Biophys J 2007, 93 (4), 1255–1263..

18. Klotzsch, E.; Smith, M. L.; Kubow, K. E.; Muntwyler, S.; Little, W. C.; Beyeler, F.; Gourdon, D.; Nelson, B. J.; Vogel, V. Fibronectin Forms the Most Extensible Biological Fibers Displaying Switchable Force-Exposed Cryptic Binding Sites. Proceedings of the National Academy of Sciences 2009, 106 (43), 18267–18272.

19. Lodola, F.; Rosti, V.; Tullii, G.; Desii, A.; Tapella, L.; Catarsi, P.; Lim, D.; Moccia, F.; Antognazza, M. R. Conjugated Polymers Optically Regulate the Fate of Endothelial Colony-Forming Cells. Sci. Adv. 2019, 5 (9), eaav4620.

20. Parameswaran, R.; Carvalho-de-Souza, J. L.; Jiang, Y.; Burke, M. J.; Zimmerman, J. F.; Koehler, K.; Phillips, A. W.; Yi, J.; Adams, E. J.; Bezanilla, F.; et al.

Photoelectrochemical Modulation of Neuronal Activity with Free-Standing Coaxial Silicon Nanowires. Nature Nanotech 2018, 13 (3), 260–266.

21. Jiang, Y.; Li, X.; Liu, B.; Yi, J.; Fang, Y.; Shi, F.; Gao, X.; Sudzilovsky, E.; Parameswaran, R.; Koehler, K.; et al. Rational Design of Silicon Structures for Optically Controlled Multiscale Biointerfaces. Nat Biomed Eng 2018, 2 (7), 508–521.

22. Raffaello, A.; Mammucari, C.; Gherardi, G.; Rizzuto, R. Calcium at the Center of Cell Signaling: Interplay between Endoplasmic Reticulum, Mitochondria and Lysosomes. Trends Biochem Sci 2016, 41 (12), 1035–1049.

23. Webster, K. A. Mitochondrial Membrane Permeabilization and Cell Death during Myocardial Infarction: Roles of Calcium and Reactive Oxygen Species. Future Cardiol 2012, 8 (6), 863–884.

24. Gao, W., Pu, Y., Luo, K.Q., Chang, D.C. Temporal relationship between cytochrome c release and mitochondrial swelling during UV-induced apoptosis in living HeLa cells. Journal of Cell Science 2001, 114(15), 2855-2862.

25. Taylor, R. C.; Cullen, S. P.; Martin, S. J. Apoptosis: Controlled Demolition at the Cellular Level. Nat Rev Mol Cell Biol 2008, 9 (3), 231–241.

26. Raychaudhuri, S.; Willgohs, E.; Nguyen, T.-N.; Khan, E. M.; Goldkorn, T. Monte Carlo Simulation of Cell Death Signaling Predicts Large Cell-to-Cell Stochastic Fluctuations through the Type 2 Pathway of Apoptosis. Biophys J 2008, 95 (8), 3559–3562.

27. Todkar, K.; Ilamathi, H. S.; Germain, M. Mitochondria and Lysosomes: Discovering Bonds. Front Cell Dev Biol 2017, 5.

28. Raffaello, A.; Mammucari, C.; Gherardi, G.; Rizzuto, R. Calcium at the Center of Cell Signaling: Interplay between Endoplasmic Reticulum, Mitochondria and Lysosomes. Trends Biochem Sci 2016, 41 (12), 1035–1049.

29. Wong, Y. C.; Kim, S.; Peng, W.; Krainc, D. Regulation and Function of Mitochondria–Lysosome Membrane Contact Sites in Cellular Homeostasis. Trends in Cell Biology 2019, 29 (6), 500–513.

30. Wang, F.; Gómez-Sintes, R.; Boya, P. Lysosomal Membrane Permeabilization and Cell Death. Traffic 2018, 19 (12), 918–931.

31. Kroemer, G.; Jäättelä, M. Lysosomes and Autophagy in Cell Death Control. Nat Rev Cancer 2005, 5 (11), 886–897.

32. Narayanaswamy, N.; Chakraborty, K.; Saminathan, A.; Zeichner, E.; Leung, K.; Devany, J.; Krishnan, Y. A PH-Correctable, DNA-Based Fluorescent Reporter for Organellar Calcium. Nat Methods 2019, 16 (1), 95–102.

33. Qian, X.-L.; Pan, Y.-H.; Huang, Q.-Y.; Shi, Y.-B.; Huang, Q.-Y.; Hu, Z.-Z.; Xiong, L.-X. Caveolin-1: A Multifaceted Driver of Breast Cancer Progression and Its Application in Clinical Treatment. Onco Targets Ther 2019, 12, 1539–1552.

34. Schmidt, C. E.; Shastri, V. R.; Vacanti, J. P.; Langer, R. Stimulation of Neurite Outgrowth Using an Electrically Conducting Polymer. Proceedings of the National Academy of Sciences 1997, 94 (17), 8948–8953.

4. Design of coaxial hybrid silicon nanowire biointerfaces for nanoscale cellular mechanosensing

4.1. Introduction

Rigidity sensing by cells has been an important biophysical problem to understand cell migration, filopodial outgrowth, wound healing and cancer metastasis.[1-3] A conventional elastic modulus measurement involves the application of a force at one point and sensing the transmitted force at the other point. However, cells do not have a piece of machinery that enables them to perform a two-point measurement simultaneously like an instrument.[3] Cells rely entirely on one-point measurements made using their focal adhesions in a stochastic self-consistent way to sense the rigidity.[3-5] This involves the statistical coupling of Brownian forces in the focal adhesion sensor protein and that of the substrate.[3-5] The use of nanostructured materials as a tool to study rigidity sensing could be a useful strategy to obtain a biophysical understanding of this problem.

Silicon nanowires have been shown to form extra and intracellular interfaces with cells for photoelectrochemical stimulation, cellular uptake and transport respectively.[6-8] The uptake and dynamics of silicon nanowire have been studied and the mechanism proposed to be phagocytosis.[8-9] This past study primarily focuses on highly confluent cell cultures making contact with nanowires using their lamella to initiate phagocytosis.[8-9] However, cells are also capable of sensing their environment using stochastically growing filopodia.[10-11] Hence it is of interest to understand how filopodial sensing and subsequent transport of silicon nanowire may occur, along with their ultimate fate. Furthermore, it is

necessary to elucidate the biophysical principle governing the sensing of a distant nanowire from the cell. The role of Brownian forces and their transmission from nanomaterials to cells is one potential cue for filopodial growth and sensing.[10-11] Generally, we expect such forces to be transmitted via extracellular matrices and sensed by cells.[12] This would also enable verification of a theoretically proposed stochastic self-consistent way by which cells sense rigidity.

This work explores explore filopodial recognition of nanowire and their transport to cells followed by their phagocytosis. We reveal how lamellar dynamics permit the translation of nanowires along filopodia or cell lamella. Further to verify the Brownian force sensing by cells we design a structurally integrated artificial coaxial hard-soft material using silicon nanowire and poly-(3- hexyl thiophene) (P3HT) or graphene. These choices of material are available from the solution phase synthetic strategies adopted to involve materials of distinctly different elastic modulus from forming a coaxial interface. Though the silicon nanowire -graphene composite is structurally unstable for the study, the Si-P3HT matrix enables the nanowire to be encapsulated in its framework to test the ability of a cell to seek it. Testing the ability of a cell to seek a hard nanoscale material buried in a soft framework enables us to understand that the cells can sense Brownian forces from the nanowire arising from differential local stiffness in a matrix. This confirms the nanoscale mechanosensing capability of a cell for diffuse Brownian forces.

4.2. Filopodial transport of nanowire by lamellar dynamics

Rat cardiac fibroblasts (RCF) cultured with 50% confluency seeded with nanowires allowed for observing any filopodial growth and interaction with nanowires away from the cellular lamella. It was observed across cells that filopodial outgrowth and attachment to nanowires occurred at multiple spots across the same cell (Fig.4.1. a. Furthermore, live imaging and observation of the cells allowed for one to observe nanowire transport across filopodia (Fig.4.1.b.c and 4.1.d.e). These nanowires were essentially observed to glide along the membrane of the filopodia at a very slow pace. However, the velocity of transport is known to be a variable in filopodial transport as it's known to be load-dependent.[13]

Besides a single cell having multiple filopodia accessing wires across the cells neighboring environment a single filopodium could potentially tether onto multiple nanowires and transport them sequentially into a target vesicle or phagosome. It is observed the transport happens linearly along the lamella of filopodia. To understand how this transport is achieved a careful observation is made on the transport of nanowire along a lamella. Observing a nanowire that is initially attached along a lamella we observe two projections along either end of the nanowire (Fig.4.2.a). With time the lamellar projection holding the nanowire in the direction of motion retracts (Fig.4.2.b-e) and the projection away from the direction of motion expands and pushes the nanowire forward in the direction of motion (Fig.4.3.f-k). Ultimately, we can observe a translation along the lamella for the nanowire with respect to its initial position (Fig.4.3. l). This observed mechanism

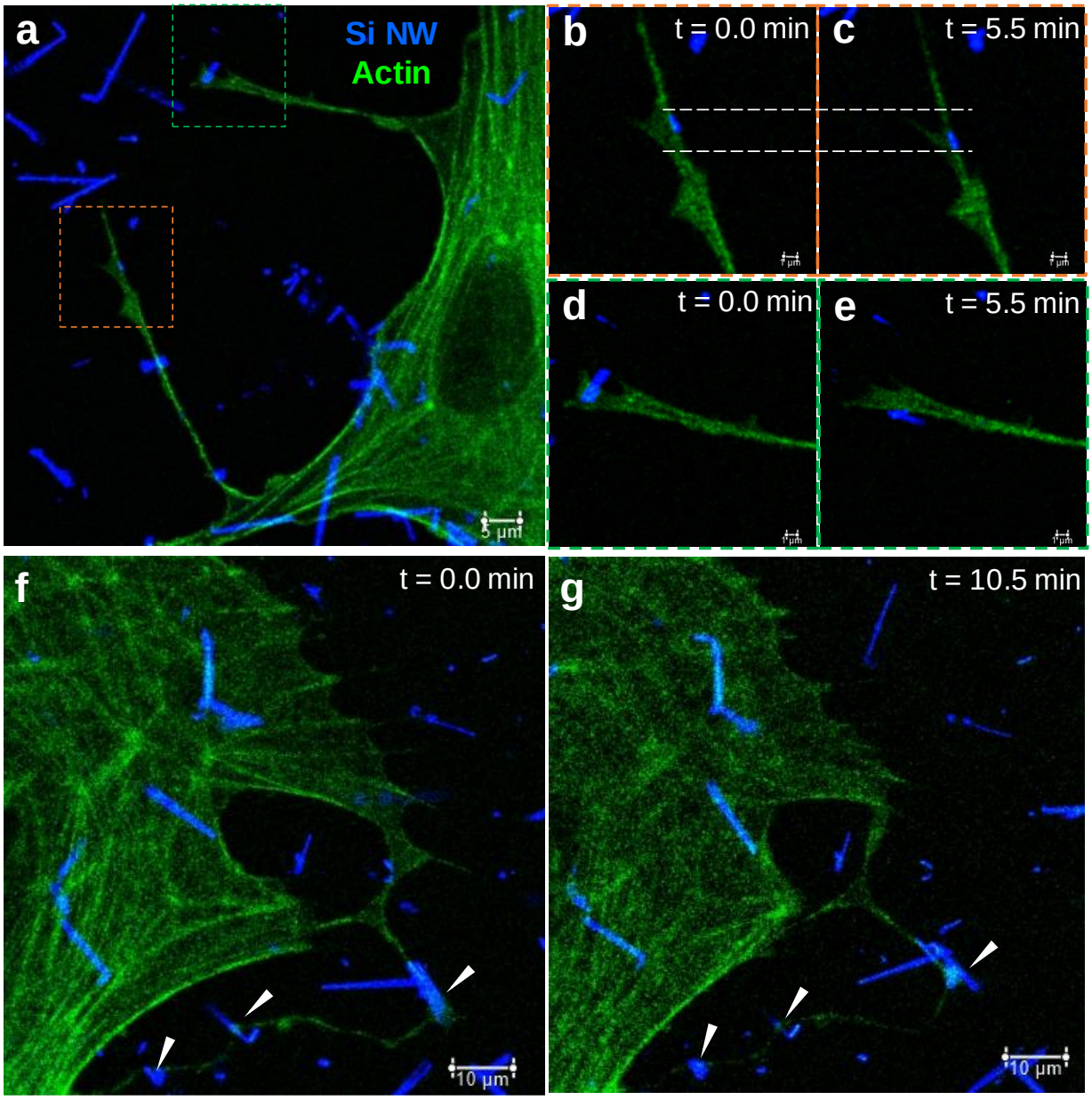

Fig.4.1. a. RCF cells with multiple filopodia attaching to nanowires across the region and transporting them to a cell. Nanowire transported along filopodia at a spot with an orange box in (a), recorded at 0 min – b and 5.5 min -c. Nanowire transported along filopodia at a spot with a green box in (a), recorded at 0 min – b and at 5.5 min -c. Single filopodia tethering to multiple nanowires and sliding them along the filopodia towards a target phagosome or vesicle observed from 0.0 min – f till 10.5 min -g.

of transport on the lamella of a cell could be well extrapolated to the lamella of a filopodia involved in transporting the nanowire. This is as the filopodia themselves like lamella are made of actin with the same fundamental dynamic instability potentially allowing this transport.[14] Once the filopodia transport the nanowire towards the cell membrane using lamellar motion, the filopodia exerts itself onto the nanowire and pushes it onto the plasma membrane (Fig.4.3.a) to initiates phagocytosis (Fig 4.3.b) and the nanowires are transported in these phagosomes towards the nuclear periphery (Fig. 4.3. c-d). However, the cargo sorting mechanism and criterion of nanowires are largely unknown. Through these investigations we gain insight into the fact that filopodial transport happens into the nanowire using a sequential lamellar motion where it ultimately

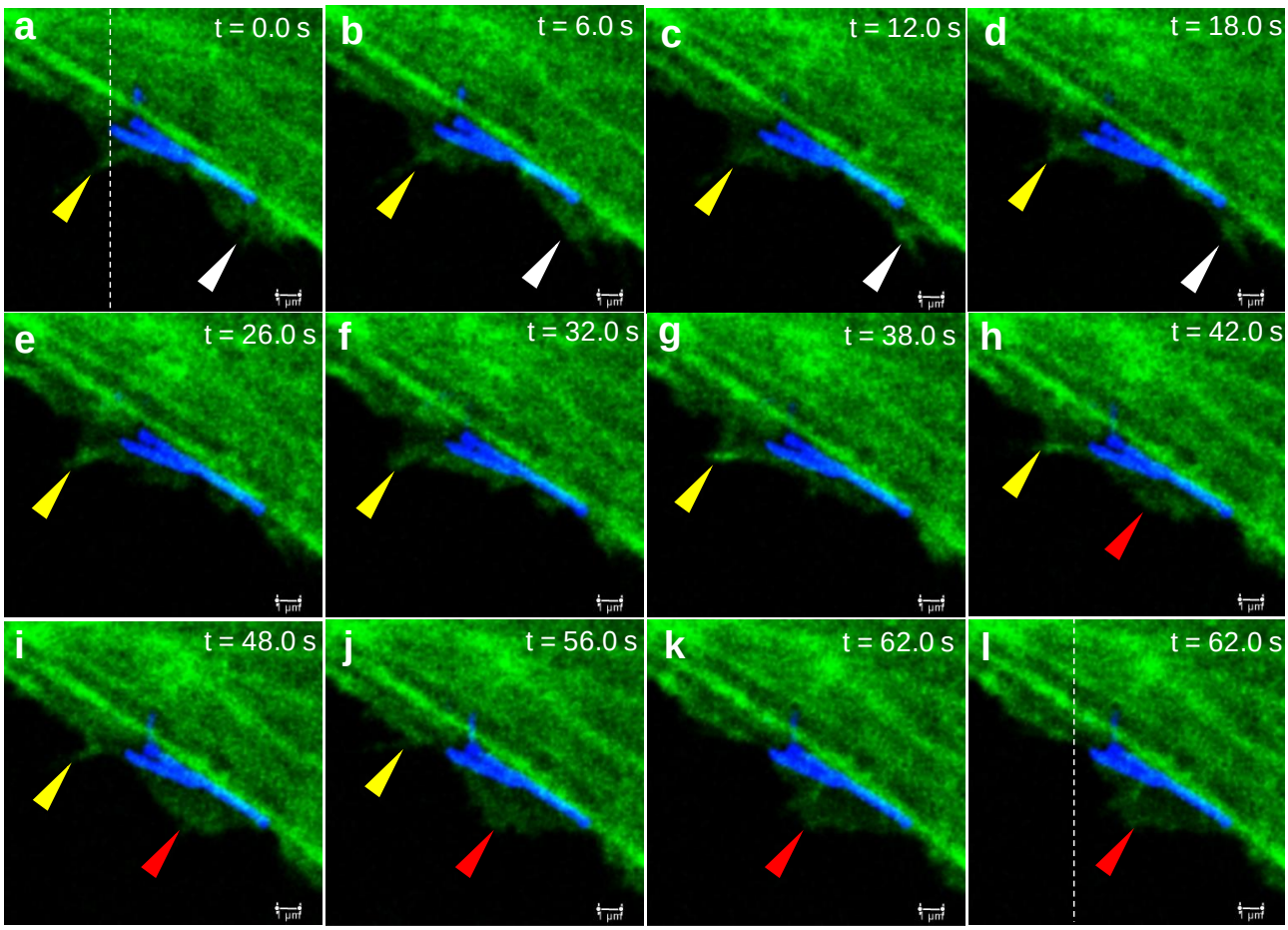

Fig.4.2. a. Initial configuration of a nanowire before translation starts along the lamella where the white dashed line marks the rear end (Yellow arrow) of the nanowire away from the direction of motion. b-e. We observe the retraction of the lamellar projection away from the forward end (White arrow) and the projection in the lamella at the rear end expands (Red arrow) (f-k) in the direction of motion. This ultimately causes the nanowire to translate along the lamella from its initial starting point. (l)

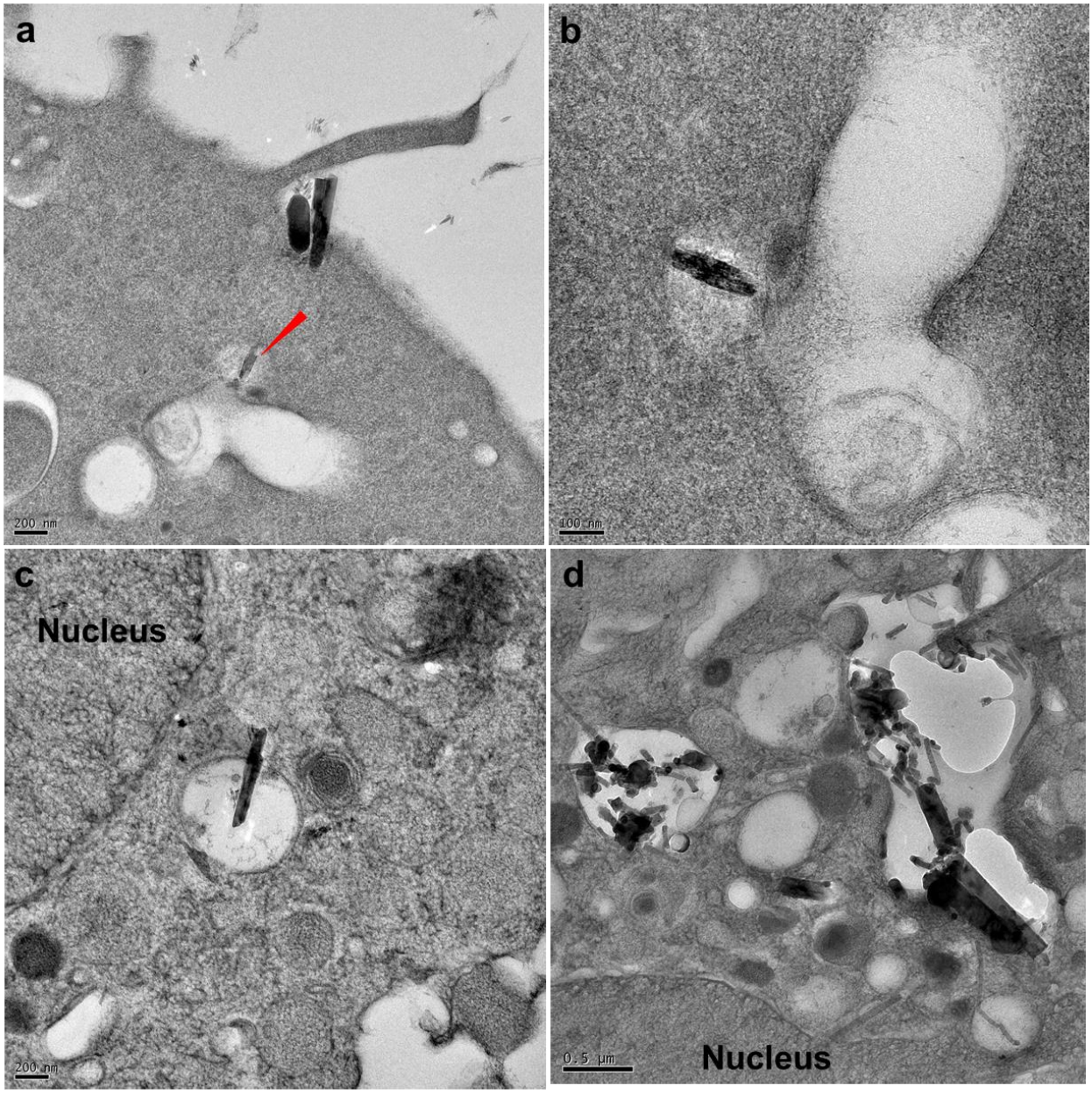

Fig.4.3. a. Electron microscopy reveals that post the filopodial transport of nanowire close to the cell membrane the filopodia pushes the nanowire towards the cell membrane to initiate phagocytosis. The red arrow shows a nanowire in a phagosome merging with another phagosome or endosome or lysosome. b. Enlarged view of the nanowire in phagosome marked with a red arrow in (a). c. Phagosome transporting nanowire close to the nucleus. d. Accumulation of most uptaken nanowire near the nucleus.

phagocytoses the wire. This type of a sequential lamellar motion for transportation is more observed in nanowire compared to nano-spherical particles. Spherical particles are transported by sequential retraction of the filopodia or lever arm retraction of the filopodia.[13] This difference in transport methodology can be attributed to the linear or quasi cylindrical geometry of the nanowire. A quasi-cylindrical geometry which enables nanowires to make a larger contact area with the cell membrane than a sphere initiating a much stronger mechanosensing capability towards nanowires. These investigations tell us the capability of cells to sense, transport and phagocytose nanowire but what is intriguing would be understand the biophysical mechanism of this process.

4.3. Need for coaxially grown hybrids- synthesis and properties

It has been so far assumed that Brownian forces enable rigidity sensing along with the extracellular matrix of a cell.[3] If this hypothesis is true cells should be capable of sensing hard substrates with nanoscale precision in artificial ECM like soft matrices or soft substrates in a harder matrix. To test our hypothesis, we synthesize hybrid materials using silicon nanowires such that the synthesized materials have a relatively hard and soft component. In such a hybrid material the structure should be such that the hard component should be hidden in the soft one or vice-versa so that we could test for differential stiffness sensing by cells. Moreover, these hard-soft interfaces should be well integrated such that any external force applied can be transferred successfully between these components. Given one of our components is a cylindrical nanowire one way to ensure a mechanically well-coupled interface is to have the other component to coaxially

cover the nanowire. We could synthesize such coaxial hard-soft interface using nucleation governed by weak driving forces dominant in solution phases- such as pi stacking and van der Waals forces.

We synthesize coaxially pi stacked P3HT and van der Waals few layers graphene by self-assembly and mechanochemical synthesis, respectively. HAADF-STEM imaging of Si-Graphene hybrid indicates that the graphene forms like ribbon and cover the nanowire and extends outward (Fig. 4.4 b). Further, there is clear coaxial van der Waals stacking of ~0.34 nm[15] around silicon nanowire suggesting successful coaxial growth (Fig.4.4.a). The graphenic phase was verified using EELS and mapping (Fig.4.6.d-f). The EELS estimated composition [15] of graphene here was found to have 82.3 % sp^2 carbon and 17.17% sp^3 carbon which arises from the buckling [15] that the graphene happens to have from the ribbon-like morphology it exhibits (Fig.4.6.c). Further control mechanochemical synthesis done without nanowire yielded (< 1%) of denotation type nanodiamond (Fig.4.6.g) structure [16-17] which indicates the source of carbon for synthesis as the solvent -isopropanol. Further, the phase and composition of diamond estimated from EELS gave 33.3% sp^3 carbon and 66.6 % sp^2 carbon in agreement with the detonation type diamond structure (Fig.4.6.f).[16-17] This control experiment further suggests the role of silicon surface as a heat dissipater for controlling the phase of carbon nucleating and growing into a graphenic one.[18] Cryo-EM imaging indicates the coaxial lamellar arrangement of P3HT with a lamellar stacking of ~ 1.63 nm, typical of pi stacked P3HT structure (Fig.4.4.d, 4.5.c).[19-20] On a structural scale, the Si-P3HT hybrid has a P3HT shell around it, from which emanate multiple P3HT fibers to form an interlinked matrix which would

encase the nanowires (Fig.4.4.d, 4.5.a-b). In either case it is to be observed that the coaxial nucleation and growth was driven by the hydrophobicity of the nanowire, created by hydrofluoric acid treatment. Besides mechanical coupling between the hard and soft components electron energy loss spectroscopy (EELS) indicates that the bulk- plasmon coupling at the interface of either material suggesting that the interfaces are electronically coupled.[21-22] Electronically coupled interfaces generated by these synthetic methods further illustrate the strength of these synthetic methods suggesting their future optoelectronic utility.

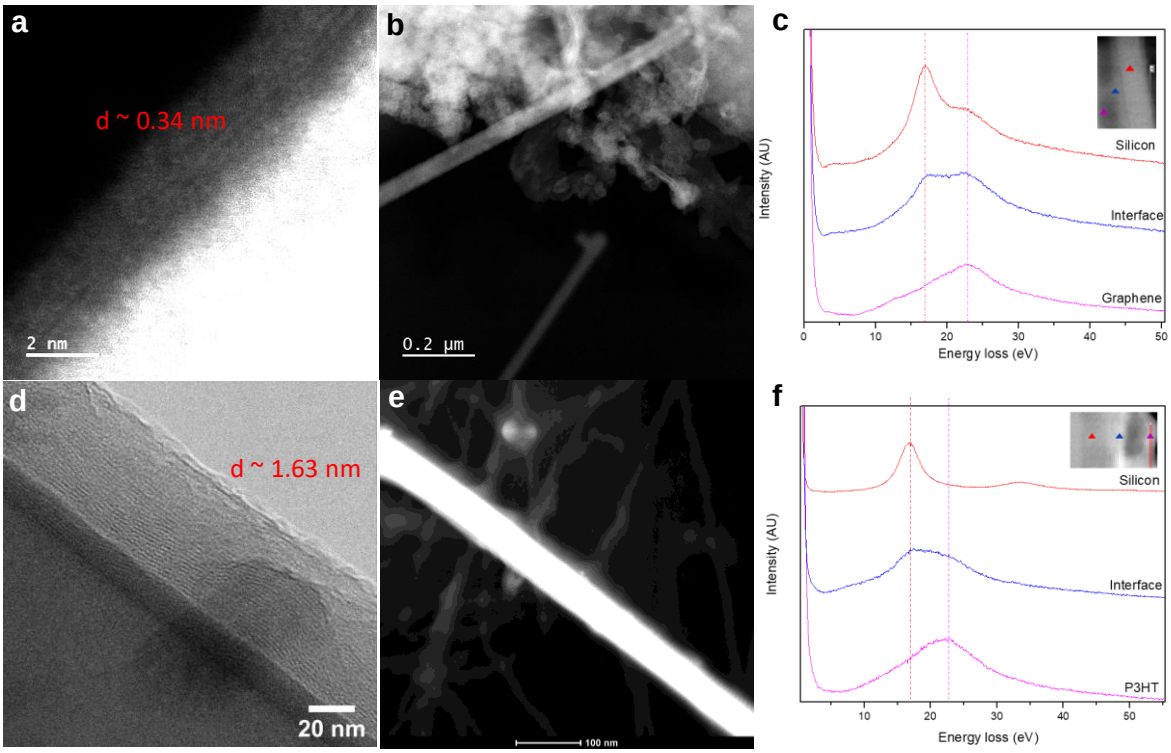

Fig.4.4. a. HAADF-STEM image of graphene layers coaxial with silicon nanowire. b. Large area HAADF-STEM image suggesting the growth of graphene around nanowire and its random outgrowth. c. Low loss EELS done at points across a Si-graphene interface to illustrate bulk plasmonic coupling. d. Cryo-EM image showing a coaxial lamellar stacking of P3HT with respect to a silicon nanowire. e.

Fig.4.4. continued. HAADF-STEM image showing coaxial shell of P3HT around nanowire and fibers emanating from them. f. Low loss EELS done at points across a Si-P3HT interface to illustrate bulk plasmonic coupling.

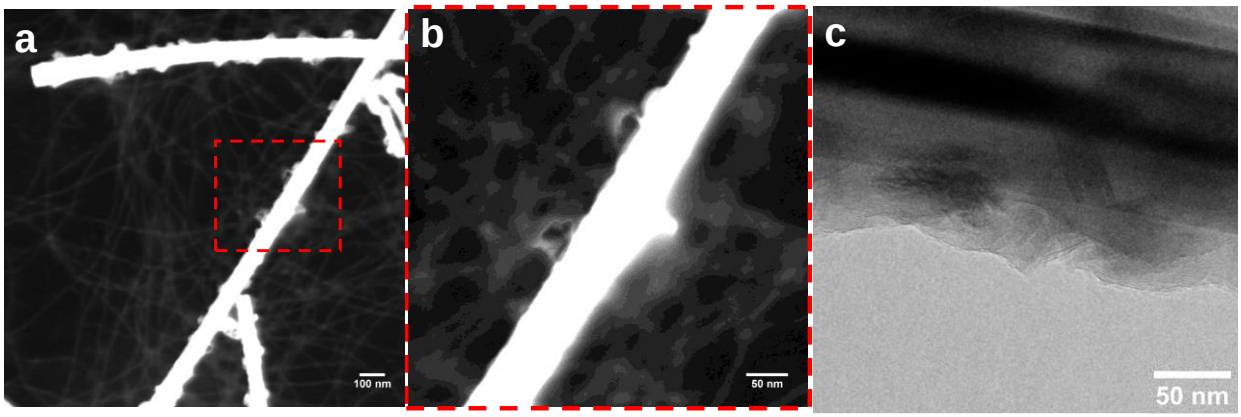

Fig.4.5. a. Large area HAADF-STEM image showing silicon nanowire as a part of P3HT network matrix. b. Higher magnification HAADF-STEM image showing P3HT forming a coaxial coating on silicon nanowire with nanofibers growing out of this coaxial coating, c. Cryo EM image indicating coaxial lamellar arrangement of P3HT even in fibers emanating from the coating.

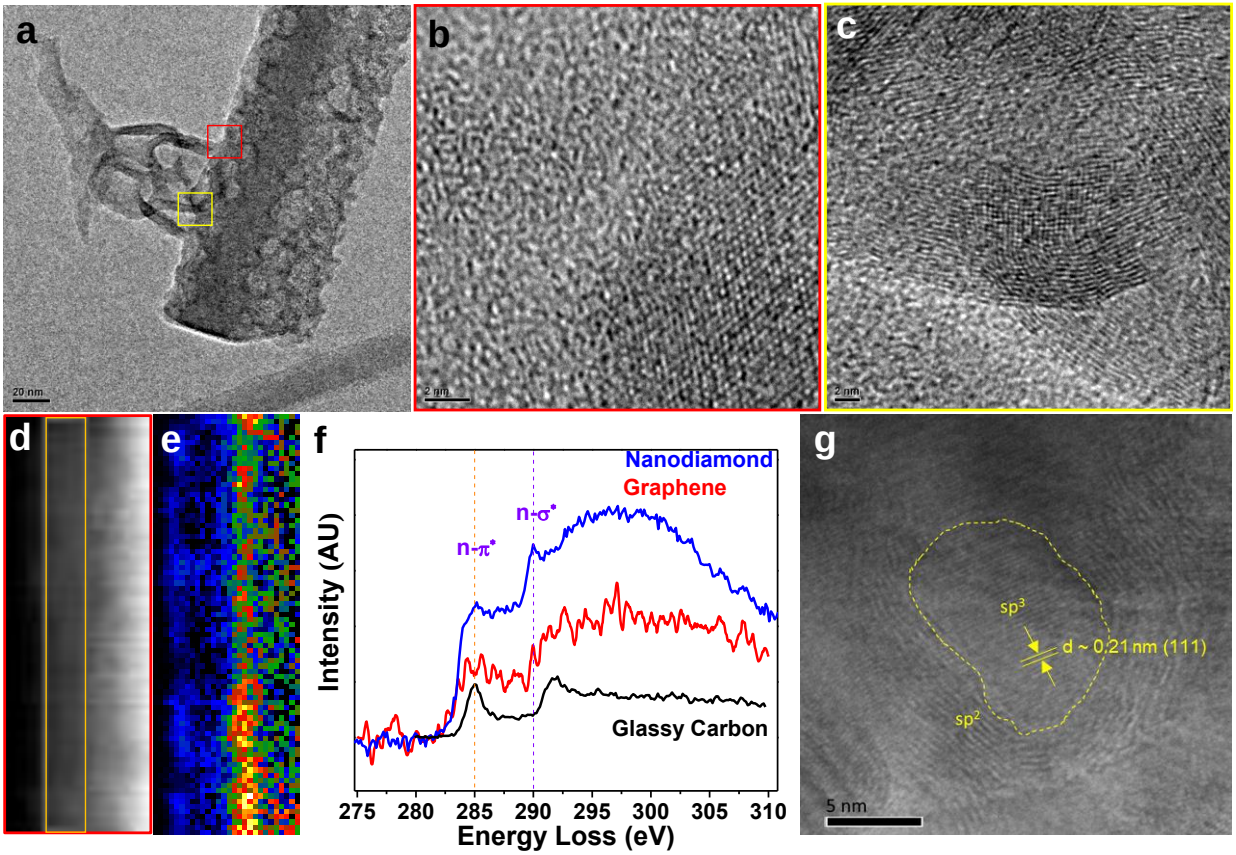

Fig.4.6. a. Coaxial coating of graphene on silicon nanowire and its emergence in ribbon form from the coating verified by high-resolution imaging in (c). b. Silicon lattice as seen through the graphemic coating in (a). d. EELS map of the silicon-graphene interface and its heat color map (e) for graphene sp^2 peak for the region marked in orange (e). The EELS map indicates a graphene coating (blue) outside the silicon nanowire and the sudden increase in intensity (red-green) arises due to reflection from the nanowire surface. f. High loss EELS spectrum of detonation nanodiamond, graphene in comparison with 100% sp^2 EELS standard – glassy carbon. g. Detonation type nondiamond structure with sp3 core with sp^2 graphitic shells coating, with core diamond structure having a lattice constant of 0.21 nm of 111 planes.

4.4. Mechanosensing of nanoscale hard-soft heterogeneity

Among the two synthesized hybrid structure candidates for testing mechanosensing, we need to consider the stability concerning external forces. It has been observed that the

Si-graphene interface is unstable as the harder substrate (Graphene- modulus of ~ 1TPa) is external to silicon (~ 100 GPa) and easily collapses to an external force.[23-24] Delamination of graphene from silicon due to mechanical mismatch and sliding due to weak van der Waals forces makes its biophysical behavior similar to a normal nanowire interface with a few added layers of graphene coating. Hence, we perform our nanoscale mechanosensing experiment using the Si-p3Ht hard-soft interface where the P3HT (~ MPa) is the soft component and silicon (~ 100 GPa) the harder one.

To perfume mechanosensing, we need a cellular readout which is proportional to rigidity differences but independent or superior to the topographical mechanotransduction due to the P3HT fiber framework. An ideal candidate for this would be caveolin 1. Though it is increased due to topographic features has a good dynamic range concerning rigidity sensing.[25,26] Moreover, it is important to use a cell line which actively responds to mechanical rigidity in a very profound way making MDA-MB-231 – a triple-negative breast cancer cell line as an available choice to test mechanosensing.[27]

MDA-MB-231 cells cultured on Si-P3HT hybrid matrices show very close to our expected behavior. The cells are shown to exhibit the filopodial extensions towards nanowires with

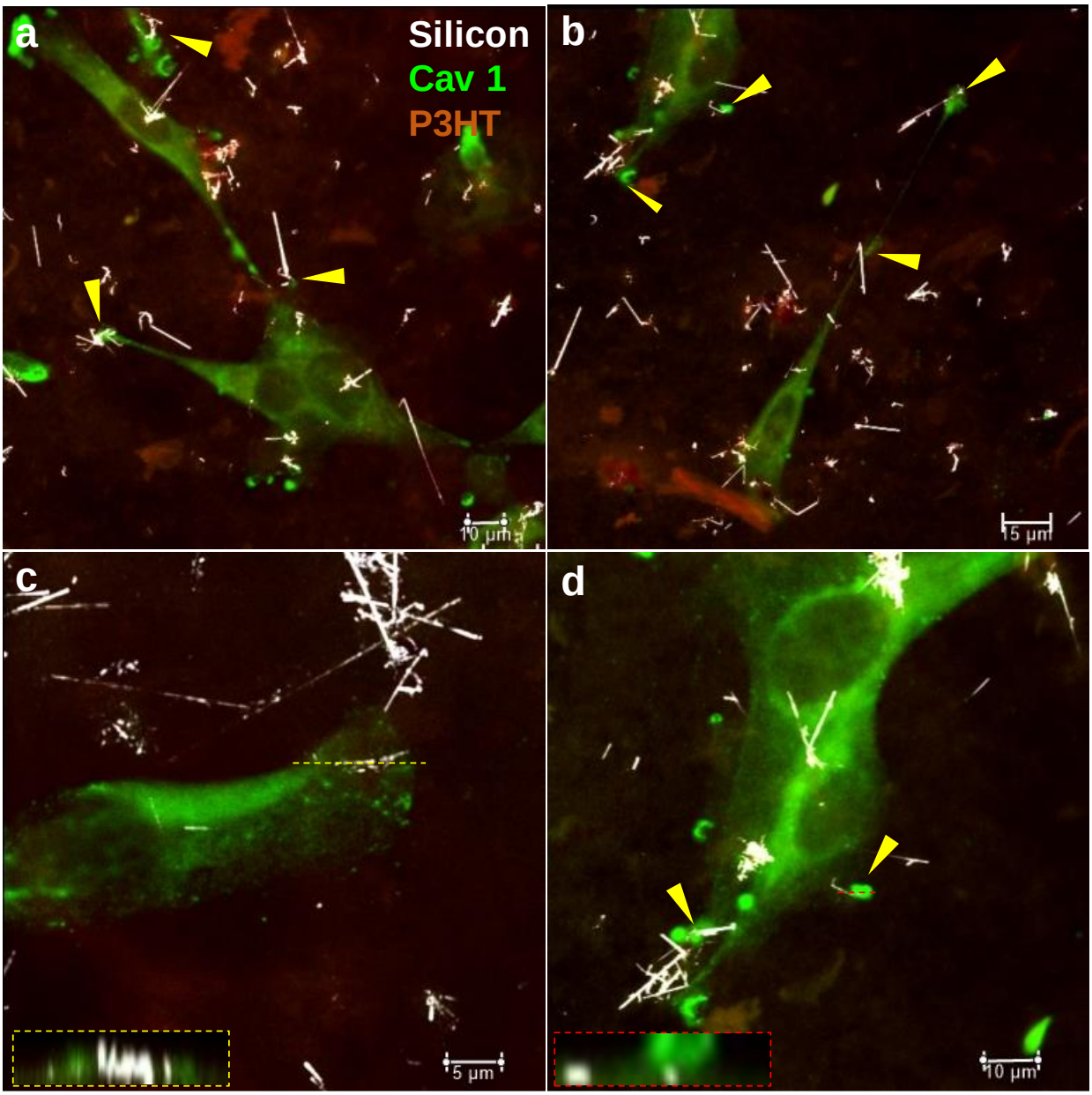

Fig.4.7. a. MDA-MB-231 cancer cells showing filopodial expression and increased caveolin vesicles at filopodial tip sensing nanowire in a soft matrix. b. Filopodia sensing two nanowires at the same time and showing increased expression of caveolin at either location. c. Nanowire near lamella attempting to be phagocytosed by the cell. The z-stack (inset) taken along the dotted line indicates a phagocytic vesicle formation with caveolin around the nanowire. d. Filopodia seeking a nanowire with the z-stack (inset) taken along dotted line indicating a caveolin rich vesicle above the nanowire.

increased caveolin expression on the detected nanowires (Fig. 4.7a,b,d). Even multiple nanowires were detected by a single filopodium with increased caveolin expression at different nanowire location. (Fig.4.7.b).This suggests that the cells have successfully been able to sense this nanowire hidden in a soft P3HT matrix. The caveolin expression increase is only found along the filopodia seeking out the nanowire. Three-dimensional stack collected on filopodia seeking a nanowire indicates increased caveolin expression in a big vesicular on the filopodia exactly above the nanowire (Fig.4.7.d). In contrast nanowires near the cellular lamella were perceived and recognized for phagocytosis causing vesicle formation and caveolin to surround this vesicle (Fig. 4.7.c). This confirms the capability of cells to sense differential rigidity in a matrix mediated by Brownian forces and the perception of hard materials with no chemical cues for phagocytosis.

4.5. Conclusion

In this work using a material development strategy that allows us to build matrices with nanoscale rigidity modulation, we demonstrate how cells are capable of sensing differential rigidity using the cytoskeletal framework and caveolin. Using free-standing nanowires, we understand how cylindrical objects are translated into the extracellular environment by the cells for phagocytosis by sequential control of lamellar projection. Further by embedding hard nanowires in a soft polymer matrix capable of coaxial self-assembly around it we use a hide and seek strategy to allows cells to seek nanowires hidden in these matrices. This confirms the capability of cells to recognize Brownian forces arising from rigidity changes in the local environment. From a synthetic viewpoint,

we gain knowledge on the mechanical stability of hard-soft interface and design principles. Besides we understand how hard-soft interfaces could possess electronic integration along with mechanical.

4.6. Experimental methods

Cell culture

Rat cardiac fibroblasts: P0-P5 neonatal rat hearts were isolated and placed into ice cold hanks balanced salt solution without calcium or magnesium (HBSS). Further these hearts were digested and fibroblasts obtained from them using Pierce cardiomyocyte culture kit (Thermo Fisher) by following manufacturers protocol. The cell suspension containing cardiomyocyte and fibroblasts were seeded in tissue culture plates for an hour to allow adherence of fibroblasts keeping the cardiomyocytes in the supernatant. The supernatant is removed and replaced with rat cardiac fibroblast media consisting of DMEM with 5% FBS, 1% Pen-Step and 1% Glutamax (Life technologies). MDA-MB-231 cells were obtained from the university of chicago cell screening facility and cultured in DMEM with 10% FBS and 1% Pen-Strep.

Synthesis of silicon nanowire, Si-P3HT hybrid and Si-Graphene hybrid

Silicon nanowires were grown using gold nanoparticle catalyzed VLS growth mechanism in a chemical vapor deposition system. Intrinsic nanowires were grown using 20 nm or 50 nm or 100 nm gold nanoparticle with silane as silicon precursor. The silane precursor was delivered at rate of 2 sccm mixed with hydrogen as a carrier gas delivered at rate of 60 sccm. The growth chamber was maintained at a pressure of 80 torr. The growth was

carried out for 20 minutes. The as grown silicon nanowires were cut into 1 cm x 1 cm piece and were treated with 5X buffered HF (Alfa Aesar) and gold etchant (Sigma Aldrich) for a minute each. Further these nanowires were sonicated and transferred into 10 mL HPLC grade isopropanol (Alfa Aesar) or cyclohexanone for Si-Graphene and Si-P3HT hybrid synthesis respectively.

0.2 mg of RR-P3HT (Sigma Aldrich) is mixed with 5 mL of nanowire-cyclohexanone dispersion (Sigma Aldrich) and nitrogen gas bubbled through the solvent for an hour before raising the temperature to 120 C under vacuum conditions. Once at 120 C for an hour slowly ramp down to room temperature with 20C every hour under vacuum and keep at room temperature overnight. All reactions to be done under dark or limited lighting. For synthesis of Si-graphene, the dispersion of silicon nanowire in 10 mL filtered HPLC grade isopropanol was probe sonicated using a 13 mm diameter $Ti_4Al_6V_4$ cylindrical probe (Sonics VC 750) with a duty cycle of 66.66% and power radiating at the tip to be around 20 W. Control experiments were performed without nanowires under similar experiment.

Electron microscopy and spectroscopy

TEM and STEM images for Si-P3HT hybrid and detonation nanodiamond were collected on FEI Technai Twin F30 with an accelerating voltage of 300 kV. STEM for Si-graphene were done on a JEOL ARM 200CF (Cs corrected) with a field emission gun at an accelerating voltage of 200 kV. All EELS measurements were done on each area after a 200 kV, 30 min beam shower at the spot to remove any adsorbed hydrocarbon contaminants. EELS was collected using a gatan dual EELS detector at magic angle.

TEM imaging for Si-graphene and structures and all electron diffraction was done on JEOL JEM 3010F scope at an accelerating voltage of 300kV with a LaB_6 emission.

Raman spectroscopy

Raman spectrum was collected on Horiba LabRAM HR Evo Confocal Raman using a 473 nm excitation laser with detection in a back-scattered geometry with a 50X/0.5 NA objective and 600 grooves/mm grating, under ambient conditions.

Actin -GFP transfection

Rat cardiac fibroblast were transfected with Actin-GFP plasmids in baculovirus using Cell light Actin reagent (Thermo-Fisher). Manufacturers protocol was followed for transfection.

Immunofluorescence staining

Caveolin 1 staining was done using Anti-Caveolin-1 conjugated with Alexa Fluor 488, Clone: 7C8 (Novus biologicals) at a concentration of 20 µg/mL overnight at 4C, after fixation and permeabilization. Nuclear staining was done using NucBlue Live ReadyProbes (Thermo Fisher) as per manufacturers protocol.

Confocal imaging

Confocal live imaging was done of a LEICA SP5 STED-CW system. Immunofluorescence imaging was done on a LEICA SP5 two photon microscope.

References

1. Bavi, N.; Nikolaev, Y. A.; Bavi, O.; Ridone, P.; Martinac, A. D.; Nakayama, Y.; Cox, C. D.; Martinac, B. Principles of Mechanosensing at the Membrane Interface. In The Biophysics of Cell Membranes; Epand, R. M., Ruysschaert, J.-M., Eds.; Springer Singapore: Singapore, 2017; Vol. 19, pp 85–119.

2. Akhmanova, M.; Osidak, E.; Domogatsky, S.; Rodin, S.; Domogatskaya, A. Physical, Spatial, and Molecular Aspects of Extracellular Matrix of In Vivo Niches and Artificial Scaffolds Relevant to Stem Cells Research. Stem Cells Int 2015, 2015.

3. Escudé, M.; Rigozzi, M. K.; Terentjev, E. M. How Cells Feel: Stochastic Model for a Molecular Mechanosensor. Biophysical Journal 2014, 106 (1), 124–133.

4. Wipff, P.-J.; Rifkin, D. B.; Meister, J.-J.; Hinz, B. Myofibroblast Contraction Activates Latent TGF-B1 from the Extracellular Matrix. J Cell Biol 2007, 179 (6), 1311–1323.

5. Schwarz, U. S.; Erdmann, T.; Bischofs, I. B. Focal Adhesions as Mechanosensors: The Two-Spring Model. Biosystems 2006, 83 (2–3), 225–232.

6. Parameswaran, R.; Carvalho-de-Souza, J. L.; Jiang, Y.; Burke, M. J.; Zimmerman, J. F.; Koehler, K.; Phillips, A. W.; Yi, J.; Adams, E. J.; Bezanilla, F.; et al. Photoelectrochemical Modulation of Neuronal Activity with Free-Standing Coaxial Silicon Nanowires. Nature Nanotech 2018, 13 (3), 260–266.

7. Jiang, Y.; Li, X.; Liu, B.; Yi, J.; Fang, Y.; Shi, F.; Gao, X.; Sudzilovsky, E.; Parameswaran, R.; Koehler, K.; et al. Rational Design of Silicon Structures for Optically Controlled Multiscale Biointerfaces. Nat Biomed Eng 2018, 2 (7), 508–521.

8. Zimmerman, J. F.; Parameswaran, R.; Murray, G.; Wang, Y.; Burke, M.; Tian, B. Cellular Uptake and Dynamics of Unlabeled Freestanding Silicon Nanowires. Sci. Adv. 2016, 2 (12), e1601039.

9. Zimmerman, J. F.; Murray, G. F.; Wang, Y.; Jumper, J. M.; Austin, J. R.; Tian, B. Free-Standing Kinked Silicon Nanowires for Probing Inter- and Intracellular Force Dynamics. Nano Lett. 2015, 15 (8), 5492–5498.

10. Heckman, C. A.; Plummer, H. K. Filopodia as Sensors. Cellular Signalling 2013, 25 (11), 2298–2311.

11. Jacquemet, G.; Hamidi, H.; Ivaska, J. Filopodia in Cell Adhesion, 3D Migration and Cancer Cell Invasion. Current Opinion in Cell Biology 2015, 36, 23–31.

12. Jansen, K. A.; Atherton, P.; Ballestrem, C. Mechanotransduction at the Cell-Matrix Interface. Seminars in Cell & Developmental Biology 2017, 71, 75–83.

13. Kress, H.; Stelzer, E. H. K.; Holzer, D.; Buss, F.; Griffiths, G.; Rohrbach, A. Filopodia Act as Phagocytic Tentacles and Pull with Discrete Steps and a Load-Dependent Velocity. Proceedings of the National Academy of Sciences 2007, 104 (28), 11633–11638.

14. Nemethova, M.; Auinger, S.; Small, J. V. Building the Actin Cytoskeleton: Filopodia Contribute to the Construction of Contractile Bundles in the Lamella. J Cell Biol 2008, 180 (6), 1233–1244.

15. Hu, M.; He, J.; Zhao, Z.; Strobel, T. A.; Hu, W.; Yu, D.; Sun, H.; Liu, L.; Li, Z.; Ma, M.; et al. Compressed Glassy Carbon: An Ultrastrong and Elastic Interpenetrating Graphene Network. Sci. Adv. 2017, 3 (6), e1603213.

16. Osswald, S.; Yushin, G.; Mochalin, V.; Kucheyev, S. O.; Gogotsi, Y. Control of Sp 2 /Sp 3 Carbon Ratio and Surface Chemistry of Nanodiamond Powders by Selective Oxidation in Air. J. Am. Chem. Soc. 2006, 128 (35), 11635–11642.

17. Mochalin, V. N.; Shenderova, O.; Ho, D.; Gogotsi, Y. The Properties and Applications of Nanodiamonds. Nature Nanotech 2012, 7 (1), 11–23.

18. Chen, R.; Lu, M.-C.; Srinivasan, V.; Wang, Z.; Cho, H. H.; Majumdar, A. Nanowires for Enhanced Boiling Heat Transfer. Nano Lett. 2009, 9 (2), 548–553.

19. Kleinhenz, N.; Persson, N.; Xue, Z.; Chu, P. H.; Wang, G.; Yuan, Z.; McBride, M. A.; Choi, D.; Grover, M. A.; Reichmanis, E. Ordering of Poly(3-Hexylthiophene) in Solutions and Films: Effects of Fiber Length and Grain Boundaries on Anisotropy and Mobility. Chem. Mater. 2016, 28 (11), 3905–3913.

20. Nair, V.; Kumar, A.; Subramaniam, C. Exceptional Photoconductivity of Poly(3-Hexylthiophene) Fibers through in Situ Encapsulation of Molybdenum Disulfide Quantum Dots. Nanoscale 2018, 10 (22), 10395–10402.

21. Petoukhoff, C. E.; O'Carroll, D. M. Absorption-Induced Scattering and Surface Plasmon out-Coupling from Absorber-Coated Plasmonic Metasurfaces. Nat Commun 2015, 6 (1), 7899.

22. Hooshmand, N.; El-Sayed, M. A. Collective Multipole Oscillations Direct the Plasmonic Coupling at the Nanojunction Interfaces. Proc Natl Acad Sci USA 2019, 116 (39), 19299–19304.

23. Liew, K. M.; Yan, J.-W.; Zhang, L.-W. 2-D Graphene and White Graphene. In Mechanical Behaviors of Carbon Nanotubes; Elsevier, 2017; pp 387–410.

24. Sohn, Y.-S.; Park, J.; Yoon, G.; Song, J.; Jee, S.-W.; Lee, J.-H.; Na, S.; Kwon, T.; Eom, K. Mechanical Properties of Silicon Nanowires. Nanoscale Res Lett 2010, 5 (1), 211–216.

25. Pennacchio, F. A.; Caliendo, F.; Iaccarino, G.; Langella, A.; Siciliano, V.; Santoro, F. Three-Dimensionally Patterned Scaffolds Modulate the Biointerface at the Nanoscale. Nano Lett. 2019, 19 (8), 5118–5123

26. Yeh, Y.-C.; Ling, J.-Y.; Chen, W.-C.; Lin, H.-H.; Tang, M.-J. Mechanotransduction of Matrix Stiffness in Regulation of Focal Adhesion Size and Number: Reciprocal Regulation of Caveolin-1 and B1 Integrin. Sci Rep 2017, 7 (1), 15008.

27. Tilghman, R. W.; Cowan, C. R.; Mih, J. D.; Koryakina, Y.; Gioeli, D.; Slack-Davis, J. K.; Blackman, B. R.; Tschumperlin, D. J.; Parsons, J. T. Matrix Rigidity Regulates Cancer Cell Growth and Cellular Phenotype. PLoS ONE 2010, 5 (9), e12905.

28. Kumar, A.; Ann Lin, P.; Xue, A.; Hao, B.; Khin Yap, Y.; Sankaran, R. M. Formation of Nanodiamonds at Near-Ambient Conditions via Microplasma Dissociation of Ethanol Vapour. Nat Commun 2013, 4 (1), 2618.

29. Chu, P. K.; Li, L. Characterization of Amorphous and Nanocrystalline Carbon Films. Materials Chemistry and Physics 2006, 96 (2–3), 253–277.

5. Future directions

5.1. Silicon as a mineralizing biointerface in plants

Silicon has always played a versatile chemical role in nature leading to its existence in a variety of living and non-living forms that co-exist or are separate. Extending from plant to animal kingdom we have a variety of systems that can metabolize pure silicon into various forms of oxides or silicate like structures.[1-2] However, the biochemical role is more often significantly noted in plants and the geochemical cycle. [1-2] This forms a basis for exploring silicon nanowire uptake, metabolism and consequences in plants as a first step. Silicon also plays the role of a nutrient in plants and hence could control signaling pathways for defense and priming.[3-5]

An initial experiment was performed to study the uptake of as-synthesized nanowire in *Arabidopsis thaliana* plants from liquid media culture. This initial experiment wherein plants were treated with nanowire containing media was carried out for two weeks. Electron micrographs of two-week-old plant roots revealed the attachment of intact nanowire to epidermal cells (Fig.5.1.a-b) and presence of degraded nanowire (Fig.5.1.e-f) in vacuoles of cells in vascular bundle. The degrade nanowires were attached to actin or microtubule cytoskeletal filaments in the vacuole (Fig.5.1.f) [6,7] indicating their active transport. Besides we find mesoporous silicate structures in vacuoles of vascular bundle cells suggesting the mineralization of silicon nanowires in plants (Fig.5.1.g-h).

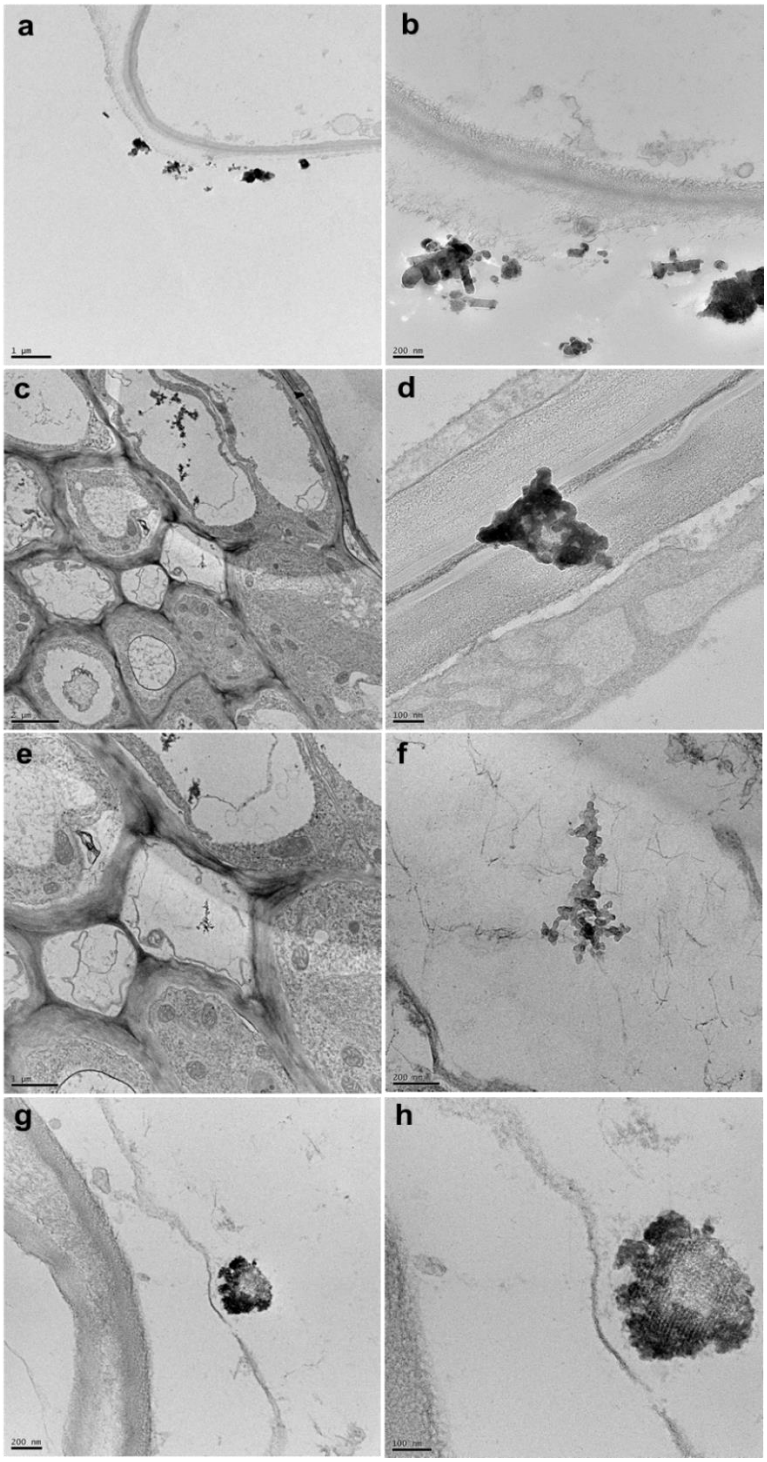

Fig.5.1. a TEM image showing nanowire attached to epidermal root cells, b. Magnified view of (a), c. Vascular bundle of the plant root with nanowire degraded

Fig. 5.1. continued. fragments in cells, d. Nanowire chunk trapped in cell wall between epidermal cell and a vascular bundle cell. e. A cell in vascular bundle having a linear degraded nanowire, f. Magnified view of (e) showing degraded nanowire in vacuole with actin filaments around it. g. Degraded nanowire forming porous silicate formation in root cell, h. magnified view of (g) showing mesoporous structure.

Besides uptake in liquid culture parallel studies were carried out experiments on plants growing in modified agar media to study the effect of ultrasound on plants and nanowire. Here is aim is to check is ultrasound affects the capability of plants to uptake silicon and if it can accelerate the degradation process of nanowires to silicates inside or outside the plants. Initial batch of plants that were studied were analyzed for silicon content using Inductively coupled plasma-atomic emission spectroscopy. The silicon content in control plants with no nanowire added to the media show small in increase in silicon uptake by plants (Fig.5.2.b). Simple addition of nanowire to agar media without sonication significantly increased silicon content in plants which however when coupled with sonication drastically fell (Fig.5.2.b). The concentration of silicon in agar, however, remains invariant (Fig.5.2.c). The role of sonication to interpret here is tricky as multiple cavitation mediated processes are happening and a systematic study as to how each possible process affects needs to study. Irrespective of that the big picture behind this study is to understand the mechanism nanowire uptake in plant roots and the effect of silicon on plant defense and priming.

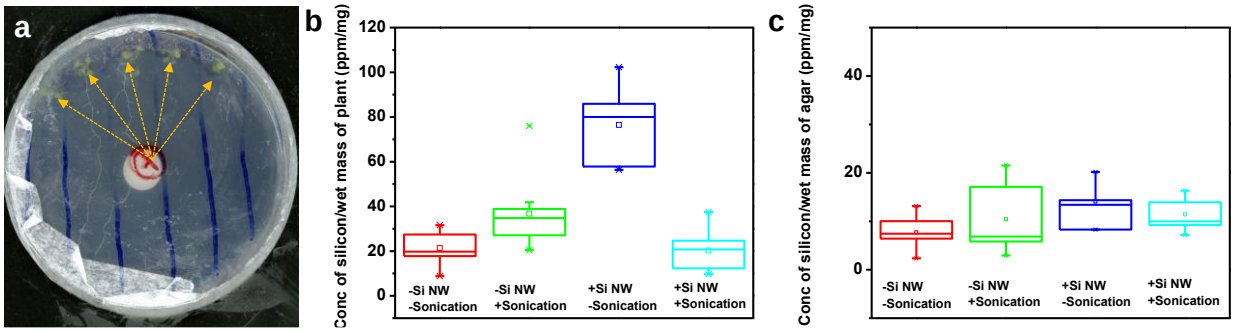

Fig.5.2. a. Plant seedling growing on agar plate showing a radially symmetric spot marked for application of ultrasound, b. The concentration of silicon in ten two-week-old plants under various growth conditions on the agar plate, c. The concentration of silicon in ten agar samples taken from a plant grown and dishes treated under various growth conditions.

5.2. Crystal orientation-dependent photoelectrochemistry for redox biology

Crystal orientation-dependent catalytic properties have been well explored in nanoscale catalysis.[8,9] These differential properties arise from variation in surface energies which also can affect electrochemical properties.[8,9] The surface properties affect the differential double-layer capacitance and hence the electrochemical behavior. Band structure variation along different crystal orientations often couple with these differences in surface energy can give rise to orientation-dependent photoelectrochemical properties.[8] Thus, crystal orientation is a tuning gear from a biointerface design perspective to bring forward specificity in photoelectrochemical stimulation of cells.

Silicon has been a good candidate for this however its main drawback is the formation of the oxide layer. Hence investigations on these were abandoned in the late 90s. However, it is possible that the coating nanoscale metal layer or semiconductor layers on silicon

could enable us to harvest these properties for bioelectronics. Freshly hydrofluoric acid etched silicon 100 and 111 wafers of n and p doping show varied faradaic and capacitive properties (Fig. 5.3) suggesting that the fact that crystal orientation has immense potential as a tuning gear in biointerface development. Besides crystals orientation doing controls the relative extent to which the capacitive and faradic processes are occurring.

The utility of such interfaces lies in the control of specific biochemical redox processes. Furthermore, this is a concept that can well extend to other biocompatible semiconductors and junctions unraveling a whole new facet dependent nanomaterial design methods for biointerface development.

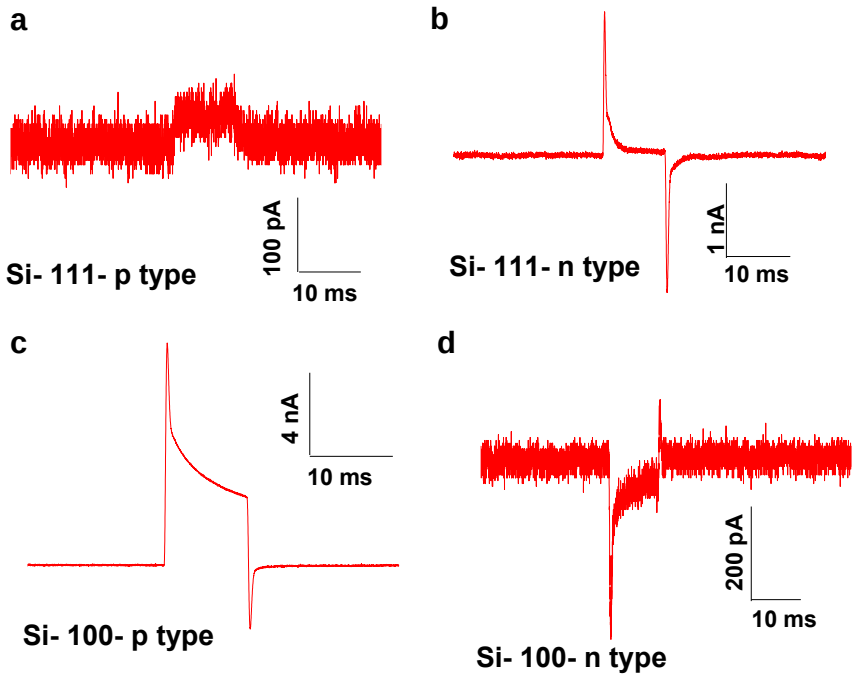

Fig.5.3. a. Silicon 111 p type wafer showing pure faradaic reduction effect, b. Silicon 111 n type wafer showing pure and dominating capacitive and very small faradic

Fig. 5.3. continued. reduction effect, c. Silicon 100 p type showing dominant faradaic reduction effect and capacitive effect, d. Silicon 100 n type showing capacitive effect with faradaic oxidation effect.

5.3. Experimental methods

Plant culture

Columbia wild type *Arabidopsis thaliana* seeds were sterilized and placed in half-MS liquid culture or agar plates post winterization**.** Media was a modified with nanowire by sonicating nanowire grown silicon chips in media before their sterilization**.**

Ultra sound treatment

An ultrasound probe (Chattanooga medical supply company) of 5 cm^2 area was placed at the center of a circular agar plate with seeds places radially (Fig.5.2.a). Ultrasound pulses of 1 W/cm^2 intensity was applied at a frequency of 1 MHz with a duty cycle of 50%, twice daily.

Electron microscopy

Plant roots were fixed in with 2.5% Glutaraldehyde in sodium cacodylate buffer and embedded in Spurrs resin (EMS) following manufacturers protocol. They were microtomed into 90 nm sections and imaged on a Technai F30 twin scope at an accelerating voltage of 300 kV.

Inductively coupled plasma-atomic emission spectroscopy (ICP-AES)

Each two-week-old plant was freeze dried and digested in 400 µL of conc. HNO_3 and 100 µL of 15% H_2O_2 and volume made upto 5 mL. ICP-OES was then run on Agilent 700 Series spectrometer.

Photocurrent measurements

Photocurrent measurements were performed by single channel voltage clamped recordings on a patch-clamp amplifier (Axopatch 200B) set up. The material of interest was immersed in 1X PBS (Fisher Scientific) in a petridish and focused on using a microscope (Olympus BX61WI) with a water immersion lens (20X/0.5 NA). Light pulses are delivered through the microscope using a 514.5 nm LED source (Thorlabs, ~ 500 µm spot size). Light pulses were delivered to these light sources using a digitizer (Molecular devices, Digidata 1550). For measuring the photocurrent measurements glass pipettes of ~ 1 MΩ were pulled (Sutter Instrument, P-97) and their tip lowered and focused onto the same optical plane (Gap of ~2 µm) as the material surface before the stimulation pulse is applied. The voltage clamped currents were recorded at -0.5 V bias in parallel with the stimulation pulse at various holding current levels.

References

1. Wang, B.; Liu, C.-Q.; Maberly, S. C.; Wang, F.; Hartmann, J. Coupling of Carbon and Silicon Geochemical Cycles in Rivers and Lakes. Sci Rep 2016, 6 (1), 35832.

2. Struyf, E.; Smis, A.; Van Damme, S.; Meire, P.; Conley, D. J. The Global Biogeochemical Silicon Cycle. Silicon 2009, 1 (4), 207–213.

3. Deshmukh, R. K.; Ma, J. F.; Bélanger, R. R. Editorial: Role of Silicon in Plants. Front. Plant Sci. 2017, 8, 1858.

4. Sahebi, M.; Hanafi, M. M.; Siti Nor Akmar, A.; Rafii, M. Y.; Azizi, P.; Tengoua, F. F.; Nurul Mayzaitul Azwa, J.; Shabanimofrad, M. Importance of Silicon and Mechanisms of Biosilica Formation in Plants. BioMed Research International 2015, 2015, 1–16.

5. Wang, M.; Gao, L.; Dong, S.; Sun, Y.; Shen, Q.; Guo, S. Role of Silicon on Plant–Pathogen Interactions. Front. Plant Sci. 2017, 8, 701.

6. Kost, B.; Chua, N.-H. The Plant Cytoskeleton. Cell 2002, 108 (1), 9–12.

7. Zhang, C.; Hicks, G. R.; Raikhel, N. V. Plant Vacuole Morphology and Vacuolar Trafficking. Front. Plant Sci. 2014, 5.

8. Li, D.; Liu, Y.; Shi, W.; Shao, C.; Wang, S.; Ding, C.; Liu, T.; Fan, F.; Shi, J.; Li, C. Crystallographic-Orientation-Dependent Charge Separation of BiVO 4 for Solar Water Oxidation. ACS Energy Lett. 2019, 4 (4), 825–831.

9. Chatterjee, D.; R, A.; Kamalnath, K.; Ahmad, R.; Singh, A. K.; Ravishankar, N. Orientation Selection during Heterogeneous Nucleation: Implications for Heterogeneous Catalysis. J. Phys. Chem. C 2017, 121 (18), 10027–10037.

6. Conclusion

Starting out with the goal of evolving the field of bioelectronics by bringing forward material design aspects have led to the introduction of many new material systems which are capable of exerting specific cues on cells. The first design strategy was to laser write semiconducting patterns in an insulating mold to obtain biointerfaces whose property could be controlled by additives in starting material or surface functionalization. This strategy was built to illustrate the idea that material property and functionality correlation arises from the synthetic tuning gears. These tuning gears on property ultimately gave rise to the availability of different stimulation modes ranging from photoelectrochemical, photothermal and electrical. Each of these modes were matched with an appropriate biological system with signaling pathways capable of responding to these stimuli modes. These stimuli mode push the cell into non-equilibrium states which enable the cell to respond using specific signaling pathways allowing for thoughts on therapeutic utility. Besides we translate the bioelectronic modulation from cells to cell networks to affect synchronization to understand the capability of bioelectronic modulation in controlling chaotic systems. Further this design strategy contributes to the big picture of building a bioelectronic material library or genome.

The second design strategy was built based on biomimicry of extracellular matrix proteins. This involves searching for the right material candidate and synthetic tool to assemble them into a similar morphology. However, the choice of a semiconductor material makes the designed material have multiple modes of stimulation by enabling optical and

electrical coupling. This enables the development of optoelectronically active extra cellular matrix. The optoelectronic activity leads the cells being apoptotic under photothermal effect and stimulated under photoelectrochemical effect. Besides we look at how neuronal networks interact with ECM like materials and their mechanical cues. Ultimately this strategy enables multimodality besides mechanotransduction of softness and topography of the matrix.

The third design strategy was to design a material in order to test a biophysical hypothesis. Though understanding of a biophysical hypothesis is suggestive of the underlying signaling pathway and methods to tune it for therapeutic applications. Besides the synthetic methodology used here suggests us the utility of hard-soft interfaces in biology and their recognition by biological entities.

To summarize, different material design strategies were developed to understand how a one on one correlation between nanomaterial properties and signaling cues could be achieved.

Appendix

A1. Extended data and figures for Chapter 2

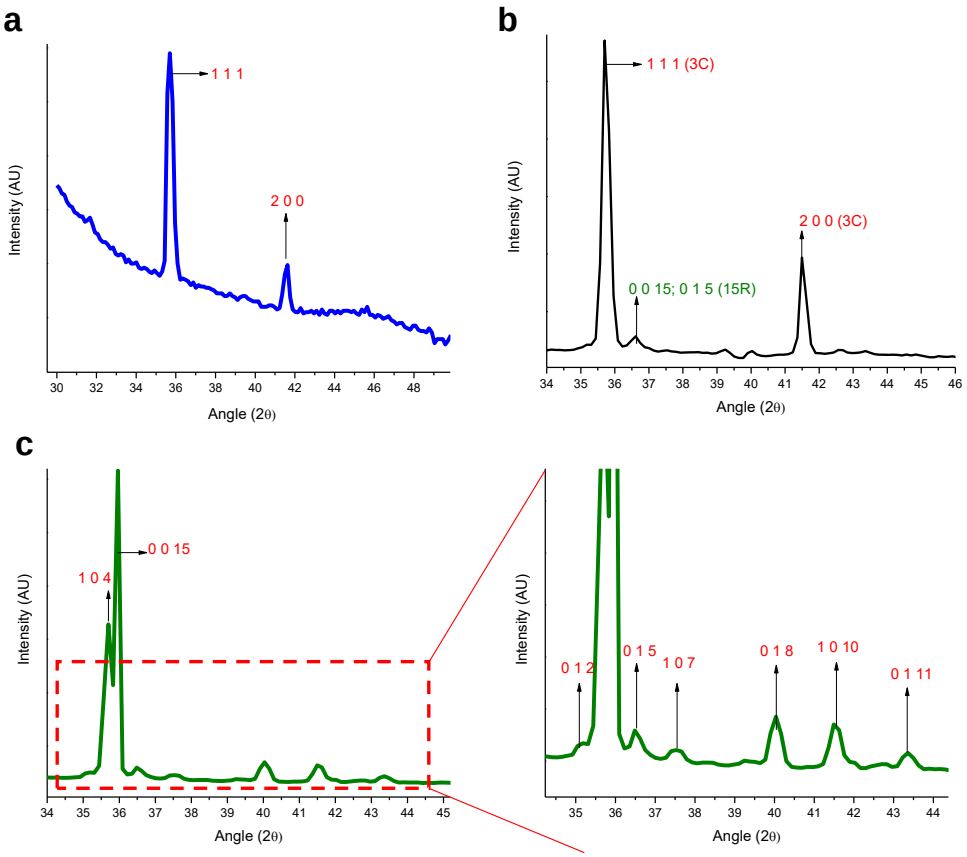

Fig. A.1.1. a. Wide angle X-ray scattering (WAXS) collected for pure 3C-SiC sample. b. WAXS collected on a M-SiC sample showing mixed 3C and 15R polytypes existing on that sample. c. WAXS collected for M-SiC sample at a specific spot showing a 15R polytypic phase of SiC, revealing phase separation during synthesis. The indexing of phases was done using peaks from (*36*).

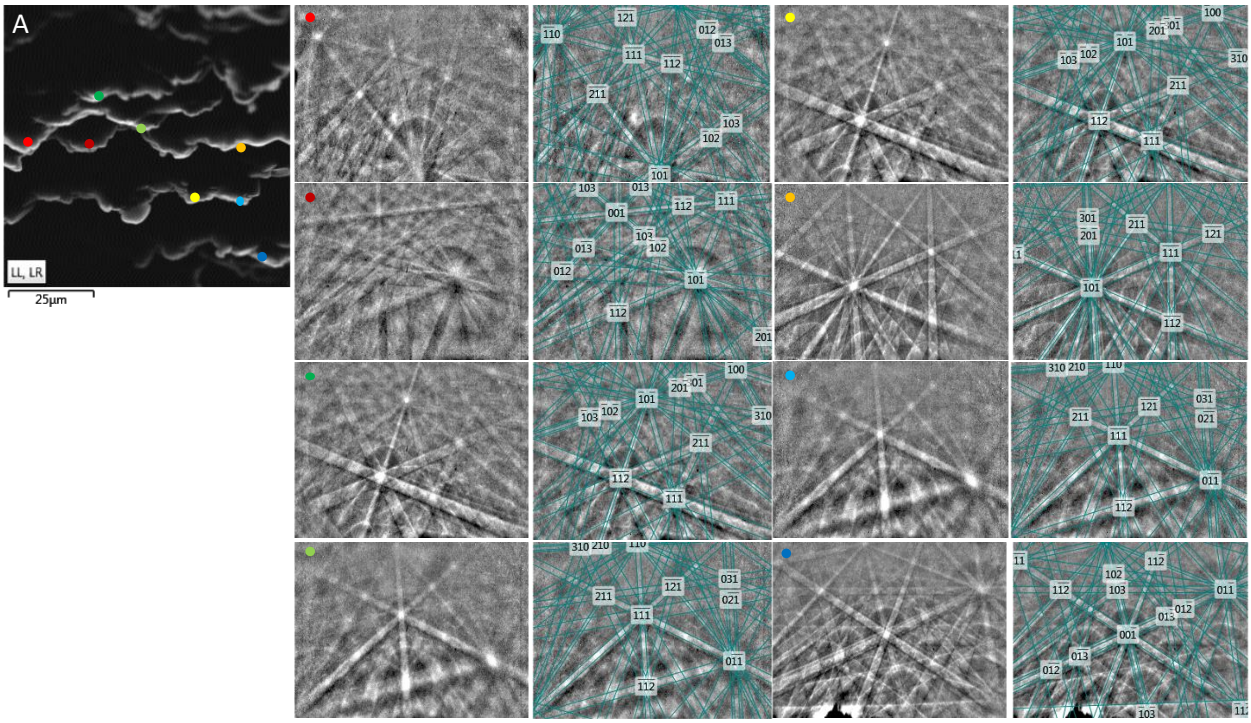
A
LL, LR
25μm

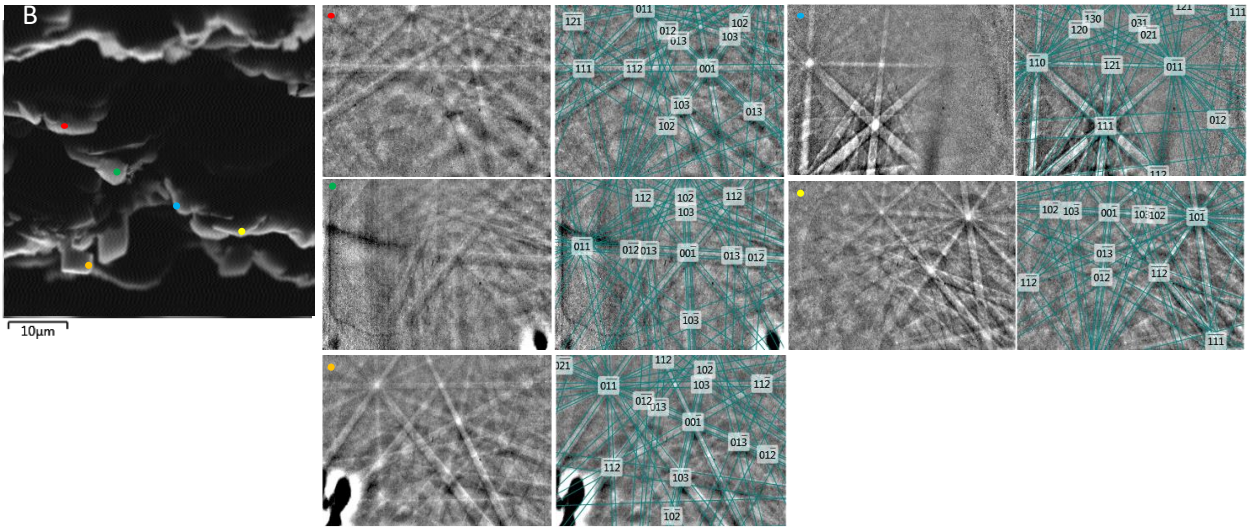
B
10μm

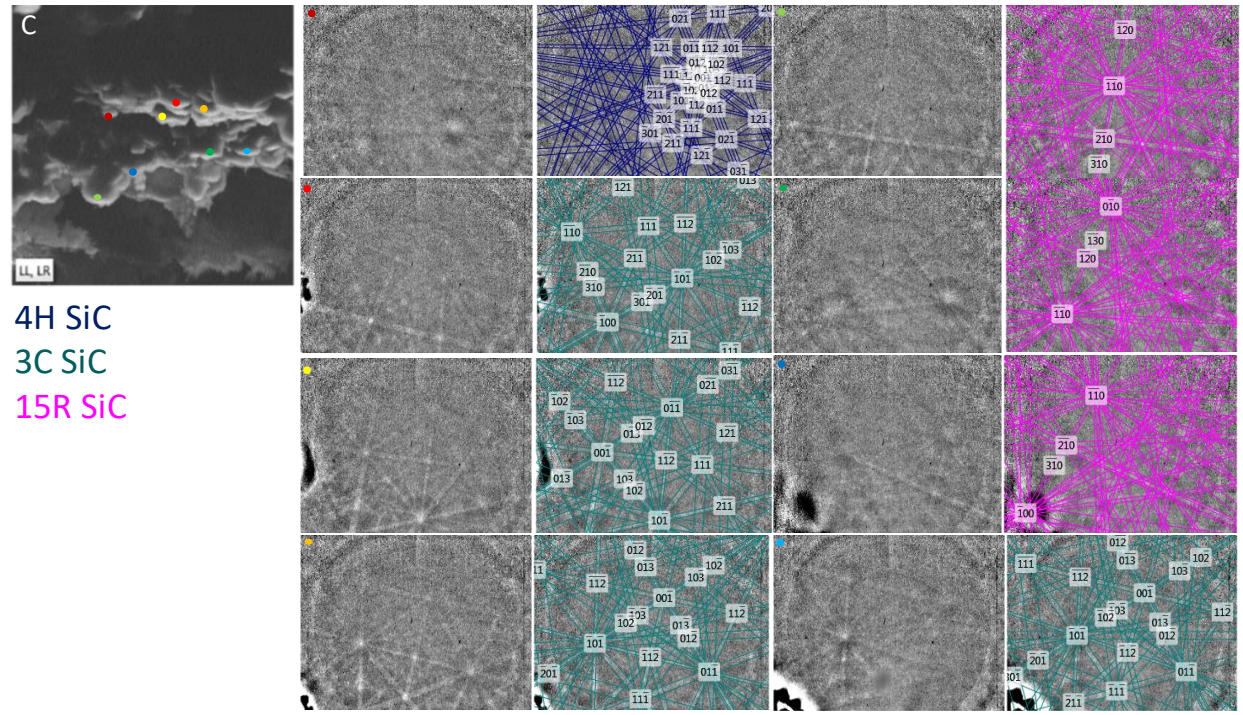
C
LL, LR
4H SiC
3C SiC
15R SiC

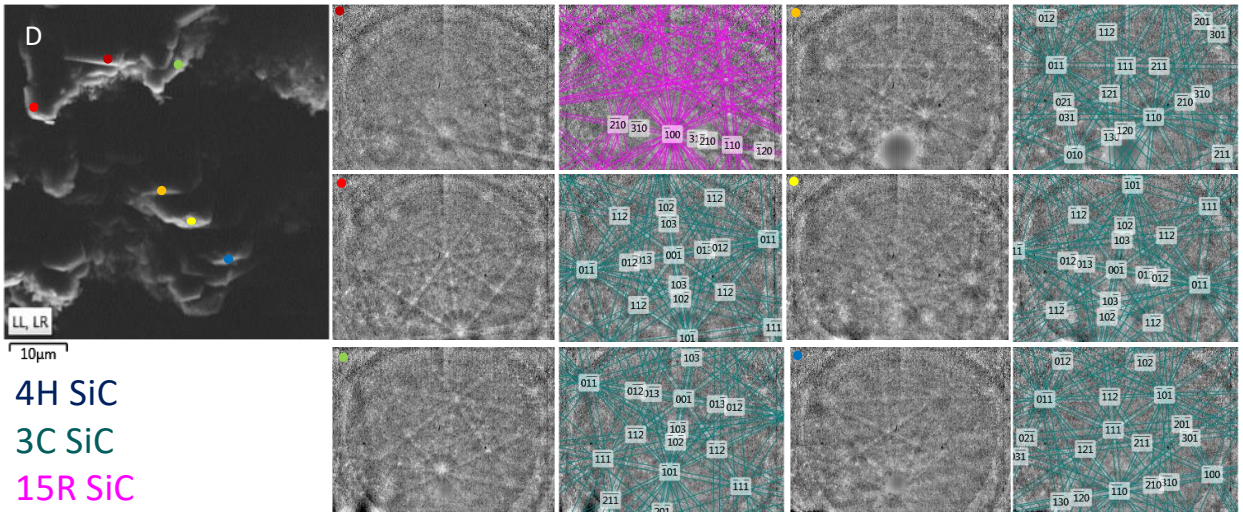
D
LL, LR
10µm
4H SiC
3C SiC
15R SiC

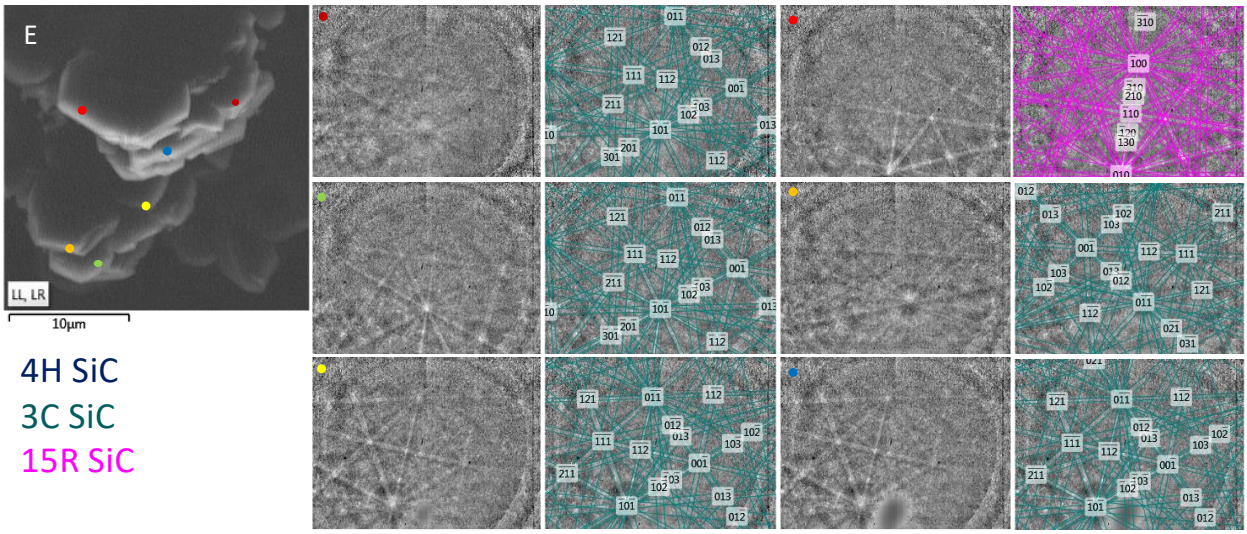

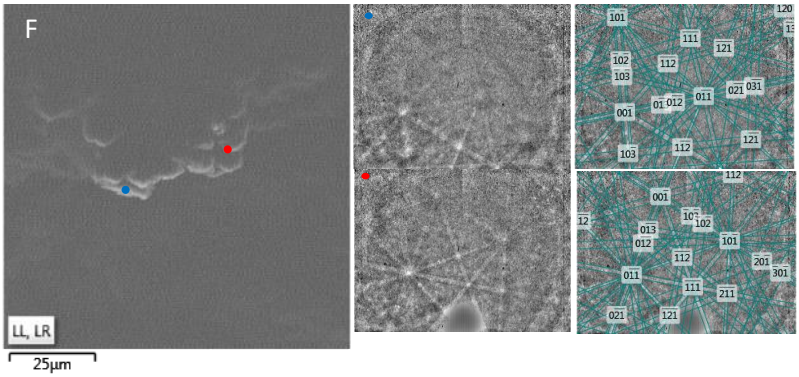

4H SiC
3C SiC
15R SiC

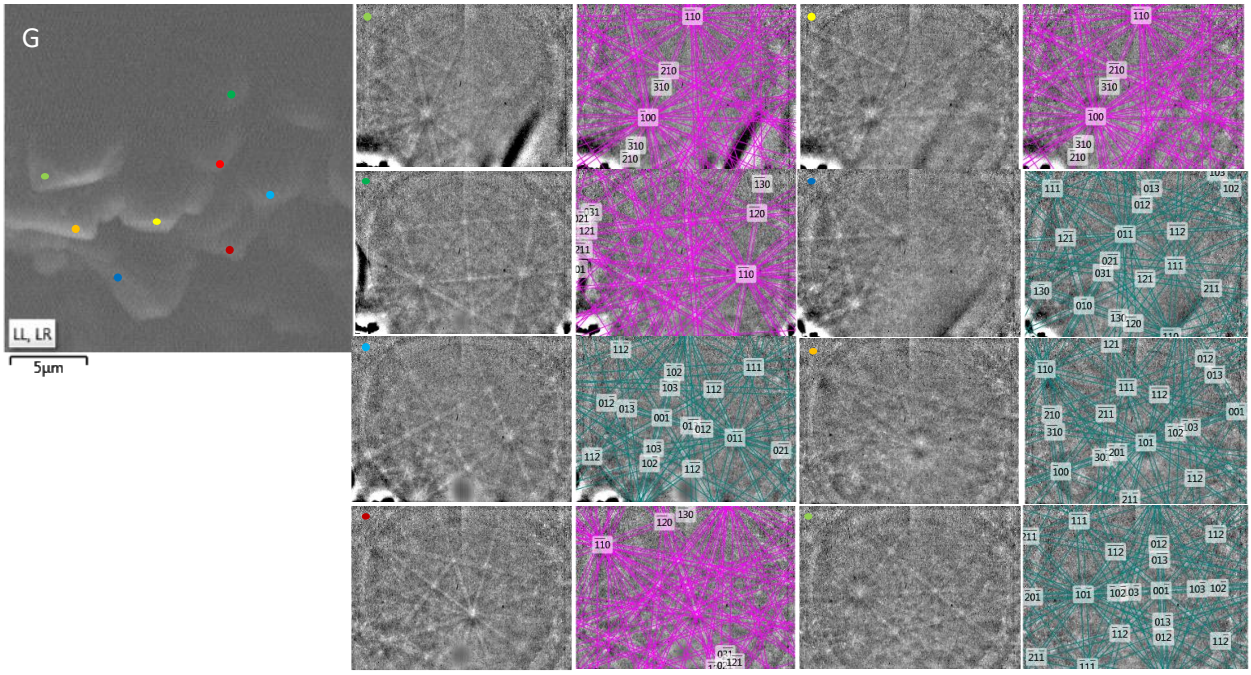

Fig. A.1.2. Multipoint EBSD analysis carried out on a batch of 3C-SiC (A-B) and M-SiC (C-G) samples. The EBSD was done on different crystals which actively diffract on the detector as observed in the fore scatter diode (FSD) images. The FSD image has every point with a color marked where EBSD was carried out. The Kikuchi diffraction pattern and indexing from each corresponding point were detected and indexed as 4H, 3C or 15R.

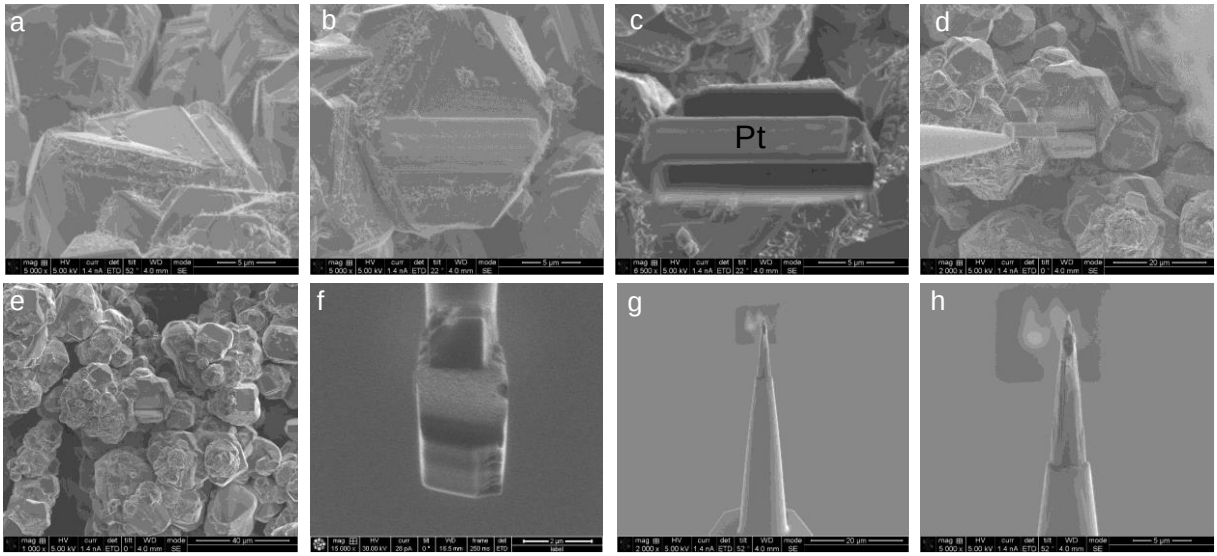

Fig. A.1.3. a. SEM image of a flat surface identified for FIB preparation of atom probe tomography tips. b. Deposition of platinum to protect the sample of interest. c. FIB milling of trenches on either side of the sample of interest protected by platinum coating. d. Lift out of a lamella using micromanipulator. e. Low magnification SEM image showing trench of the lifted-out lamella in material of interest. f. FIB image showing a section of lamella, platinum welded on a silicon micropost. g. Polished tip for atom probe tomography measurement on a silicon micropost. h. Higher magnification image of the atom probe tomography tip.

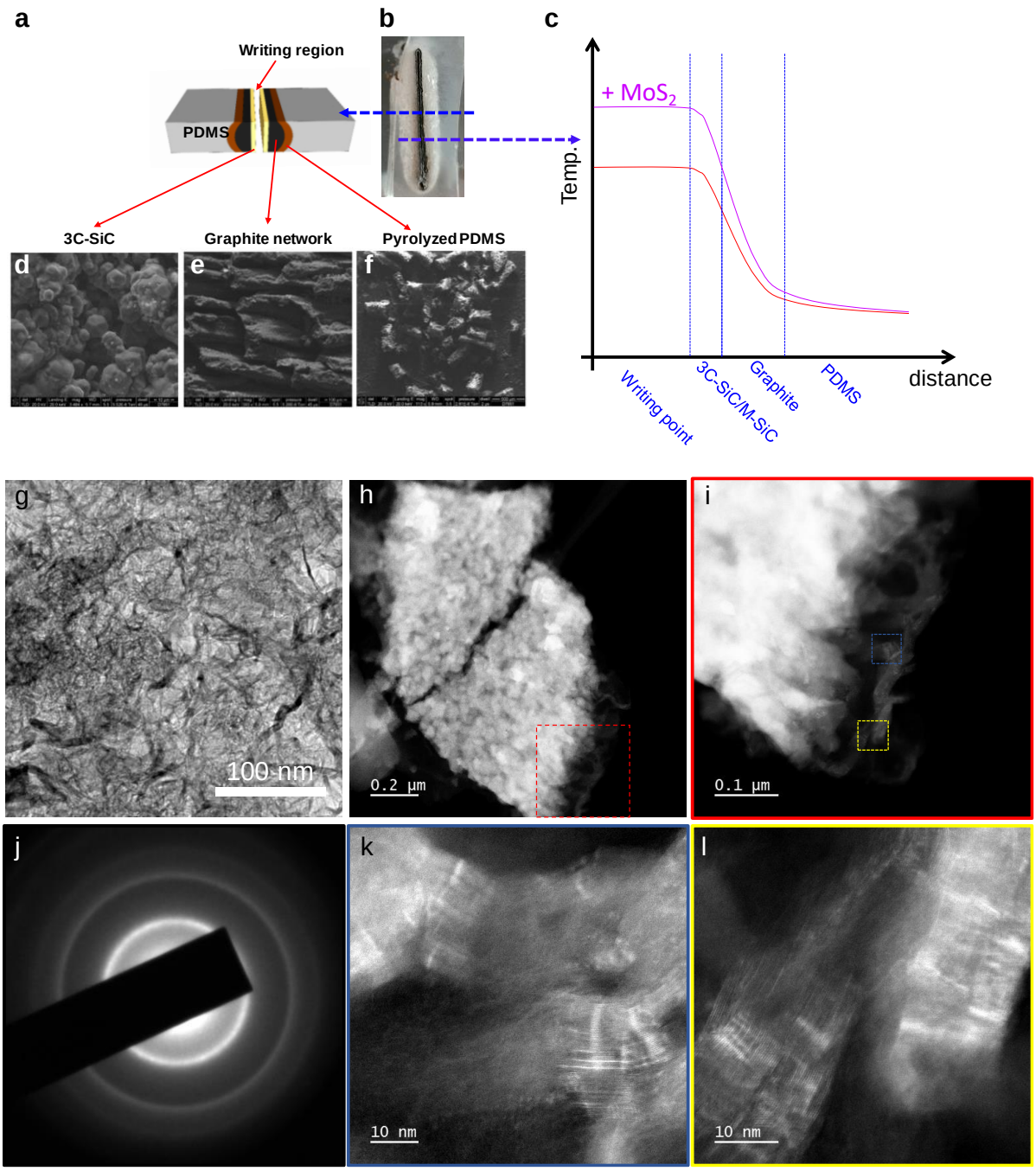

Fig. A.1.4. Schematic illustration of the different layers of materials formed (a) with respect to the laser writing point, embedded in a PDMS matrix (b). The different layers formed is as a result of a temperature gradient that would exist from the laser writing point into the bulk which would control the thermodynamics of reaction eventually leading to such a layered structure (c). Moreover, we can observe these layers in SEM images (d-f). Furthermore, addition of MoS_2 to PDMS leads to a higher temperature at the burning

point (c). This is Fig. 4. continued. due to the fact that oxidation of MoS_2 is highly exothermic and the product formed -MoO_3 which is highly volatile at such temperatures. This highly exothermic nature of the oxidation reaction leads to accelerated kinetics, which coupled with catalytic activity of molybdenum in fixing nitrogen increases the doping by ten times and also gives it a grading which follows the temperature profile in (c). Graphitic layers as seen in a TEM (g) and its corresponding SAED pattern (j). HAADF STEM image of a microtomed section of the SiC-graphite (h) with magnified section (i) clearly showing the SiC-graphite interface where graphite is seen in ribbon like structures further confirmed at higher magnification imaging (k,l).

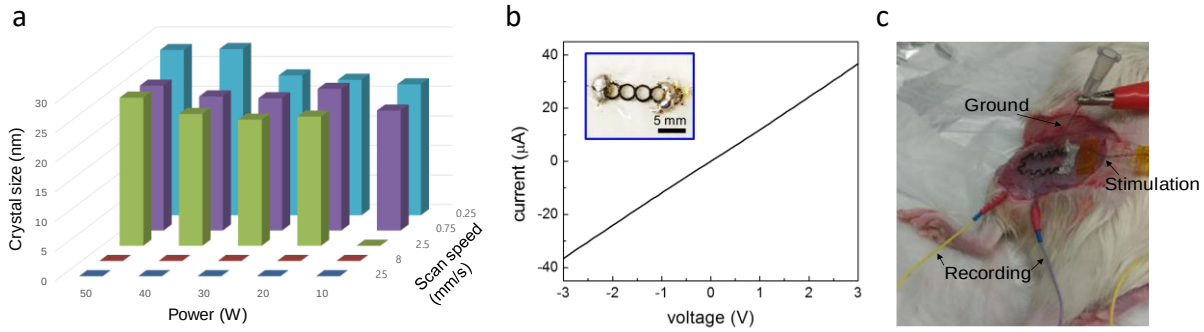

Fig. A.1.5. (a) Crystal size control factors in the laser ablation synthesis is demonstrated here as a function of the laser power and scan speed. This illustrates that the synthesis has a cutoff power with respect to the synthesis parameters and control on crystal on size above the cutoff. The crystal sizes were estimated by using Debye-Scherrer equation on the (111) peak of x-ray diffraction/scattering. (b) I-V characteristic of a device made by SiC printing showing high conductance due to the supporting graphite layer below the SiC crystals. The high conductance is due to the graphitic layer and illustrates its utility in enabling integration of devices for future large-scale device fabrication (c) Configuration for 3C-SiC muscle stimulation and recording electrodes on the skeletal muscle of an adult rat. (Main manuscript Fig. 2k)

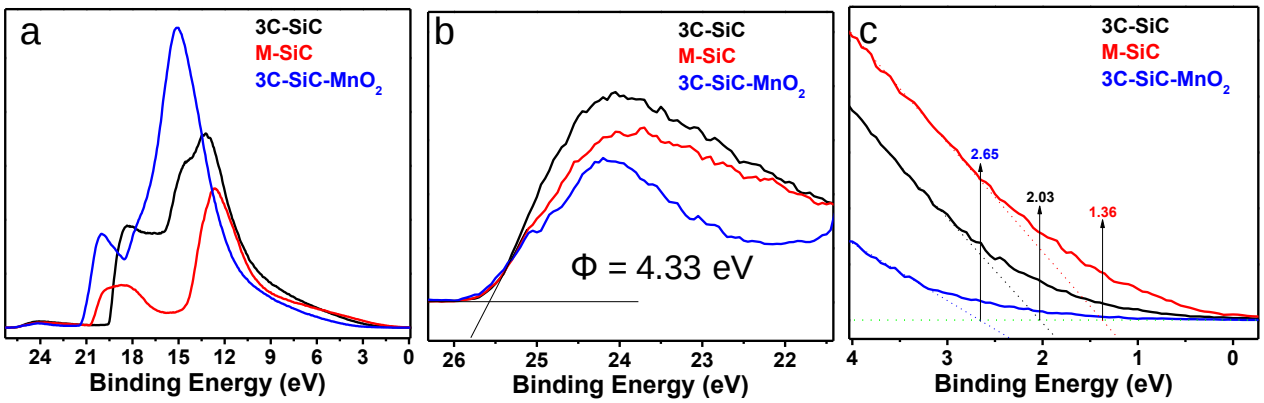

Fig. A.1.6. a. UPS spectrum of 3C-SiC, M-SiC, 3C-SiC-MnO_2, b. Estimation of work function from the secondary scattering edge cutoff of the UPS spectrum, c. Estimation of HOMO from the valence band edge of the UPS spectrum.

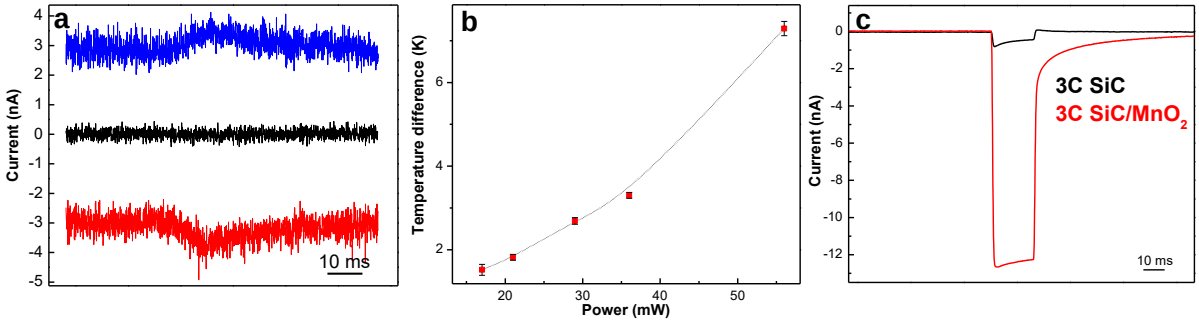

Fig. A.1.7. a. M-SiC consisting of a mixed phase and excess nitrogen doping, demonstrated a weak photothermal effect which would switch polarity with the holding level and portray a growing current with the applied stimulation (350 nm LED with a 10 ms pulse). The polarity flipping is due to the fact that thermal currents always superpose onto any injected current following its direction contrary to faradaic processes. b. Temperature change induced by a 10 ms pulse of 532 nm laser, as function of stimulation power averaged over 10 holding levels. This shows that the photothermal effect is small and thus a non-lethal dosage on cells further preventing the fluorescence imaging laser from producing stimulation artifacts in our observation. c. Surface modification of 3C-SiC by MnO_2 further enhances the photoanodic oxidation reaction as indicated by the magnitude difference in current (Stimulation: 350 nm LED with a 10 ms pulse).

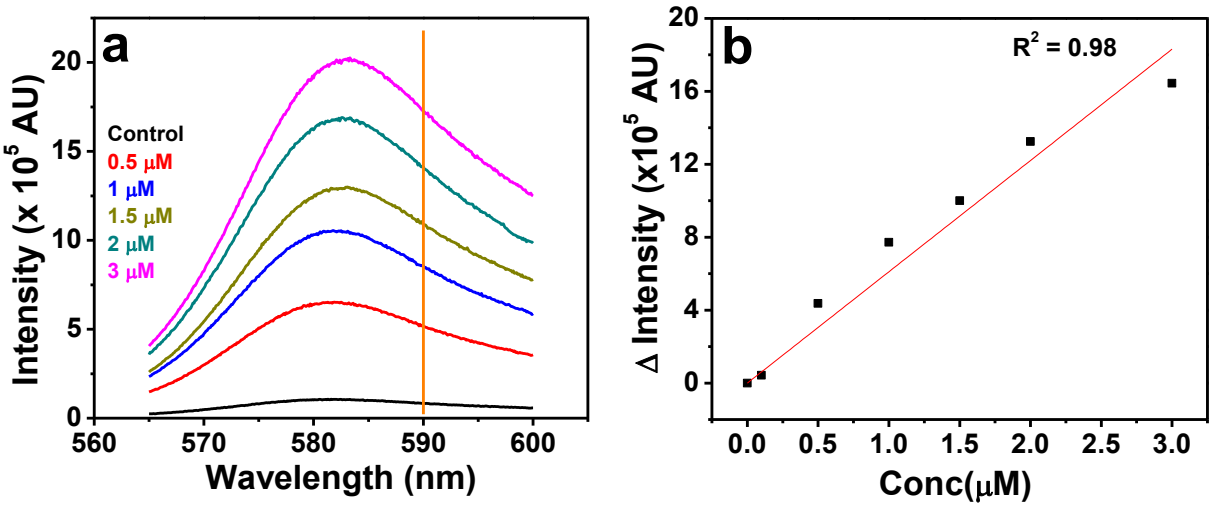

Fig. A.1.8. a. Steady state fluorescence of Amplex Red for specific concentration of hydrogen peroxide. Each curve is a separate measurement done with freshly mixed dye stock solution and hydrogen peroxide of an appropriate concentration. b. The intensity changes with respect to 0 mM hydrogen peroxide curve at 590 nm is plotted with respected to the added concentration of hydrogen peroxide. The curve fitted by least squares methods (R^2 = 0.98) gives a linear correlation between concentration change of hydrogen peroxide and the fluorescence intensity change for a fixed concentration of Amplex Red. This fitted curve is used a calibration curve to construct the quantitative fluorescence kinetics curve in main manuscript Fig. 5d.

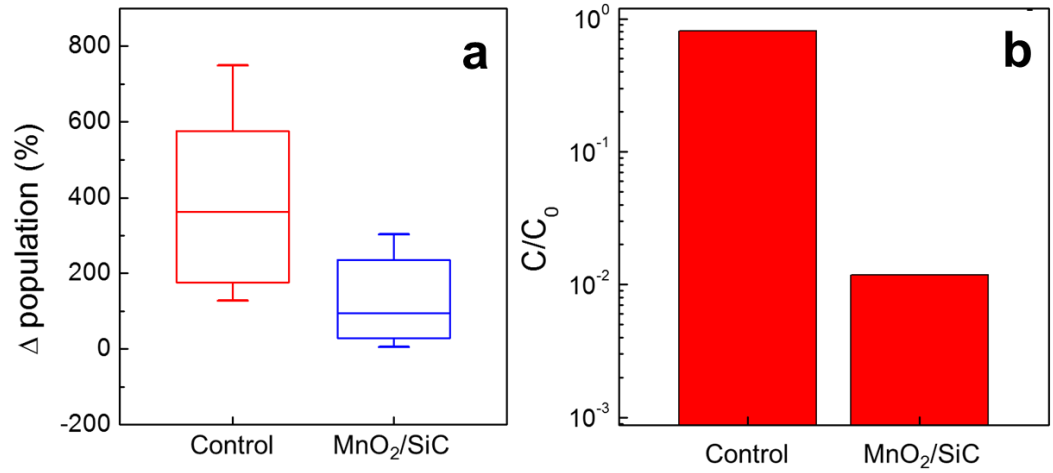

Fig. A.1.9. a. Percentage change in bacterial population measured by standard spread plate culture, with photoelectrochemical anti-bacterial treatment of 3C-SiC-MnO_2

compared Fig. 9. continued. with samples containing 3C-SiC-MnO_2 under dark (N=15). b. Average fractional change in bacterial population (with respect to bacterial culture without any 3C-SiC-MnO_2 under light conditions), estimated by standard spread plate culture with photoelectrochemical anti-bacterial treatment of 3C-SiC-MnO_2 compared with samples containing 3C-SiC-MnO_2 under dark.

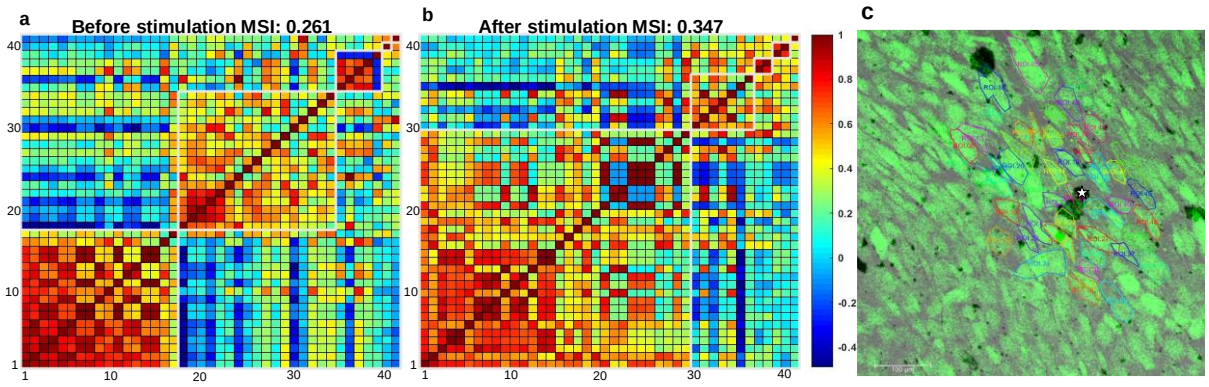

Fig. A.1.10. a. Synchronization matrix of calcium signals before stimulation along with mean synchronization index (MSI) of 0.261. b. Synchronization matrix of calcium signals after stimulation along with mean synchronization index (MSI) of 0.347. (Stimulation Power: 29 mW, Pulse: 1 ms).c. Overlay of calcium and DIC image showing 3C-SiC particles co-cultured with smooth muscle cells along with stimulation point indicated as a white star. Region of interests (ROIs) used for synchronization analysis in a and b have been marked (Stimulation Power: 29 mW, Pulse: 1 ms)

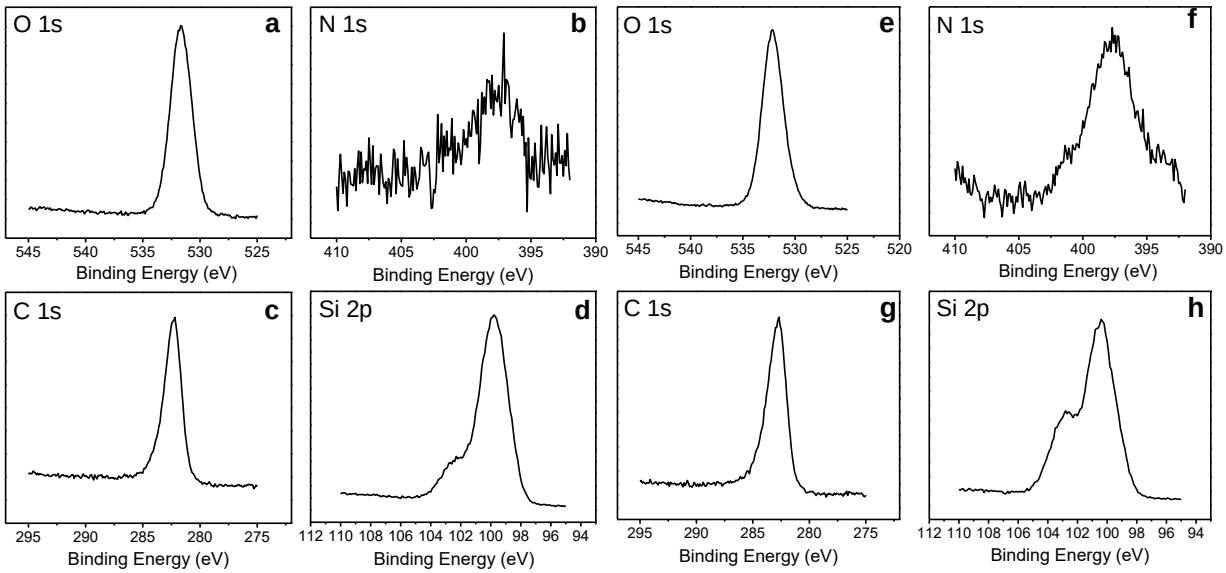

Fig. A.1.11. Elemental XPS spectrum collected on 3C-SiC samples for (a) oxygen 1s, (b) nitrogen 1s, (c) carbon 1s, (d) silicon 2p. and M-SiC samples for (e) oxygen 1s, (f) nitrogen 1s, (g) carbon 1s, (h) silicon 2p.

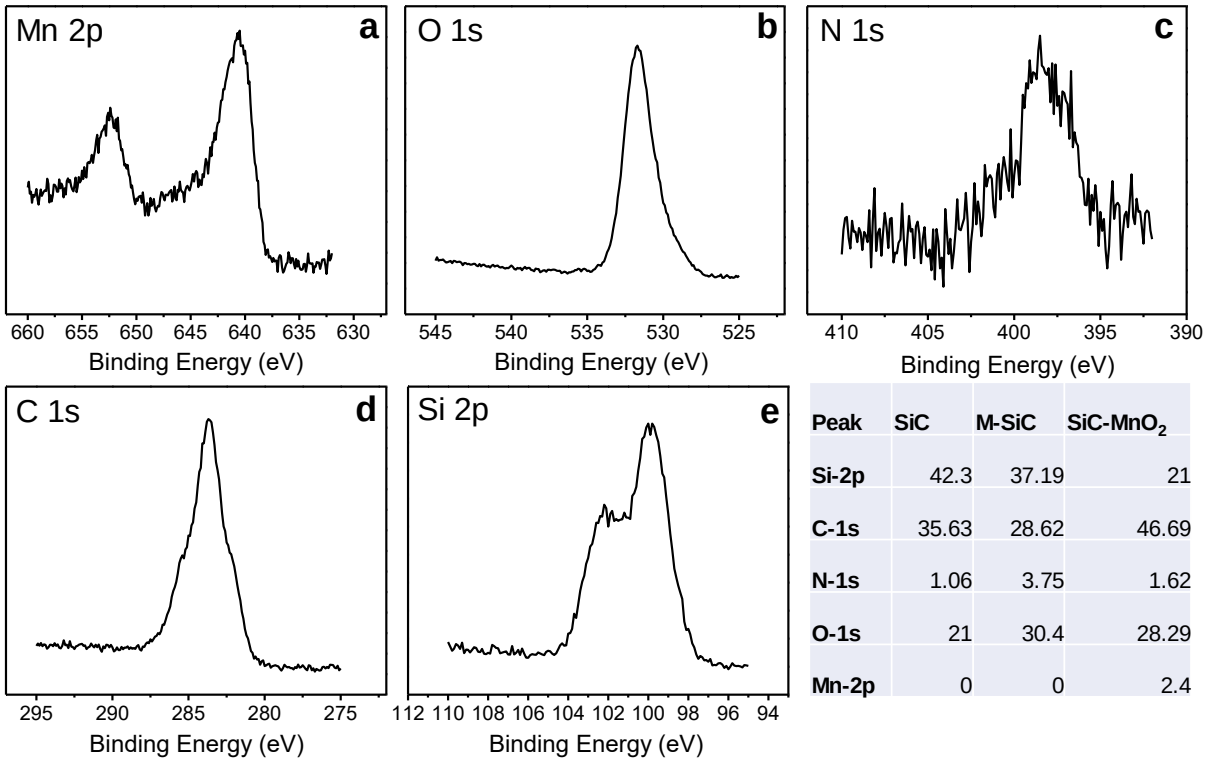

Peak	SiC	M-SiC	SiC-MnO_2
Si-2p	42.3	37.19	21
C-1s	35.63	28.62	46.69
N-1s	1.06	3.75	1.62
O-1s	21	30.4	28.29
Mn-2p	0	0	2.4

Fig. A.1.12. Elemental XPS spectrum collected on 3C-SiC-MnO_2 samples for (a) manganese 2p, (b) oxygen 1s, (c) nitrogen 1s, (d) carbon 1s, (e) silicon 2p, (f) Table representing surface composition in atomic percentages for each element in 3C-SiC, M-SiC and 3C-SiC-MnO_2

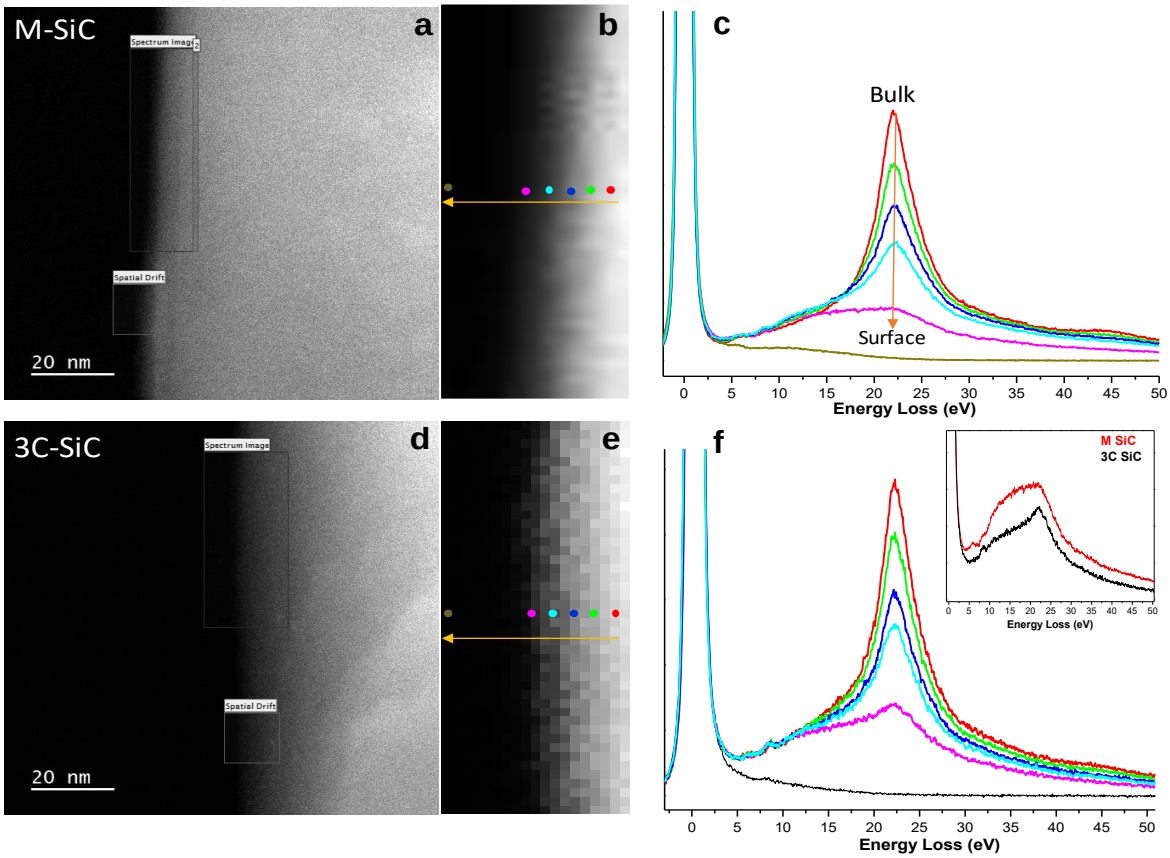

Fig. A.1.13. EELS mapping done for surface and bulk plasmons in M-SiC (b) and 3C-SiC (e) on regions represented by HAADF STEM image in (a) and (d) respectively. The spatial evolution of low loss EELS spectrum from bulk of a microtomed crystal to its surface for a M-SiC (c) and 3C-SiC (f) crystal. The evolution from bulk to surface shows how the surface phonons are different in either case which could be correlated with the nitrogen doping level as revealed by atom probe tomography and surface oxide and nitride defects from XPS. Zero loss peak normalized, surface low loss EELS on microtomed crystals of 3C and M-SiC (f-inset). The M-SiC shows much higher surface phonon density of states compared to 3C-SiC in agreement with the nitrogen doping levels in atom probe tomography, surface oxide and nitride defects from XPS. This difference explains why M-SiC shows photothermal effect compared to photoelectrochemical in 3C-SiC.

.

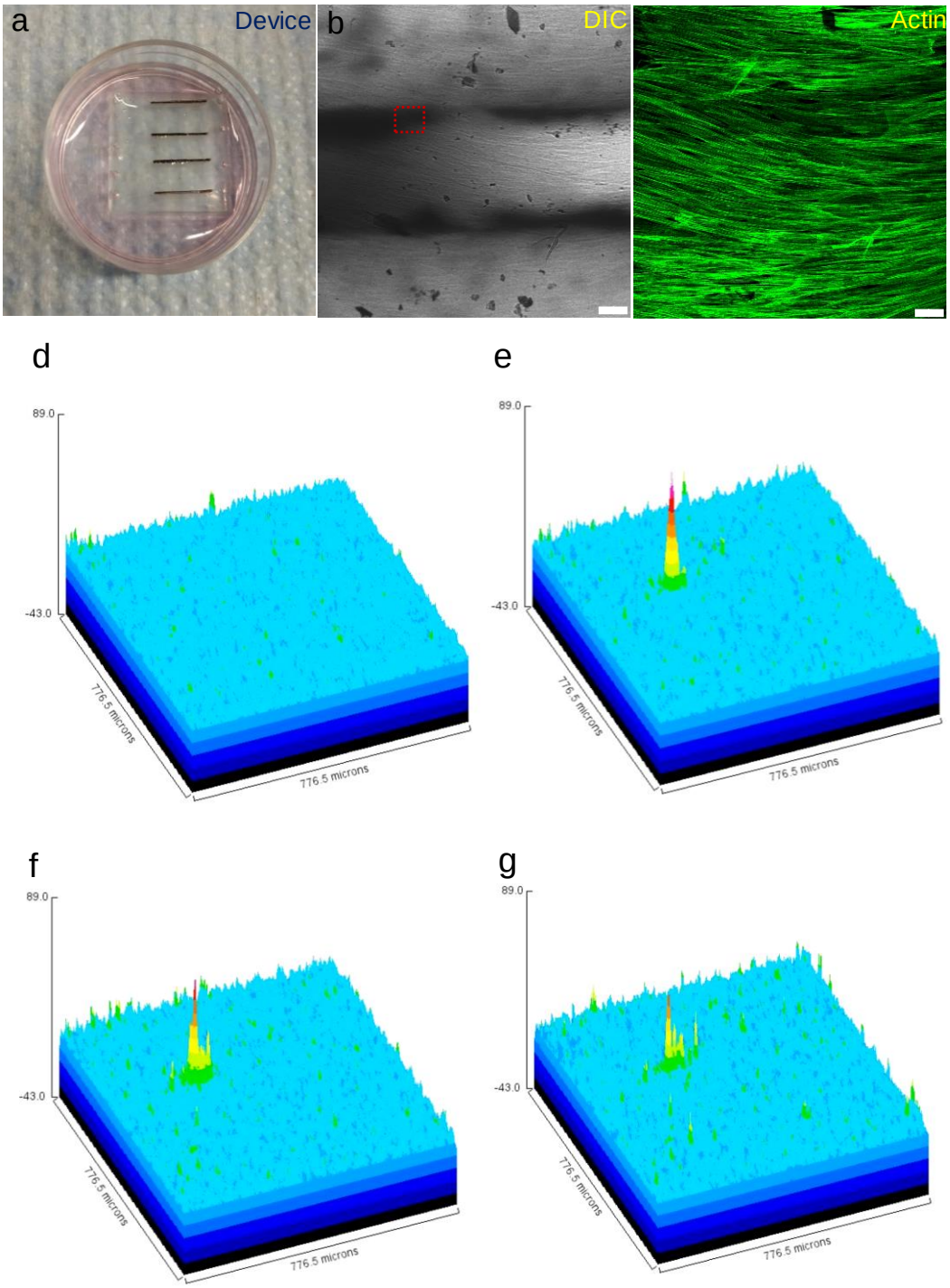

Fig. A.1.14. HASMCs are cultured on the device (a) to obtain a uniform film of cells as observed through DIC image (b), Actin immunofluorescence staining (c) and Z-stack (Figure 3i in main manuscript). Differential calcium fluorescence (ΔF/F) surface plots are constructed for device shown in (b): Time points before (-2.0 s) (d) and after stimulation

Fig. A.1.14. continued. (e-g) (0.0 s, 2.0 s, 4.0 s respectively) for a 8 mW, 1 ms stimulation on the region indicated by red box in (b). Magnified views of calcium waves in red boxed region is represented in main manuscript Fig.5j. Scale bars in (b-c) are 100 μm each

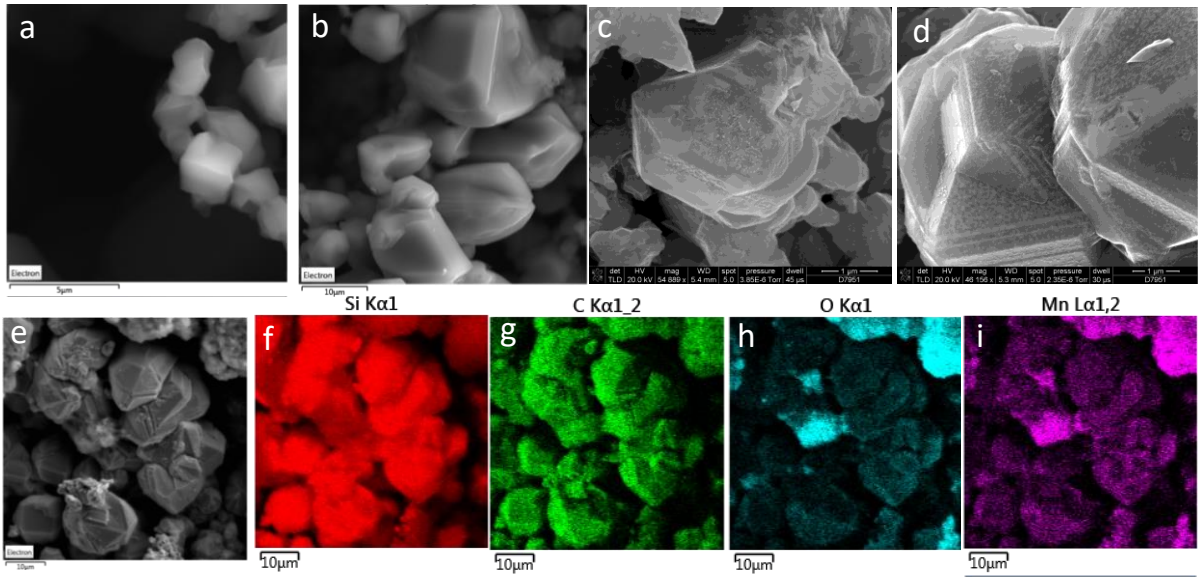

Fig. A.1.15. a. SEM images of 3C-SiC after purification revealing cubic morphology. b. SEM images of M-SiC after purification revealing rhombohedral morphology arising due to phase mixing induced after MoS_2 addition. c-d. Magnified view of crystals showing a coating of MnO_2 deposited on them by electroless deposition. e. SEM image of 3C-SiC-MnO_2 crystals where EDS mapping was done. f-i. EDS map of on crystals shown in (e).

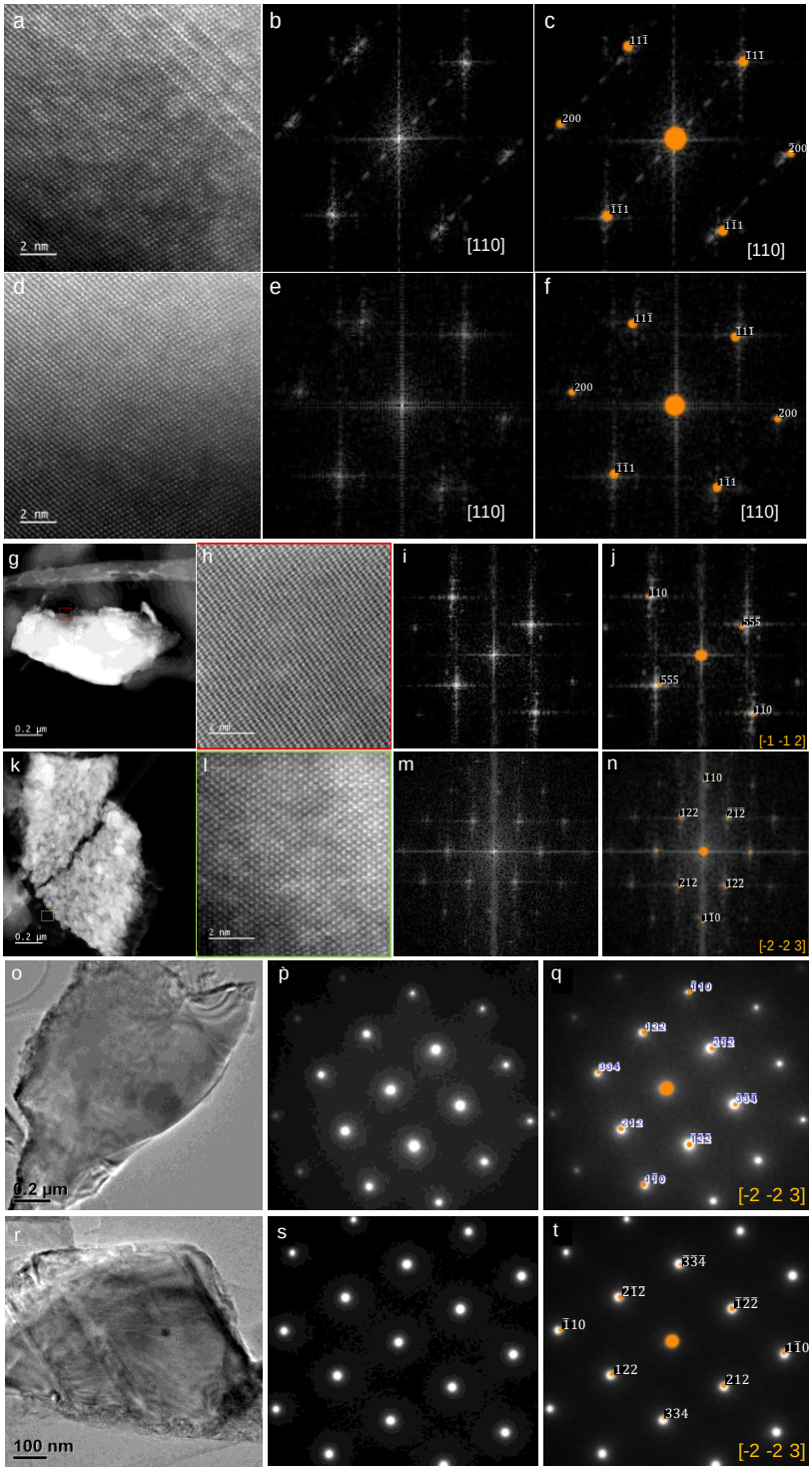

Fig. A.1.16. HAADF STEM image of a 3C-SiC microtomed crystal section (a) and (d). (b) and (e) are their corresponding FFTs. (c) and (f) show the indexing of FFTs to [110] zone using crystal maker software. HAADF STEM image of microtomed sections of M-SiC (g)

Fig. A.1.16 continued. and (k). HAADF STEM image of a 15R-SiC microtomed crystal section (h) and (l). (i) and (m) are their corresponding FFTs. (j) and (n) show the indexing of FFTs to [-1-1 2] and [-2-23] zone respectively. TEM image of microtomed sections of M-SiC (o) and (r). SAED patterns collected on respective sections (p) and (s). Indexing of corresponding SAED patterns to [-2-2 3] zone (q) and (t).

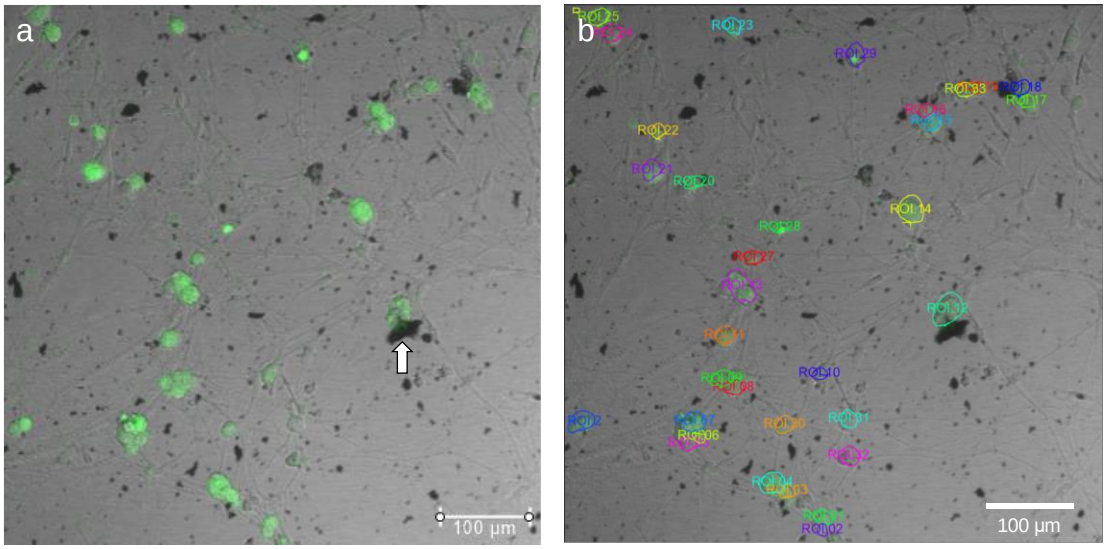

Fig. A.1.17. Region of interest (ROI) of neuronal soma marked on DIC and calcium image. The neuron in ROI 12 was stimulated by a 1 ms pulse of 5.3 mW. (Main manuscript Fig. 6f)

A2. Extended data and figures for Chapter 3

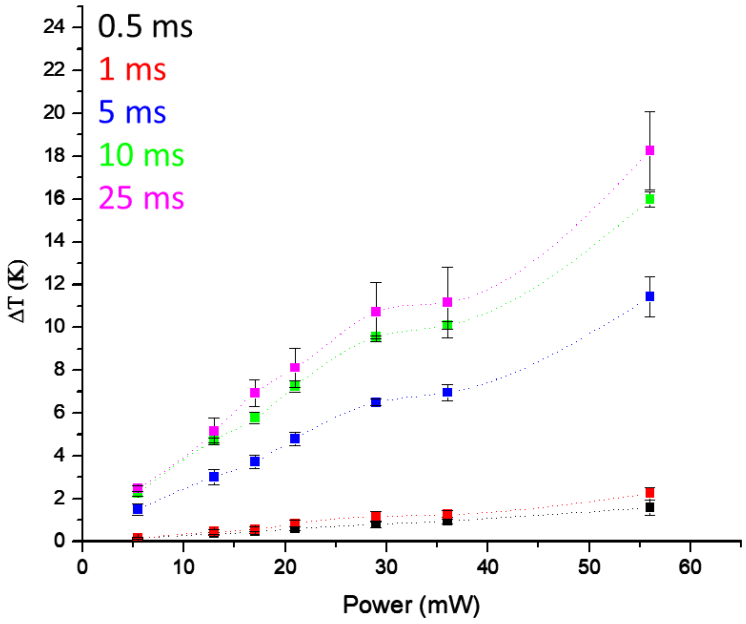

Fig. A.2.1. Graph showing temperatures generated on p3HT nanofiber matrix stimulation by a 532 nm laser for various power and pulse width across five different spots of the sample.

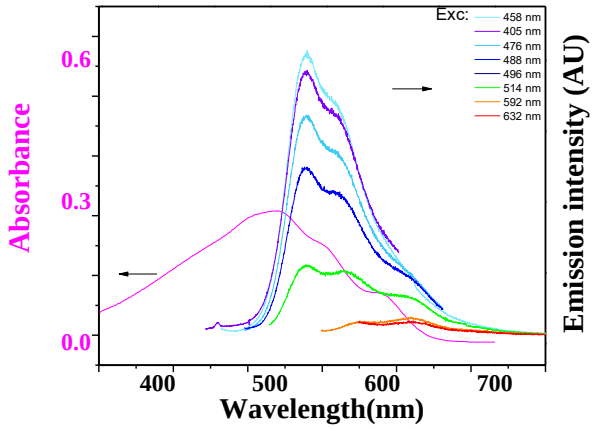

Fig. A.2.2. UV-Vis absorbance spectrum and photoluminescence spectrum for as synthesized P3HT nanofibers in cyclohexanone.

A3. Extended data and figures for Chapter 4

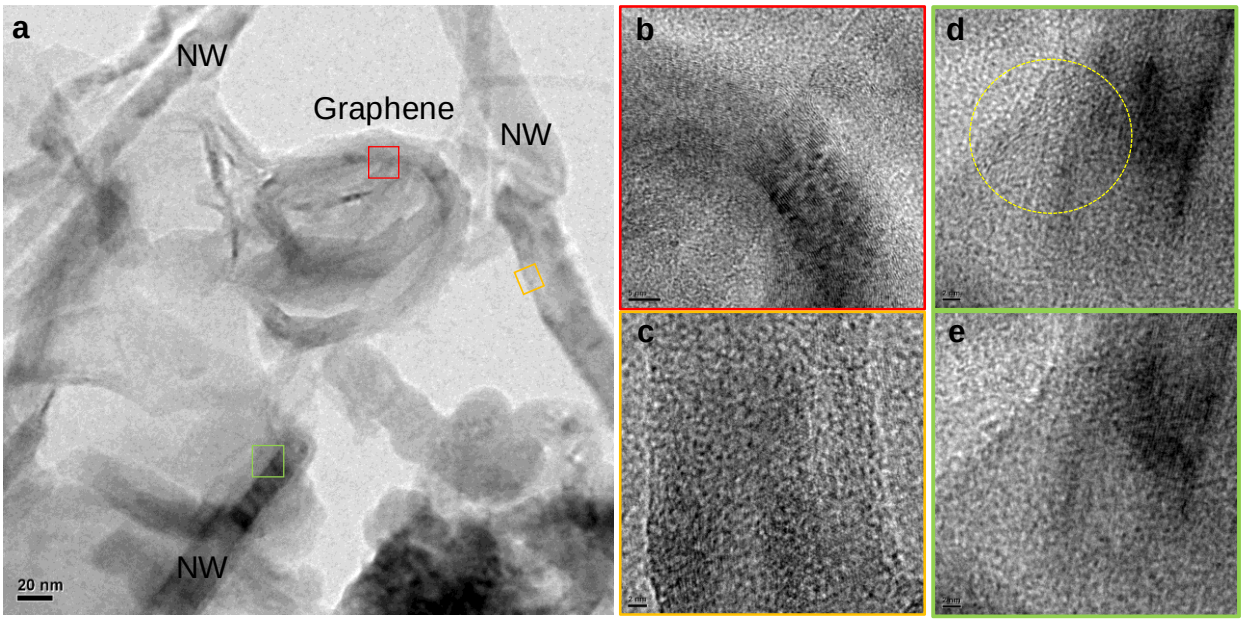

Fig. A.3.1. a. TEM image showing graphene ribbon like interconnects forming between nanowires after mechanochemical synthesis of Si-Graphene hybrid, b. Graphene lattice as seen on interconnect, c. Silicon lattice of a nanowire, d. Graphene lattice as seen emanating from a nanowire whose lattice (e) is seen by changing the z-focus in the microscope.

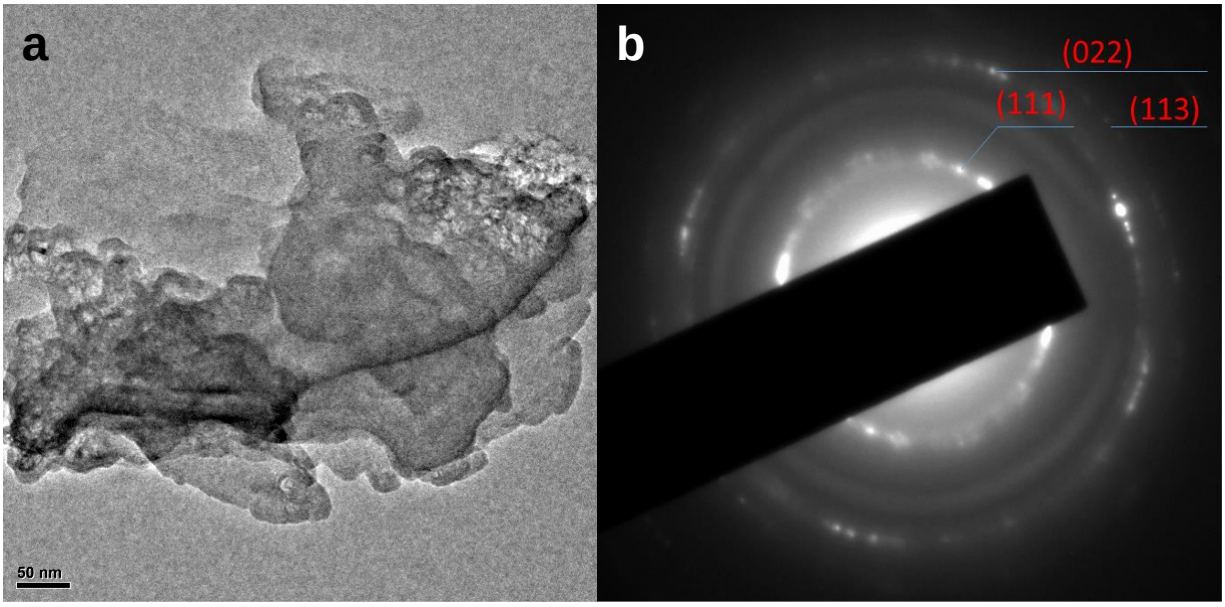

Fig. A.3.2. a. Detonation nanodiamond assembling into sheets in a formvar grid on drop casting and drying, b. Electron diffraction pattern of (a) indexing to cubic diamond structure.[28]

Low Loss EELS (LL- EELS)

1. 34 keV is assigned: Bulk plasmonic loss in diamond
2. 12-13 keV: Several electronic transition between crystalline levels:
   $\Sigma_2 \rightarrow \Sigma_3$; $L'_3 \rightarrow L_3$; $X_4 \rightarrow X_1$; $L'_3 \rightarrow L_1$
3. 22 to 23 keV :$\Gamma'_{25} \rightarrow \Gamma_1$ and/or loss to surface plasmons

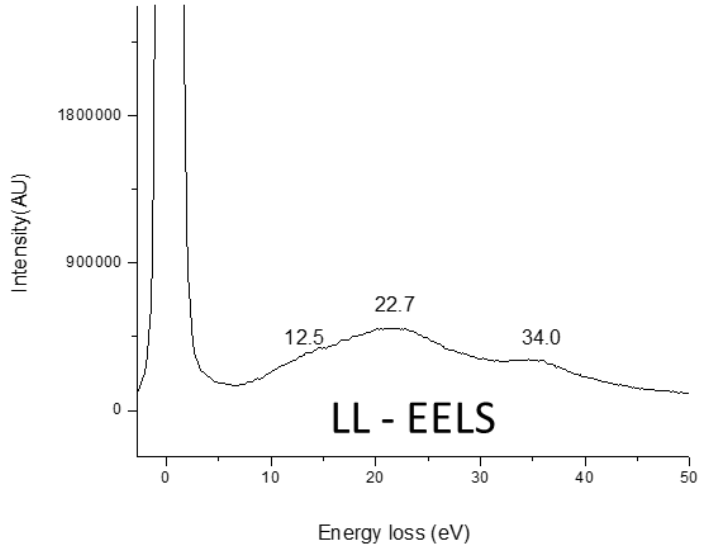

Fig. A.3.3. Low loss EELS of detonation type nanodiamond confirming the diamond structure along with plasmonic transitions assigned to the peaks.[29]

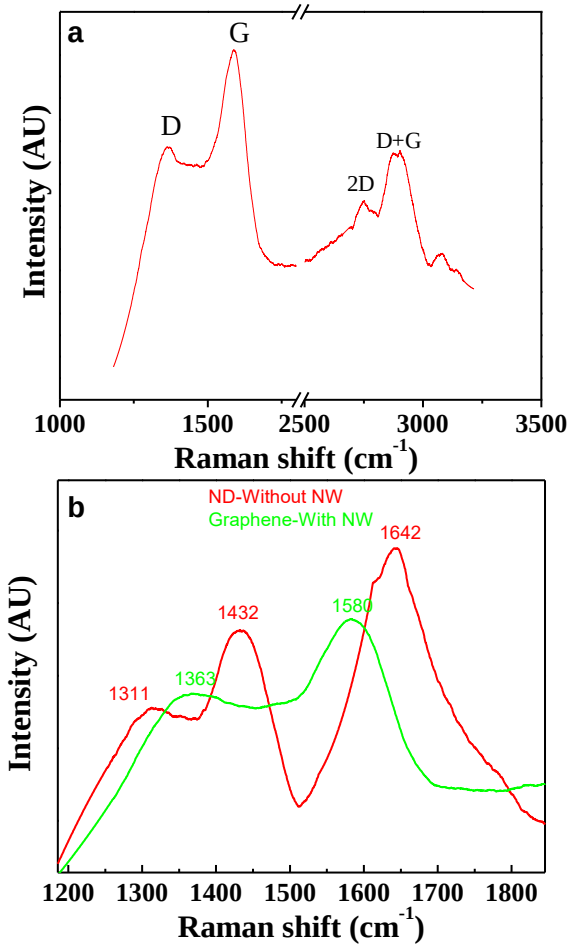

Peak	Assignment
1367	Graphene -D
1582	Graphene-G
2734	Graphene-2D (broad peak indicates multilayer graphene)
2885	D+G peak

Peak	Assignment
1311	ND- T_{2g} (sp^3)
1363	Graphene-D
1432	Graphitic shell –D (Detonation diamond)
1580	Graphene-G
1642	Graphitic shell-G (Detonation diamond)

Fig. A.3.4. Raman spectrum of graphene on silicon (a) and peak assignment compared with spectrum of detonation type nanodiamond (b) along with peak assignments.[16,28]